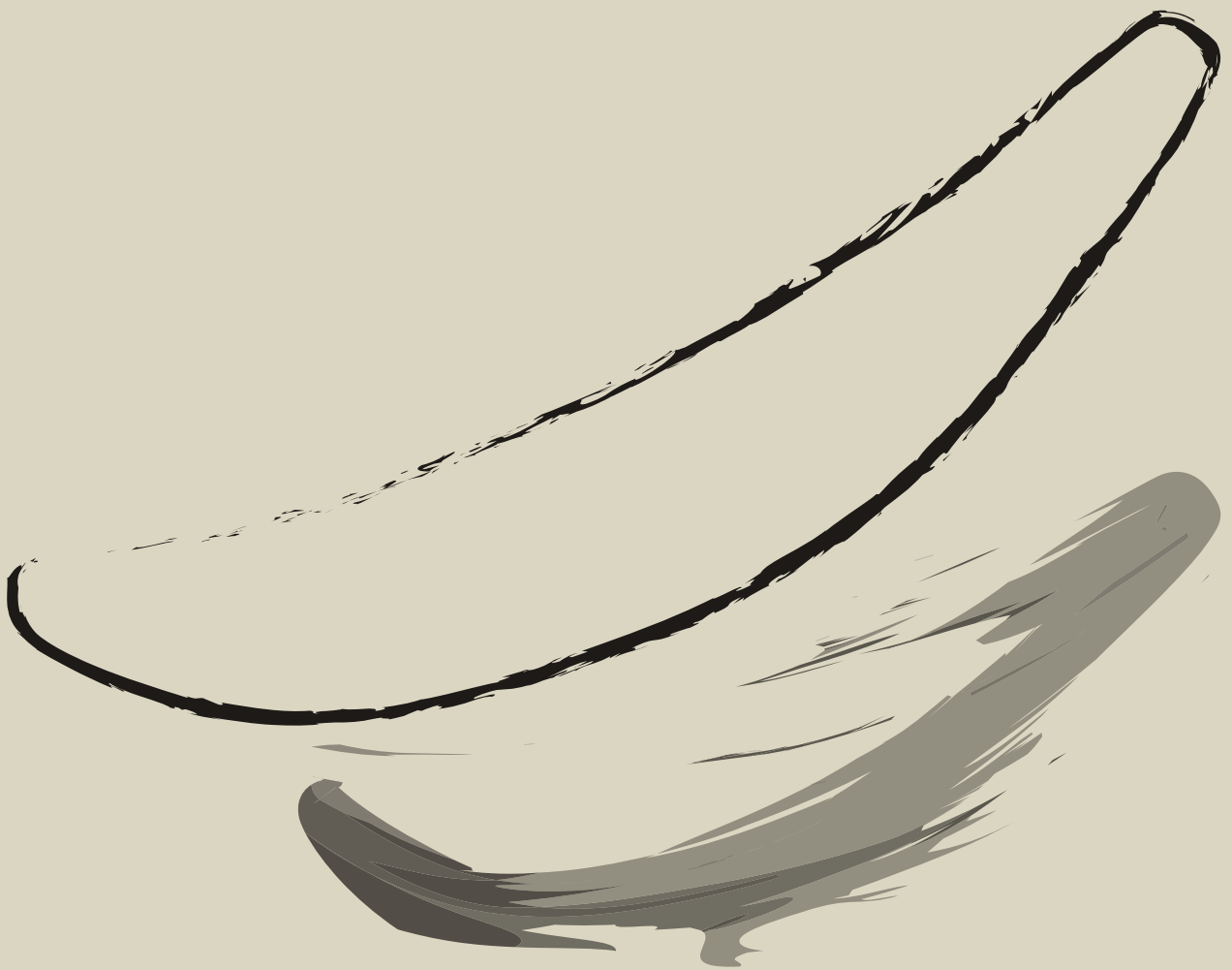# LIGHT AND SHADOW ON GRAVITATIONAL FLEXION MEASUREMENTS

AGNESE FABRIS

DISSERTATION

submitted to the

Combined Faculties of the Natural Sciences and Mathematics

of the Ruperto-Carola-University of Heidelberg, Germany

for the degree of

Doctor of Natural Sciences

Put forward by

Agnese Fabris
born in Torino, Italy

Oral examination: 18 December 2015

Light and shadow
on gravitational flexion measurements

Agnese Fabris

Institut für Theoretische Astrophysik

Referees: Prof. Dr. Matthias Bartelmann
              Prof. Dr. Joachim Wambsganß

a Hashem
esempio di gentile fermezza

*"Misura ciò che è misurabile,
e rendi misurabile ciò che non lo è."*

GALILEO GALILEI

Abstract

Is gravitational flexion reliably measurable in realistic observational conditions? To address this question we undertook an exhaustive investigation into the problem of estimating flexion. By means of synthetic data, we tested the ability of different methods to recover the shape of faint background galaxies with the level of detail necessary to account for the spin-1 and spin-3 distortions caused by flexion. Three different methods for weak lensing measurements have been extended in order to measure the high-order moments of surface brightness necessary to quantify the flexion-induced deformations. We observed that, for the two methods which exploit a weight function to control the noise and afterwards correct for the impact of this procedure, a successful outcome depends upon numerous assumptions on the properties of the objects investigated, making these techniques less appealing for practical applications. The third method we tested employs a principal component analysis algorithm to de-noise the images. Even though, in the most strict observational conditions, we could not achieve a precise measurement of the high-order distortions, this method stood out as a promising technique for shape measurements in weak lensing applications. Our analysis shows that a deeper understanding of the impact of pixel noise on the flexion estimators is required before measurements of flexion in real data can be carried out and, finally, used to exploit the vast potential of gravitational flexion.

Zusammenfassung

Die zentrale Frage dieser Arbeit lautet: Ist gravitative Flexion unter realistischen Bedingungen zuverläsig messbar? In diesem Zusammenhang wird das Problem der Bestimmung des Flexion-Effektes detailliert untersucht. Unter Verwendung synthetischer Datensätze wird die Effektivität unterschied-licher Methoden analysiert, die prinzipiell dazu in der Lage sind, die Form schwacher Hintergrundgalaxien bis zu einer Genauigkeit zu bestimmen, die mögliche Effekte von Spin-1 und Spin-3 Verzerrungen durch Flexion auflöst. Insgesamt wurden drei verschiedene Methoden zur Messung des schwachen Linseneffektes verwendet und in einer Weise adaptiert, dass höhere Momente in der Flächenhelligkeit der Hintergrundgalaxien ermittelt werden können, die eine Bestimmung der Verzerrungen durch Flexion ermöglichen. Zwei dieser Methoden verwenden eine Gewichtungsfunktion zur Kontrolle des Hintergrundrauschens, deren Effekt auf die Messung im Nachhinein korrigiert werden muss. Es stellt sich dabei heraus, dass ein verwertbares Ergebnis nur unter einschränkenden Annahmen über die Eigenschaften der zu untersuchenden Objekte erreicht werden kann. Für eine allgemeine praktische Anwendung erweisen sie sich daher als weniger sinnvoll. Die dritte Methode besteht in einer Hauptkomponentenanalyse der Galaxienbilder, um sie so gut wie möglich vom Hintergrundrauschen zu befreien. Die Anwendung dieser Methode zeigt allerdings, dass selbst unter bestmöglichen Beobachtungs- und Messbedingungen keine präzise Messung der höheren Momente des Galaxienverzerrung möglich ist. Die Anwendung dieser Methode auf den schwachen Linseneffekt erweist sich allerdings als vielversprechend. Die Untersuchungen dieser Arbeit zeigen, dass zunächst ein tieferes Verständnis der Effekte von Pixel-Rauschen auf die Schätzer für Flexion-Effekte notwendig ist, um eine sinnvolle Messung der gravitativen Flexion in Beobachtungsdaten erfolgreich durchzuführen.

Contents

Motivation

The accurate characterization of the mass distribution of large structures in the universe represents an important means by which cosmological models and theories of structure formation can be constrained. A standard technique to achieve this characterization is, nowadays, represented by weak gravitational lensing, which, in the last years, has been routinely exploited to infer the matter distribution in the universe on a wide range of scales, allowing to explore the density profiles of galactic halos, likewise halos of galaxy clusters, as well as to trace the large-scale structure. Indeed, weak gravitational lensing represents a powerful and versatile tool to analyze dark cosmological structures, since, differently from other techniques, it probes the mass distribution independently of the nature (visible or dark) or the dynamical state of the matter.

Weak lensing analyses are typically performed by examining the ellipticity of distant galaxies, seeking a coherent alignment of these ellipticities induced by mass along the line of sight. This phenomenon, known as gravitational shear, is caused by the gravitational tidal field. In particular, it can be related to linear combinations of the second order derivatives of the projected gravitational potential. Nevertheless, as first shown by Goldberg and Natarajan (2002), valuable information is also contained in the derivatives of the tidal field. These third order derivatives of the potential can be conveniently combined into two quantities, called first and second flexion, or $\mathcal{F}$ and $\mathcal{G}$ flexion, which give rise to characteristic deformations of astronomical images. Specifically, the first flexion introduces a shift in the centroid of the images, while the second flexion creates patterns with a three-fold rotational symmetry. These distortions, when applied on intrinsically elliptical galaxies, bend the galaxy images into "banana-shaped" arclets. Note that, even though the level of the flexion signal is expected to be lower than for the shear, the noise level should be lower, as well. In fact, while galaxies are intrinsically elliptical and, thus, have an intrinsic deformation mimicking external shear, they do not typically exhibit intrinsic deformations resembling flexion. Nevertheless, a reliable measurement of the intrinsic level of flexion in distant galaxies has not been convincingly demon-

strated yet.

In the last decade, many theoretical studies have shown that flexion can contribute to cosmology in several ways. First of all, being related to the third derivatives of the lensing potential, it is sensitive to smaller-scale variations in the projected mass distribution (Bacon et al., 2006; Okura et al., 2007; Leonard et al., 2009; Bacon et al., 2010). Hence, if flexion became ordinarily measurable, it would improve the spatial resolution of dark matter maps, allowing to test one of the fundamental predictions of the present concordance cosmological model, namely that cosmological objects, like galaxy clusters, should be richly substructured. Besides representing an excellent tool to detect substructures, it has also been shown that flexion is very powerful in constraining the profiles of dark matter halos, improving both the mass and the concentration estimates (Bacon et al., 2006; Leonard and King, 2010). Furthermore, galaxy-galaxy flexion can be used to determine the shape of galactic halos, providing tighter constraints on their ellipticity compared to those obtained from shear measurements (Hawken and Bridle, 2009; Er et al., 2012; Er and Bartelmann, 2013). Finally, flexion could, in principle, be used to study the growth of structures in the universe, since lensing by large-scale structure grows with time at a different rate for shear and flexion.

These theoretical works, which investigated the potentialities of flexion, have been accompanied by several attempts to measure flexion in real data, mainly by means of two distinct methods. The first method is based on the decomposition of the lensed images into a sum of orthogonal basis functions, called *shapelets*, which are related to two dimensional Gauss-Hermite polynomials (Bernstein and Jarvis, 2002; Refregier, 2003a; Goldberg and Bacon, 2005; Massey et al., 2007b). The second method, *HOLICS*, uses higher order moments of the brightness distribution of the lensed images to construct flexion estimators (Okura et al., 2007; Goldberg and Leonard, 2007; Okura et al., 2008). Most recently, a third approach (so-called analytic image model, *AIM*) has been proposed by Cain et al. (2011) and is based on a parametric modeling of the lensed galaxy images. The *shapelets* technique has been used to measure galaxy-galaxy flexion in a sample of field galaxies in the Deep Lens Survey (Goldberg and Bacon, 2005), as well as in the COSMOS survey (Velander et al., 2011). On the other side, *HOLICS* and *AIM* have been applied to estimate the flexion signal in the galaxy cluster Abell 1689, using both Hubble Space Telescope observations (Leonard et al., 2007, 2011; Cain et al., 2011), and ground-based Subaru observations (Okura et al., 2008).

Even though several groups claim to have measured flexion, the reliability of these measurements is still missing a solid ground. In fact, the theoretical work which accompanied these analyses mostly focused on exploring the potential

of flexion estimates, while less emphasis was given to testing the feasibility of performing these measurements in realistic situations. In the few cases in which this has been done, like in Rowe et al. (2013), a different picture emerged, showing that, differently from shear, flexion estimates are dominated by noise at the pixel level, rather than noise due to intrinsic properties of the galaxies, and that the final measurement error increases more rapidly as the signal-to-noise ratio of the images decreases compared to the shear case, making flexion measurements extremely challenging in practice.

On top of this, another important issue has been raised by Viola et al. (2012), who pointed out how all these methods assume that the measured distortions can simply be related to $\mathcal{F}$ and $\mathcal{G}$ flexions, despite this assumption being true only if the shear can be considered negligible and the galaxies are intrinsically circular. If this is not the case, as expected in realistic situations, and any of these assumptions is violated, Viola et al. (2012) showed that a considerable error is introduced on the inferred lens power.

In short, there are exciting theoretical reasons to go beyond the first-order image distortions ordinarily used in weak lensing studies, and try to measure flexion. However, a successful outcome is not guaranteed, because these measurements are very challenging from a practical point of view.

This is where this thesis starts.

In this work I present a detailed investigation into the problem of estimating flexion in realistic observational conditions. More precisely, we thoroughly studied the ability of different pipelines to recover, from noisy images, the shape of galaxies with the level of detail necessary to estimate the higher-order distortions imprinted by the flexion fields.

The thesis is organized as follows. The first three chapters revise the theoretical background necessary to understand the results presented afterwards. In particular, in Chapter 1, we review the observational and theoretical pillars on which the current cosmological paradigm, the ΛCDM model, rests. This provides us with the necessary tools to study the different weak gravitational lensing phenomena, upon which we dwell in Chapter 2. In this chapter we describe how characteristic shape distortions of lensed objects are defined in terms of the gravitational potential of the lens that induced them, and we briefly illustrate the main techniques currently used to extract information on the mass distribution of the lens, in the three different cases of lensing by galaxies, by galaxy clusters or by the large-scale structure. A review of the main shape measurement methods used in weak lensing studies is given in the first part of Chapter 3, while the second part of this chapter focuses on the problem of relating the amount of higher-order deformations observed in the shape of galaxies to the strength of the flexion fields. The following three chapters are

dedicated, instead, to describe the three different methods that we have tested on flexion measurements to conduct our investigation, as well as to report the results we obtained from these tests. All these three methods rely on the measurement of the surface brightness moments of the lensed images in order to construct estimators for the flexion-induced distortions. The first method, the DEIMOS algorithm for shear measurements developed by (Melchior et al., 2011), is presented in Chapter 4, where we describe two modifications that we have implemented in order to apply this pipeline to images of flexed galaxies, together with the results we obtained with them. Chapter 5 illustrates a second approach, which differs from DEIMOS only in the de-weighting procedure applied to correct for the effect of the weight function that needs to be used, when measuring the surface brightness moments of the images, in order to control the noise impact. At last, Chapter 6 focuses on the results obtained with *PCALens*, a new method recently developed within our group (Maturi, 2015, in prep.), which exploits principal component analysis to de-noise the images of galaxies and thus measure their shape. We, ultimately, summarize the main results of this thesis and draw our conclusions in the final Chapter.

Chapter 1

THE COSMOLOGY BEHIND

Cosmology aims to study the properties of the universe as a whole, it is thus not interested in individual objects, like stars or galaxies, but rather in the time and space in which these object are embedded. The goal is to understand how the universe formed and evolved and possibly shed light on its ultimate fate. The peculiarity of cosmology is that its object of study, the universe, is by definition unique. This means that empirical laws have to be formulated and theories have to be tested based on this unique representation of the universe we have. Despite this special situation, huge progress has been made in the last century in the understanding of our universe and cosmology has become a very flourishing research area, also thanks to the great technological development that characterized the last decades, providing an enormous amount of data, before unimaginable.

The work presented in this thesis must be inserted into this larger frame. By aiming to measure gravitational flexion we aim to test the actual cosmological model and get new and deeper insight into the structure formation process. Cosmology and the comprehension of our universe represents thus the ultimate goal.

This chapter is meant to provide an introduction to the basic mathematical structure of modern cosmology, as well as to give an overview of the observational pillars on which our comprehension of the universe has been built. The current standard paradigm of formation and evolution of the universe, the ΛCDM model, will be introduced together with the main concepts necessary to understand lensing theory and its applications discussed in the rest of the thesis. We will not provide here a complete and extended overview, for which we refer to Coles and Lucchin (2002); Dodelson (2003); Schneider (2015).

1.1   Fundamental cosmological observations

In this section we will present a series of observations that have played a key role in cosmology, opening the way to the development and establishment of the theory of Big Bang and, afterwards, of the ΛCDM model as standard models.

Hubble law and expansion of the universe

The first observational evidence of the expansion of the universe dates back to 1929, when Edwin Hubble, by measuring the distances and velocities of 24 "nebulae", realized that these objects were receding from the Earth with velocity proportional to their distance (Hubble, 1929). Even though these measurements had been already performed in the previous decade by Slipher (Slipher, 1917), it was Hubble to propose this bold interpretation and formulate the famous law:

$$v = H_0 d \, , \tag{1.1}$$

known today as the *Hubble law*. This law relates the velocity v of the galaxies to their distance d from us, through a constant of proportionality H_0, called the *Hubble constant*. The numerical value of H_0 is usually expressed in km s^{-1} Mpc^{-1}. Nowadays, there is a general consensus on values of H_0 around 70 km s^{-1}Mpc^{-1} (Planck Collaboration et al., 2015). However, since H_0 is very difficult to measure accurately, for many years there has been an uncertainty of about a factor of 2 in its value, with estimates of H_0 varying between ~ 50 km s^{-1}Mpc^{-1} and ~ 100 km s^{-1}Mpc^{-1}. For this reason, the Hubble parameter h was introduced, defined so that:

$$H_0 = 100 \, h \text{ km s}^{-1}\text{Mpc}^{-1} \, . \tag{1.2}$$

Even if, nowadays, the value of H_0 is determined with high precision, this convention remains and all distances and derived quantities are commonly expressed in terms of the parameter h.

To produce the famous diagram shown in figure 1.1, Hubble estimated the distances of the nebulae using the Cepheids as standard candles[1]. The velocities were measured, instead, by means of the shift of spectral lines z, interpreted as Doppler redshift and thus related to the velocity by:

---

[1]Cepheids are very bright variable stars whose period of variability is proportional to the absolute brightness. Thus, by measuring their apparent brightness and estimating the absolute magnitude from the period of variability, we can measure the distance of these stars. Actually, Hubble mistook the type of variable star and he mainly looked at RR Lyrae stars. The Hubble constant that he first derived was too large, because of the misinterpretation.
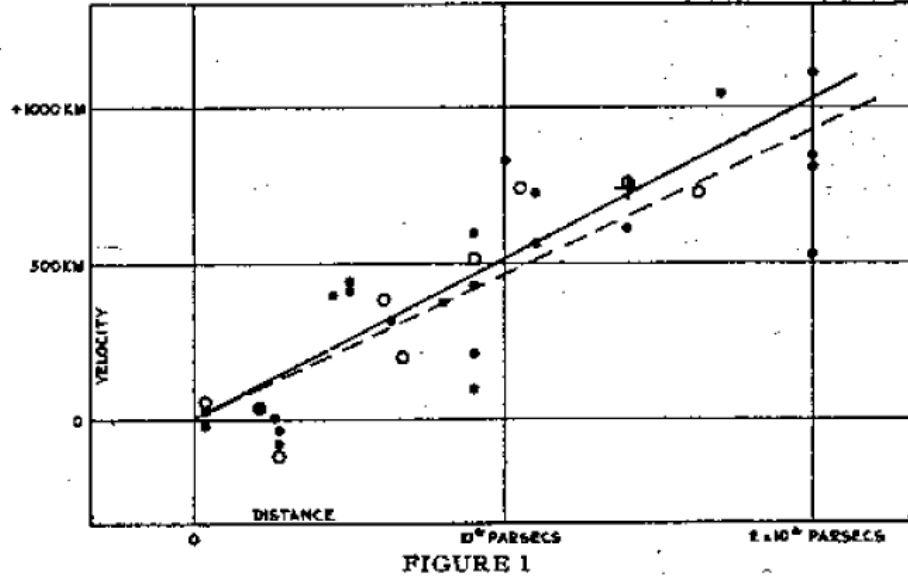
Figure 1.1: Original Hubble diagram published in Hubble (1929)

$$1 + z = \sqrt{\frac{1 + v/c}{1 - v/c}} \quad \xrightarrow{v \ll c} \quad z \sim \frac{v}{c}\,, \qquad \text{where } z = \frac{\lambda_{obs} - \lambda_{em}}{\lambda_{em}}\,. \qquad (1.3)$$

Light elements abundances

One key-point of the Big Bang theory is the possibility to predict, through the Big Bang nucleosynthesis (BBN, hereafter), the primordial abundances of four light elements (D, ^{3}He, ^{4}He, ^{7}Li), as first demonstrated by Alpher and Herman (1948) with their prediction of the abundance of helium.

The agreement found between theoretical predictions and observations represented a major success of the Big Bang theory and strengthened its establishment as standard model to describe the evolution of the universe since its earliest times.

According to this theory, in the early times the universe was much hotter and denser than now. Due to the vast amount of radiation in such a hot environment, the formation of composite nuclei was prevented, any atom or nucleus

produced was immediately destroyed by a high energy photon. However, while expanding, the universe gradually cooled till reaching temperatures well below the binding energies of typical nuclei, at this point, about 3 minutes after the Big Bang, light elements began to form. After five minutes from the beginning, most neutrons were bound in ^{4}He nuclei, while most protons remained free. Much smaller amounts of D, ^{3}He, and ^{7}Li were also synthesized. Due to the instability properties of elements with mass number 5 or 8 and to the low density conditions (making collisions between three nuclei far too rare to contribute to nucleosynthesis), heavier nuclei could not be formed and the composition of the universe remained the same for several hundred million years, until the formation of the first stars. Hence, knowing the conditions of the early universe and the relevant nuclear sections, the expected primordial abundances of the different elements can be calculated.

In 1999 a first comparison of the BBN predictions with accurate measurements of the light element abundances was made (Burles et al., 1999b). The amazing concordance that Burles et al. (1999b) found is shown in figure 1.2, where the boxes and arrows represent the observed values, while the colored strips the theoretical predictions.

It is interesting to note that BBN, beyond representing an important test of the Big Bang framework, can be used to estimate the *baryon density*[2] in the universe at the time of the nucleosynthesis, which can then be turned into the today's value with scaling arguments (as the universe evolves protons and neutron densities fall as a^{-3}). Following this strategy the baryon density has been constrained extremely accurately to only a few percent of the critical density[3]. Ordinary matter seems to account for not more than 5% of the total matter density. Hence, some other kind of, non-baryonic, matter must exist. We know refer to this "exotic" matter as *dark matter* (DM). Note that, even though this is not the only argument in favor of the existence of DM[4], it certainly represents a compelling one.

Cosmic Microwave Background

A fundamental contribution to what we know today about our universe was certainly brought about by the detection, and subsequent analysis, of the cosmic microwave background (CMB), a relic radiation of a hot dense phase in the early universe.

---

[2]With baryon density we mean the combined proton plus neutron density.

[3]See section 1.2.4

[4]Other arguments in favor of DM are based on the kinematic velocity curves of galaxies, the mass-to-light ratio of galaxy clusters, and the amplitude of cosmic microwave background fluctuations.
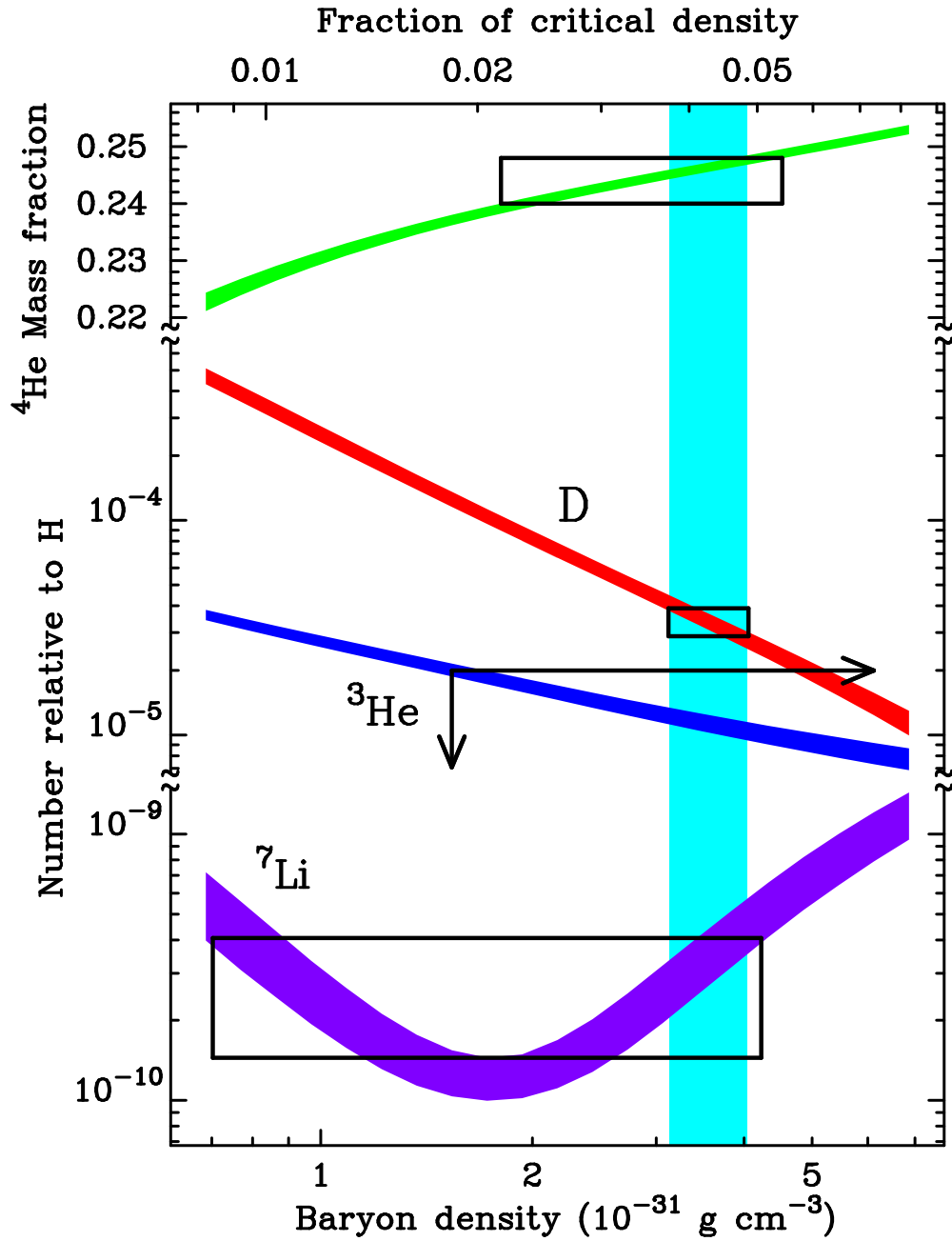
Figure 1.2: BBN nucleosynthesis predictions of the primordial abundances of light elements as a function of today's baryon density $\rho_{b,0}$ (in the lower axis), and of the corresponding density parameter Ω_b (in the upper axis), where it was assumed $h = 0.65$. The vertical extent of the boxes represents the corresponding measured values (top: ^{4}He, center: D, bottom: ^{7}Li; for ^{3}He there is only an upper limit, indicated by the arrows). The horizontal extent marks the region where the observations overlap with the theoretical predictions. The interval indicated by the vertical strip pinpoints the range of values of baryon density allowed by all the three species. Figure published in Burles et al. (1999b)

This radiation, whose presence is expected in the Big Bang framework, as first realized by Gamow in 1946, was accidentally detected by A. Penzias and R. Wilson in 1964. Indeed, while working at a horn antenna at Bell Laboratories, they measured an isotropic "excess antenna temperature" at 4080 MHz which "yielded a value of about 3.5 K higher than expected" (Penzias and Wilson, 1965).

According to the hot Big Bang model, in the early stages of the universe matter and radiation were in thermal equilibrium. The subsequent expansion, however, decreased the energy density of the primordial plasma until it became possible for electrons to combine with protons, forming hydrogen atoms and thus decoupling from the photons, that began to travel freely through space. This event, known as *recombination*, happened when the temperature was around 3000 K, and the universe was approximately 379000 years old.

The radiation emitted at recombination is expected to show a black body spectrum. Moreover, we expect to observe a certain amount of anisotropies in the CMB temperature map, due to the inhomogeneities in the universe at the epoch of recombination. The confirmation of both these predictions by the COBE satellite at the beginning of the 1990's represented two of the greatest successes of the Big Bang theory. In fact, COBE measured with extreme accuracy the spectrum of the CMB finding the most precise black body spectrum known in nature, as shown in figure 1.3. The same mission detected also very faint anisotropies of the CMB, it measured temperature fluctuations of the order of $\delta T/T = 1.8 \times 10^{-5}$ on angular scale of 7 degrees[5].

After COBE, many other experiments, both ground- and space-based, have studied the CMB properties and measured its anisotropies on smaller angular scales. In figure 1.4, we show the most recent map of the CMB temperature, as measured by the Planck satellite.

Finally, the temperature and polarization power spectra of the CMB have proven to be a gold mine of cosmological information. These spectra, in fact, depend sensitively on many cosmological parameters (see section 1.2.4) and thus can be used to constrain them. The temperature power spectrum of the CMB, as measured by Planck, is shown in figure 1.5, together with the best fit of the standard model of cosmology. We can see that on small and intermediate angular scales the observations agree extremely well with the model predictions, on large angular scales - between 90° and 6° - the fluctuations are about 10 per

---

[5]This value provided a strong argument in favor of the existence of DM. In fact, under the assumption of a purely baryonic universe, fluctuations of amplitude $\sim 10^{-3}$ are needed, at the epoch of recombination ($z \sim 1100$), in order to be able to form the structures we observed today. Only assuming the existence of a matter component that decouples from the radiation much earlier than baryons (and thus starts collapsing and creating potential wells much in advance) is possible to explain the structures we observe in the current universe.
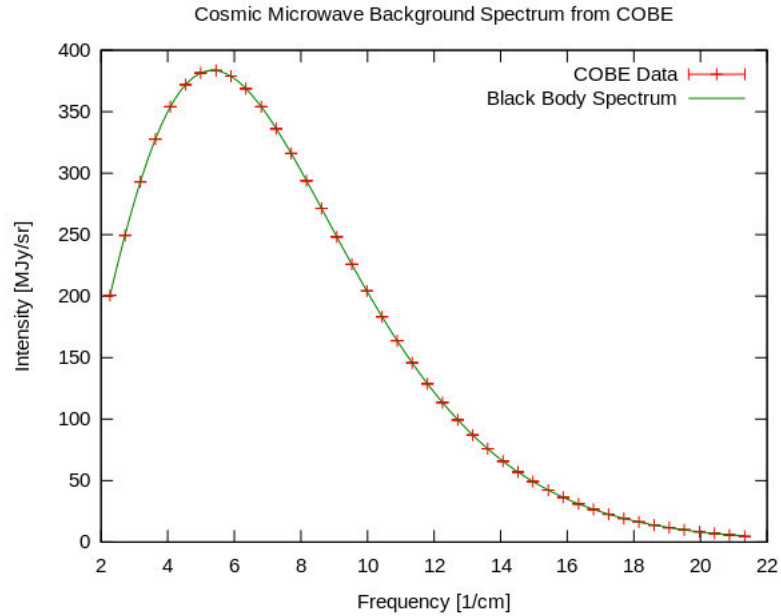
Figure 1.3: Cosmic microwave background spectrum measured by the FIRAS instrument on the COBE satellite. The error bars are too small to be seen even in the image. The observed data fit perfectly the theoretical curve (a black body spectrum at a temperature of 2.72 K). Credit: COBE/NASA

cent weaker than the best fit of the standard model to the data. In particular, there is one data point that falls well outside the range of allowed models. These anomalies in the Cosmic Microwave Background pattern might suggest that some aspects of the standard cosmological model may need to be rethought.

Summarizing, the CMB carries along an enormous amount of information about the early universe and its discovery certainly marked the beginning of a golden age for cosmology.

Galaxy distribution and inhomogeneities in the universe

The CMB represents strong evidence for the isotropy of the universe on large scales (≥ 100 Mpc h^{-1}). If we combined this isotropy evidence with the cosmological principle (see section 1.2.2), we can deduce that the universe is homogeneous. Nevertheless, this is obviously not valid on smaller scales, on which the universe appears strongly inhomogeneous, with the matter condensed in galaxies, clusters of galaxies and filaments.

Figure 1.6 gives us an idea of the aspect of the close-by universe and of
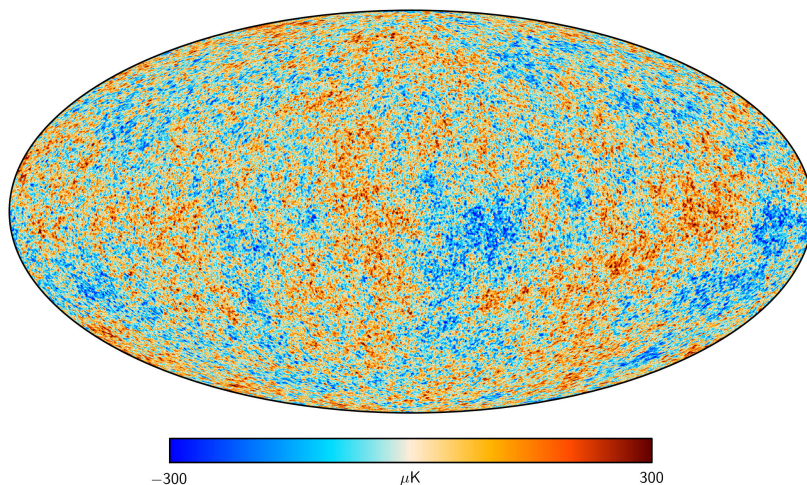
Figure 1.4: Full sky map of CMB temperature (Planck, Feb 2015). Credit: PLANCK/ESA

its inhomogeneities. The figure shows the three-dimensional distribution of $\sim 2.5 \times 10^5$ galaxies with redshift $z \leq 0.3$, as cataloged by the Two Degree Field Galaxy Redshift Survey (2dFGRS) (Colless et al., 2001). It appears that the galaxy distribution is not uniform at all, being instead characterized by filaments, sheets and clusters. Clusters are themselves grouped together in super-clusters, and large regions almost devoid of galaxies, called voids, appear in between these structures.

If we compare the amplitude of the density inhomogeneities today to those we observe in the CMB, it is clear that, in the course of its evolution, the universe became more and more inhomogeneous. As we will explain in section 1.3, density fluctuations grow over time due to self-gravity. One of the goals of modern cosmology is to explain this clustering by developing a theory for the evolution of structures within an expanding universe.

Type-Ia supernovae

At the end of the 1990's an unexpected discovery marked a turnaround in cosmology. Two different teams, the Supernova Cosmology Project and the High-z Supernova Search Team (Riess et al., 1998; Perlmutter et al., 1999), found, by investigating the relation between the apparent luminosity and the redshift of distant type Ia supernovae (SNIa), that the supernovae appeared
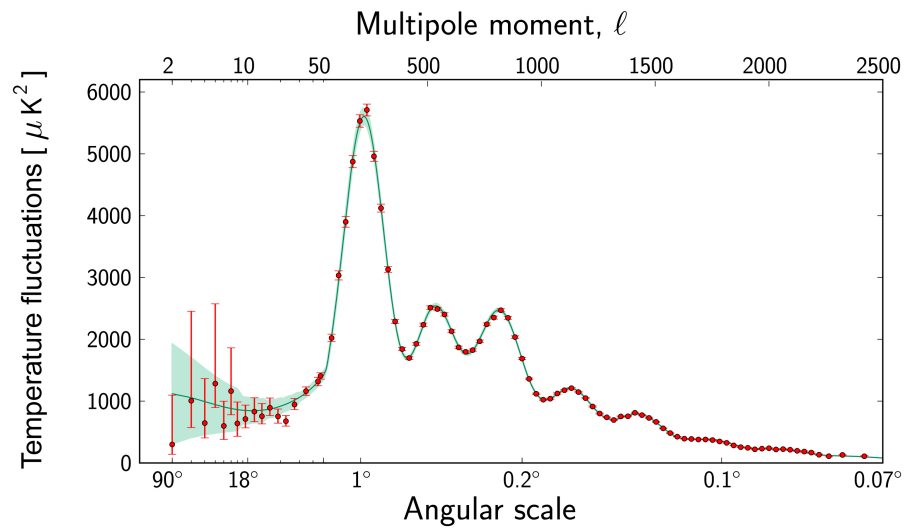
Figure 1.5: Power spectrum of the temperature fluctuations of the CMB. The red dots correspond to the Planck measurements. The error bars account for measurement errors, as well as errors due to cosmic variance. The green curve represents the best-parameter fit of the standard cosmological model (a flat ΛCDM model). The pale green area around the curve shows the predictions of all the variations of the standard model that best agree with the data. Credit: ESA and the Planck Collaboration 2013
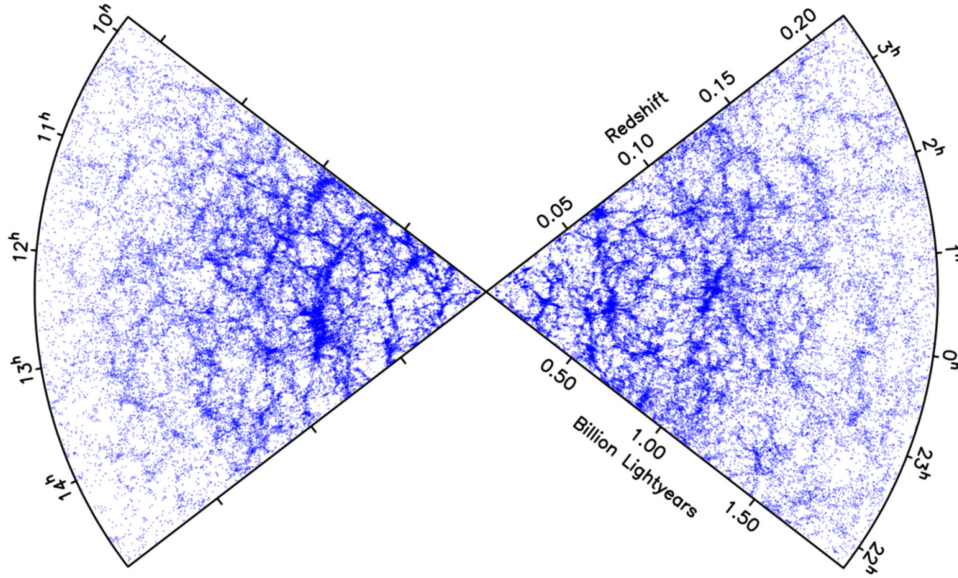
Figure 1.6: 3D distribution of more than 200000 galaxies from the 2dF Galaxy Redshift Survey. In the radial direction the redshift is plotted, while the polar angle is the right ascension. Our galaxy is at the center of the figure. Image taken from: http://www.2dfgrs.net/

dimmer[6] than expected in a Einstein-de Sitter universe[7] or in an open universe without cosmological constant (see figure 1.7). A non-vanishing *dark energy* component was then invoked to explain the observations. The plot in figure 1.7 provides thus the first observational evidence for an accelerated expansion of the universe, due to presence of dark energy, which in its simplest form is the cosmological constant Λ.

To conclude, we have observational evidence that our universe is expanding and is doing so in an accelerated fashion driven by an unknown dark energy component, it shows evidence of non-baryonic dark matter, is homogeneous and

---

[6]SNIa, which are the result of explosion processes of white dwarfs, can be used as standard candles, since there is a strong correlation between the luminosity and the shape of the light curve. By observing the light curve in several filters, it is possible to derive the maximum luminosity.

[7]An Einstein-de Sitter universe is a flat universe dominated by one single component ($\Omega_w = 1 = \Omega_{tot}$).
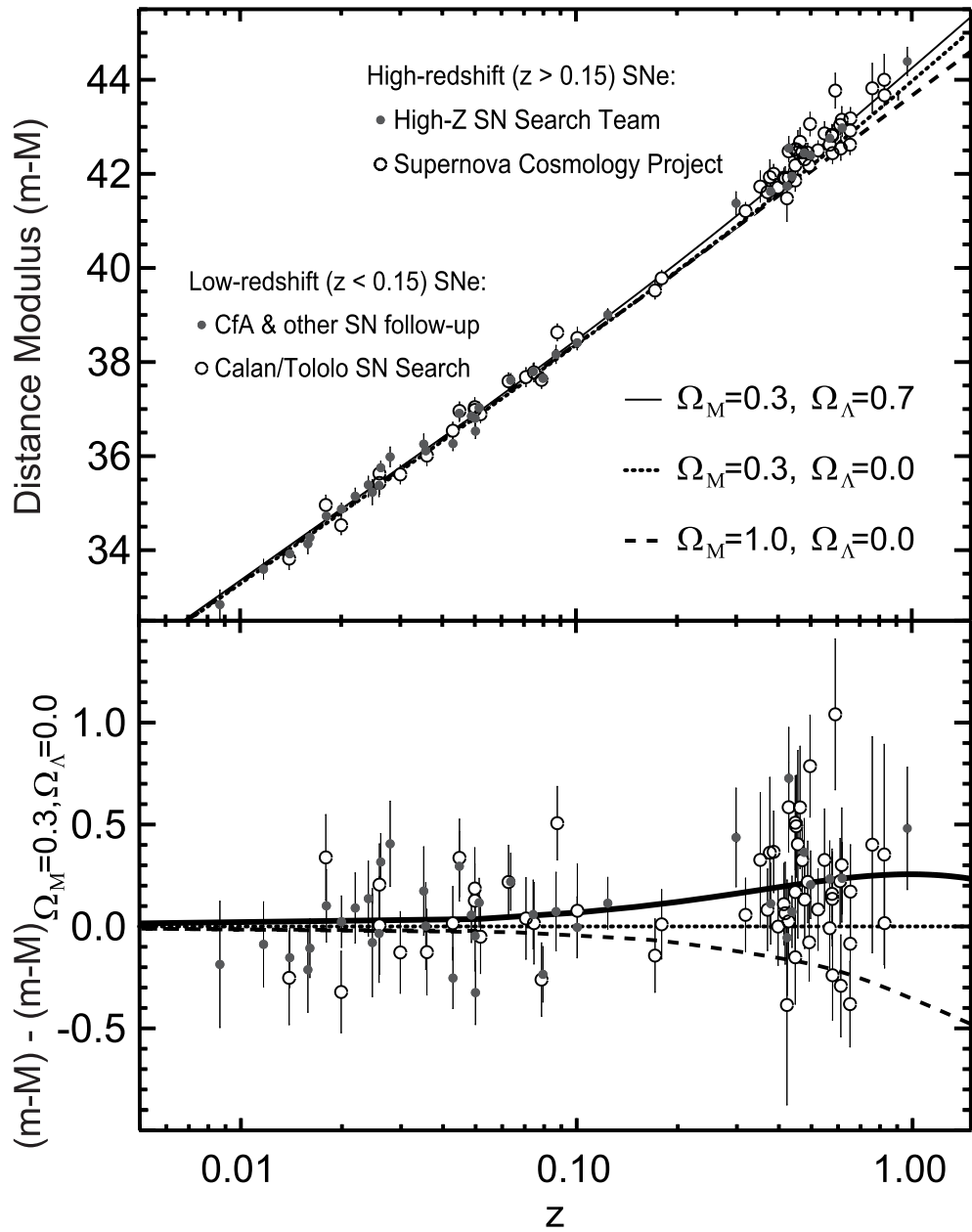
Figure 1.7: *Upper panel:* Hubble diagram for high redshift SNIa from both the High-z Supernova Search Team and the Supernova Cosmology Project. The curves represent theoretical estimations of distance modulus for different cosmological models. *Lower panel:* Residual of the distances relative to a ΛCDM model ($\Omega_M = 0.3$, $\Omega_\Lambda = 0.7$). Figure taken from: Perlmutter and Schmidt (2003)

isotropic on large scales, but inhomogeneous on small scales. Hence, any good model for the universe's evolution will have to account for these observations.

1.2   Theoretical background

Cosmology is built on two theoretical pillars: Einstein's general theory of relativity and the cosmological principle.

1.2.1   General Relativity

Up to now Einstein's theory of general relativity (GR) (Einstein, 1916) is the best description of gravitation we have. This theory essentially describes gravity as a geometric property of the space-time. J.A. Wheeler well summarized the main idea of general relativity: *"space-time tells matter how to move and matter tells space-time how to curve"*.

GR describes space-time as a four-dimensional manifold whose metric tensor $g_{\mu\nu}$ is a dynamical field. Its dynamics is governed by *Einstein's field equations*, which translate into mathematical terms the idea phrased in Wheeler's words, these equations in fact couple the metric to the matter-energy content of space-time:

$$G_{\mu\nu} = \frac{8\pi G}{c^2} T_{\mu\nu} + \Lambda g_{\mu\nu} \, , \tag{1.4}$$

where $G_{\mu\nu}$ is the Einstein tensor, which depends on the metric tensor and its first and second derivatives and describes the curvature of the space-time, $T_{\mu\nu}$ is the energy-momentum tensor of the cosmic fluid, an ideal fluid with pressure p and density ρ, and describes the content of matter and energy of the universe, c is the speed of light, G the Newtonian constant and Λ the cosmological constant. Hence, equation 1.4 tells us how the structure of the space-time is determined by the content of matter and energy and how, in turn, this structure determines the motion of matter and energy. GR is thus inevitably non-linear, making solutions of Einstein's equations generally very difficult to construct. The term $\Lambda g_{\mu\nu}$, initially introduced by Einstein to guarantee a static solution to the equations (thus a universe that is not expanding or contracting), can be interpreted as a source term for gravity corresponding to a vacuum energy density or as a new field, the dark energy, whose energy density may evolve with time.

1.2.2 Cosmological Principle

Cosmology rests on an important assumption, the *cosmological principle*. The cosmological principle is the assertion that, on sufficiently large scales (beyond those traced by the large scale structure of the distribution of galaxies) the universe is both homogeneous and isotropic. Note that the homogeneity is meant to be in space and not in time.

This principle was introduced into cosmology to simplify the mathematical description of the universe, when still very little was known about the real distribution of matter in our universe. With the discovery of the CMB and its isotropy, an observational justification for this principle became finally available.

1.2.3 FLRW metric and Friedmann's equations

The most general space-time metric describing a universe in which the cosmological principle holds is of the form:

$$ds^2 \equiv g_{\mu\nu}dx^\mu dx^\nu = -(c\mathrm{d}t)^2 + a(t)^2 \left[\mathrm{d}w^2 + f_K^2(w)(\mathrm{d}\theta^2 + \sin^2\theta\mathrm{d}\phi^2)\right] \ , \quad (1.5)$$

where we have introduced polar coordinates: w is the radial coordinate and (θ, ϕ) are the polar angles. To ensure homogeneity the radial function $f_K(w)$ has to be a trigonometric, linear or hyperbolic function of w (according to the value of the curvature K):

$$f_K(w) = \begin{cases} K^{-1/2}\sin(K^{1/2}w) & K > 0 \\ w & K = 0 \\ |K|^{-1/2}\sinh(|K|^{1/2}w) & K < 0 \end{cases} \qquad (1.6)$$

The *scale factor* $a(t)$ is responsible for the spatial stretching of the space-time and it can only be a function of time, in order not to violate isotropy. The spatial coordinates used in equation 1.5 are the *comoving coordinates*. These are the coordinates of an observer comoving with the Hubble flow, thus seeing the universe homogeneous and isotropic. The time coordinate t corresponds to the time measured by a clock moving with the Hubble flow.

This metric is known as the *Friedmann-Lemaître-Robertson-Walker metric* (FLRW metric). When using the FLRW metric in GR, we can derive from Einstein's equations a set of very useful equations, known as *Friedmann's equations*:

$$\left(\frac{\dot{a}}{a}\right)^2 = \frac{8\pi G}{3}\rho - \frac{Kc^2}{a^2} + \frac{\Lambda c^2}{3} \qquad (1.7)$$

$$\frac{\ddot{a}}{a} = -\frac{4\pi G}{3}\left(\rho + \frac{3p}{c^2}\right) + \frac{\Lambda c^2}{3} \tag{1.8}$$

(where the dot represents a derivative with respect to the cosmological time t). These equations describe the expansion of space filled by a homogeneous and isotropic perfect fluid with pressure p and rest energy density ρc^2, where all contributions from matter, radiation and vacuum or dark energy are included in ρ. Once an equation of state relating p and ρ is assumed, Friedmman's equations tell us how the scale factor $a(t)$ evolves with time. By definition, the scale factor is set today to be $a_0 \equiv 1$.

Finally, it can be show that, in a FLRW metric, the following relation between the redshift, measured for the light emitted from a distant object, and the scale factor, at the time the light was emitted, holds:

$$a(t) = \frac{1}{1+z} \ . \tag{1.9}$$

1.2.4   Cosmological parameters

Over the years many different parameters have been introduced in cosmology. They represent a convenient way to describe the Universe and its content. For a long time their determination has represented a big challenge in cosmology, a huge step in this direction was made at the beginning of this century when satellites like WMAP and Planck provided extremely accurate measurements of the CMB anisotropies, allowing very accurate determinations of many of those parameters and marking the beginning of the precision cosmology era. In table 1.1 a list of the values of these parameters, according to the latest results of the Planck collaboration (Planck Collaboration et al., 2015), is given.

Hubble parameter

It is defined as the logarithmic change in the expansion rate:

$$H(t) \equiv \frac{\dot{a}}{a} \ . \tag{1.10}$$

It quantifies by how much the recession velocity of cosmic objects grows with their distance. It has the unit of an inverse time, but usually is given in units of km s^{-1} Mpc^{-1}. Its value at the present time $H_0 \equiv H(t_0)$ is the Hubble constant.

Furthermore, we can get a rough estimate of the age of the universe, by defining the Hubble time as the inverse of the Hubble constant:

$$t_H \equiv \frac{1}{H_0} \, , \tag{1.11}$$

Another useful quantity related to H_0 is the Hubble radius, defined as the product of Hubble time and speed of light:

$$R_H \equiv \frac{c}{H_0} \, , \tag{1.12}$$

which approximately estimates the radius beyond which objects recede from us, due to the expansion of the universe, at a rate greater than the speed of light.

Critical density

It is defined as:

$$\rho_{cr}(t) \equiv \frac{3H^2(t)}{8\pi G} \, . \tag{1.13}$$

It represents the density that the spatial sections of the universe would need to be geometrically flat. Its value today is:

$$\rho_{cr0} = 1.86 \times 10^{-29} h^2 g cm^{-3} \, , \tag{1.14}$$

which corresponds to about a galaxy mass per Mpc^3.

Mass density parameter

It is a dimensionless parameter obtained from the ratio of matter density (baryonic + dark) of the universe and critical density:

$$\Omega_m(t) \equiv \frac{\rho_m(t)}{\rho_{cr}(t)} \, . \tag{1.15}$$

It is also common to distinguish the contributions of ordinary matter and dark matter by splitting this parameter into two: $\Omega_b(t)$ and $\Omega_{DM}(t)$.

Radiation density parameter

It is the dimensionless density parameter associated to radiation:

$$\Omega_r(t) \equiv \frac{\rho_m(t)}{\rho_{cr}(t)} \, . \tag{1.16}$$

Cosmological constant density

It is possible to associate a density parameter also to the cosmological constant, in the following way:

$$\Omega_\Lambda(t) \equiv \frac{\Lambda}{3H^2(t)} \; .$$
(1.17)

Curvature parameter

This parameter is defined as:

$$\Omega_K(t) \equiv -\frac{Kc^2}{H^2(t)} \; .$$
(1.18)

We can now rewrite Friedmann's equation 1.7 in terms of the parameters introduced so far:

$$H^2(a) = H_0^2 \left[\Omega_{r0}a^{-4} + \Omega_{m0}a^{-3} + \Omega_{\Lambda 0}a^{-4} + \Omega_{K0}a^{-2} \right] \; ,$$
(1.19)

where we have used the fact that $\rho_r = \Omega_{r0}\rho_{cr0}a^{-4}$ and $\rho_m = \Omega_{m0}\rho_{cr0}a^{-3}$, due to the different equations of state for radiation and matter[8]. If, moreover, we restrict to the case $a = 1$ (present time), we find the following relation:

$$\Omega_{K0} = 1 - \Omega_{r0} - \Omega_{m0} - \Omega_{\Lambda 0} = 1 - \Omega_{tot} \; .$$
(1.20)

The curvature parameter is thus related to the density parameters. As expected in GR, the geometry of space depends on the content of matter and energy.

Note that, not only the geometry, but also the evolution of the universe will depend on the content of matter and energy. In particular, if we neglect the radiation component in equation 1.19 (as reasonable for our universe where Ω_{0r} is very small), we can identify constraints on the values of Ω_m and Ω_Λ in order to have a specific expansion history. This is shown in a qualitative way in figure 1.8.

---

[8]Writing the equation of state as: $p = w\rho c^2$, we have $w = 0$ for matter, and $w = 1/3$ for radiation. This different behavior is at the origin of the different scaling of the matter and radiation densities with the expansion of the universe, since it can be shown that $\rho \propto a^{-3(w+1)}$.
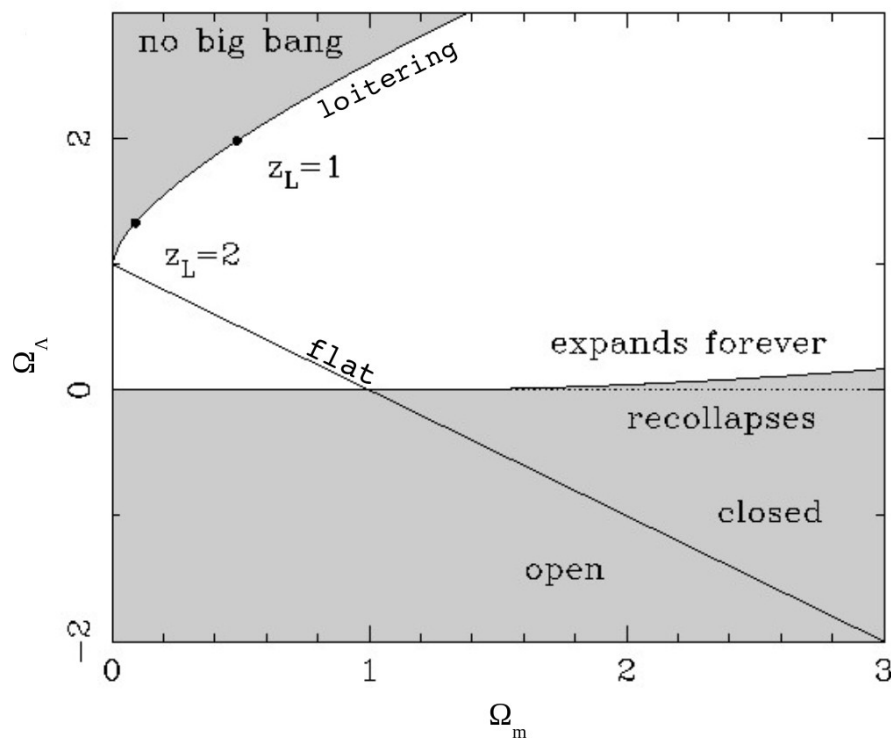
Figure 1.8: Possible cosmological models depending on the values of Ω_m and Ω_Λ (Ω_r is neglected since it is very small today). The straight solid line corresponds to flat models (those without curvature: $\Omega_K = 0$), and separates open ($\Omega_K > 0$) and close ($\Omega_K < 0$) models. The thin almost horizontal line separates models that will expand forever from those that will recollapse in the future. Also models with no big bang, where a has never been close to zero because of the repulsion of a positive Ω_Λ term, are possible. Figure adopted from: Peacock (1999)

	Planck	Planck+lensing	Planck+lensing+ext
H_0	67.31 ± 0.96	67.81 ± 0.92	67.90 ± 0.55
Ω_Λ	0.685 ± 0.013	0.692 ± 0.012	0.6935 ± 0.0072
Ω_m	0.315 ± 0.013	0.308 ± 0.012	0.3065 ± 0.0072
$\Omega_b h^2$	0.02222 ± 0.00023	0.02226 ± 0.00023	0.02227 ± 0.00020
Age(Gyr)	13.813 ± 0.038	13.799 ± 0.038	13.796 ± 0.029

Table 1.1: Values of the cosmological parameters mentioned in the chapter, as released by the Planck collaboration in 2015 (Planck Collaboration et al., 2015). For each parameter three different estimates are presented. *First column:* best fit obtained using only the Planck temperature power spectrum; *second column:* Planck temperature data in combination with lensing reconstruction; *third column:* Planck temperature data + Planck lensing + external data (BAO, SNIa, H_0).

1.2.5   Distances in cosmology

While in a static Euclidean space the separation between two points is unambiguously defined, this is no longer the case in a non-Euclidean or expanding/contracting space-time. For this reason, in cosmology, many different definitions of distance exist, which lead to different results. According to the particular situation we are interested in, one or the other definition will be preferred.

- **Proper distance:** It is the distance that the light covers to go from a source at redshift z_2 to an observer at redshift $z_1 < z_2$:

$$D_{prop}(z_1, z_2) = c \int_{a(z_1)}^{a(z_2)} \frac{\mathrm{d}a}{\dot{a}} \ . \tag{1.21}$$

- **Comoving distance:** It is the distance measured in comoving coordinates:

$$D_{com}(z_1, z_2) = c \int_{a(z_1)}^{a(z_2)} \frac{\mathrm{d}a}{a\dot{a}} \ . \tag{1.22}$$

The comoving distance between two observers moving with the cosmic flow does not change with time.

- **Angular diameter distance:** It is defined in such a way as to preserve the relation, valid in Euclidean space, between the angular size under which an object (at redshift z_2) is seen and its distance from the observer

(at redshift z_1):

$$D_A(z_1, z_2) = \left(\frac{\delta A}{\delta \omega}\right)^2 = a_2^2 f_K[w(z_1, z_2)] \,, \tag{1.23}$$

where we have used the fact that in a general space-time:

$$\frac{\delta A}{4\pi a_2^2 f_K^2[w(z_1, z_2)]} = \frac{\delta \omega}{4\pi} \,. \tag{1.24}$$

- **Luminosity distance:** Again defined in such a way as to preserve the relation between the luminosity of a source at redshift z_2 and the flux F that an observer at redshift z_1 receives:

$$D_L = \sqrt{\frac{L}{4\pi F}} \,. \tag{1.25}$$

In the limit of low redshifts all the distances coincide and we recover Hubble's expansion law:

$$D = \frac{cz}{H_0} + \mathcal{O}(z^2) \,. \tag{1.26}$$

1.3 Structure formation and the inhomogeneous universe

As we discussed in section 1.1, the universe on small scales is definitely not homogeneous. Indeed, we see pronounced structures in the matter distribution, on scales from stars to galaxy clusters and filaments. In our current understanding of the evolution of the universe, these structures can be related with the fluctuations observed in the temperature field of the CMB. Those primordial fluctuations represent the seeds from which gravitational instability began, increasing the density contrast between overdense and underdense regions and, finally, leading to the formation of the structures that we observe today.

The theory of structure formation is that branch of cosmology which aims to explain this precise process, investigating how the primordial fluctuations evolved over time. Rigorously, this theory should be worked out in the framework of GR, however it turns out that a good approximation can be obtained by working in the Newtonian framework, based on the fact that we can assume the inhomogeneities to be much smaller than the typical scale of the universe, and thus we can neglect effects of curvature and of the finite speed of light.

Within structure formation theory, the inhomogeneities are described in a cosmic fluid made of 3 components: radiation, dark matter and baryonic matter, which obeys Newtonian gravity. Their evolution is studied starting from the equations of motion for such a fluid, which, in Newtonian approximation, are represented by:

- *Continuity equation*, representing the mass conservation:

$$\frac{\partial \rho}{\partial t} + \boldsymbol{\nabla} \cdot (\rho \boldsymbol{v}) = 0 \ , \tag{1.27}$$

  where $\rho(t, \boldsymbol{x})$ and $\boldsymbol{v}(t, \boldsymbol{x})$ are the density and velocity of the fluid at position $\boldsymbol{x}$ and time t.

- *Euler's equation*, stating the conservation of momentum:

$$\frac{\partial \boldsymbol{v}}{\partial t} + (\boldsymbol{v} \cdot \boldsymbol{\nabla}) \boldsymbol{v} = \frac{\boldsymbol{\nabla} p}{\rho} + \boldsymbol{\nabla} \Phi \ . \tag{1.28}$$

  This equation describes how the velocity field evolves due to forces introduced by a pressure-gradient and the gravitational potential.

- *Poisson's equation*:
$$\nabla^2 \Phi = 4\pi G \rho \ , \tag{1.29}$$

  which relates the gravitational potential to the mass density.

When studying the evolution and growth of structures, two different regimes can be identified: *linear* and *nonlinear* evolution. To distinguish between these two regimes, we can refer to a quantity which is extensively used in structure formation theory, the so-called *density contrast*:

$$\delta(\boldsymbol{x}, t) \equiv \frac{\rho(\boldsymbol{x}, t) - \rho_0(t)}{\rho_0(t)} = \frac{\delta \rho}{\rho_0} \ . \tag{1.30}$$

Values of $\delta \ll 1$ denote linear evolution, while, when this condition is no longer verified, we enter in the nonlinear regime.

In the linear regime, it is possible to reduce the equations of motion mentioned above to a single differential equation for the density contrast. This is done by describing the density and velocity fields as given by a homogeneous background value plus a small perturbation. The solutions to this equation describe the evolution of the density contrast in time. They can be calculated analytically for the different eras which characterized the cosmic history. In particular, for each epoch, growing and decaying solutions, as well as oscillatory ones, are obtained, with the growing solutions being those responsible for
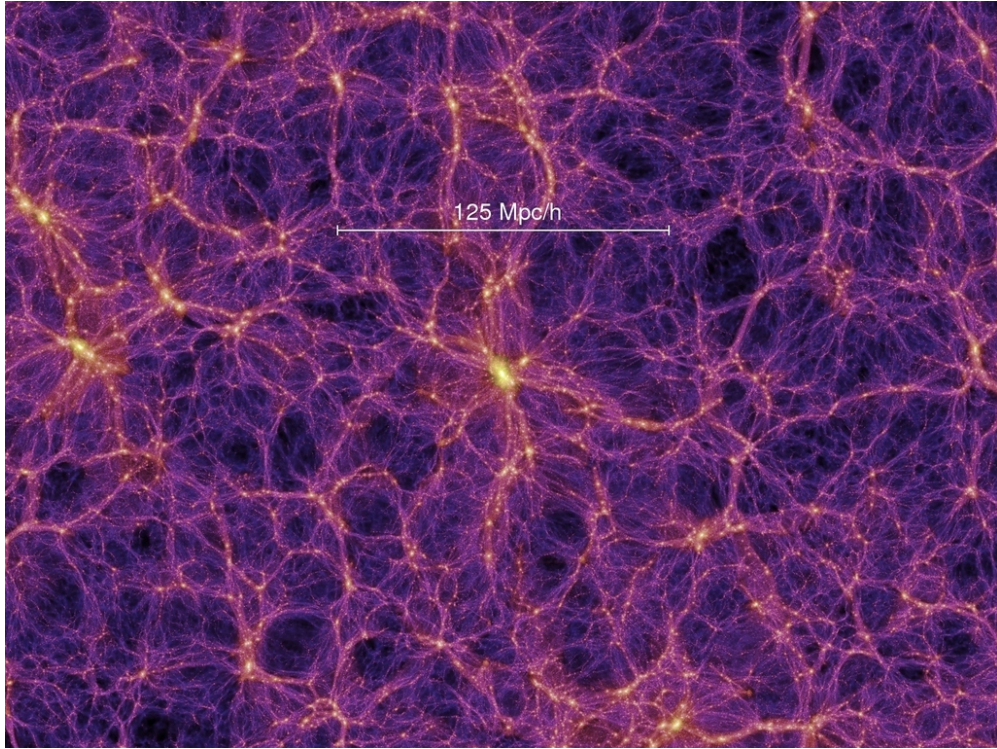
Figure 1.9: Snapshot from the Millennium simulation, showing the dark matter distribution at $z = 0$. We can see that the highest density peaks happen in the intersection of the cosmic web filaments. They correspond to galaxy clusters. Credit: Springel et al. (2005)

the growth with time of the tiny primordial fluctuations. A mathematical description of these phenomena is beyond the scope of this thesis, we referred to Padmanabhan (1993); Coles and Lucchin (2002); Dodelson (2003) for a detailed and complete overview of the linear theory of structure formation.

Clearly, due to the growth of perturbations, we will reach a point in which $\delta \gtrsim 1$, entering, then, the nonlinear regime. In this case, the assumption of small perturbation of the background fields is no longer valid and the equations of motion become very complicated to be solved analytically. To investigate the evolution of the density field at these late times, N-body simulations have become a standard tool in the last decades. The idea behind numerical simulations is to decompose the matter distribution into particles, transport them to redshifts high enough for linear evolution to hold on all scales considered, and follow their evolution by solving the equations of motion for all particles. The

outcome of these simulation, which have been characterized by increasingly larger volumes and larger number of particles, have confirmed that the matter in the universe is clustered, with the clustering happening along filaments at whose intersection highly nonlinear bound structures, representing the galaxies clusters, sit. A representation of the so-called *cosmic web*, obtained with the Millennium simulation[9] (Springel et al., 2005) is given in figure 1.9.

1.3.1   The ΛCDM model

As mentioned before, the current concordance model of cosmology is the ΛCDM model. This section is meant to gather the main features of this model which have been mentioned throughout the chapter, giving a brief summary of the, nowadays, most widely accepted cosmological paradigm.

The ΛCDM model is the simplest model that provides a reasonable description of the observational pillars that we introduced in section 1.1, i.e.:

- existence and properties of the CMB;

- abundances of hydrogen, deuterium, helium, and lithium;

- large scale structure in the galaxy distribution;

- accelerated expansion of the universe.

It is a parametrization of the Big Bang cosmological model in which the universe contains a cosmological constant, denoted by Λ, associated with dark energy, and cold dark matter (CDM).

In particular, according to the ΛCDM model the universe is flat and it is composed by baryons, radiation, dark matter and dark energy. The observations support: $\Omega_M \simeq 0.3$ and $\Omega_\Lambda \simeq 0.7$, while the contribution from radiation is negligible. The matter component is divided between standard baryonic matter, representing only $\sim 5\%$ of the energy content of the universe, and an unknown non-baryonic, dissipationless and collisionless matter, referred to as dark matter. Dark matter is considered to be cold, meaning that its velocity is much smaller than the speed of light at the epoch of radiation-matter equality.

In the CDM paradigm, structures grow hierarchically (*bottom-up scenario*), with small objects collapsing first under their self-gravity and then merging to form larger and more massive objects. Hence, one of the predictions of ΛCDM model is that dark matter halos are highly substructured. Unfortunately, it

---

[9]The Millennium run used more than 10^{10} particles to trace the matter distribution in a cubic region of the universe of side over 2 billion light-years, following them from redshift $z = 127$ to the present time.

is very hard to test this prediction observationally, since we cannot directly observe substructures in the halos of galaxies outside the local group.

Nowadays, one of the discrepancies between the ΛCDM predictions and the observations concerns exactly this point: cold dark matter simulations predict an overabundance of substructures in Milky-Way-size halos, compared to observations of the Milky Way dwarf galaxies (the so-called missing satellites problem, Klypin et al. 1999; Moore et al. 1999). An excellent tool to better investigate this problem could be represented by gravitational flexion. In fact, as we will explain in the next chapter, if flexion became routinely measurable, it would improve the spatial resolution of dark matter maps, hence, allowing the detection of substructures, otherwise inaccessible.

Though the ΛCDM model has repeatedly proved extremely successful in explaining observational data, some discrepancies, like the one we just mentioned, still exist between its theoretical prediction and observations. Finding new ways to test observationally the ΛCDM paradigm, and thus investigate if such discrepancies are real, represents then an important task for cosmologists.

Chapter 2

WEAK GRAVITATIONAL LENSING

2.1 Introduction

One of the main consequences of Einstein's general theory of relativity is that light rays are deflected by gravity. This deflection was observed for the first time in 1919 by F. W. Dyson, A. S. Eddington and C. Davidson, who, during a solar eclipse, measured the deflection induced by the gravitational field of the Sun on the light rays coming from stars close to the limb of our star. This measurement provided one of the earliest confirmations of the theory of general relativity.

According to this theory, photons move along null geodesics. In a curved space-time these geodesic lines are no longer straight lines. Thus, as a light ray propagates freely in a curved space-time, it is bent towards the mass that causes the space-time to be curved. This bending gives rise to several important phenomena:

- *multiple images*: multiple paths around a single mass become possible, we can then observe multiple images of a single source.

- *shape distortions*: the light deflection of two neighbouring rays may be different, that means light bundles are distorted differentially, as a result images of extended sources will appear distorted.

- *magnification*: since photons are not created neither destroyed by this bending, the surface brightness remains unchanged, however, the size is not conserved, implying that the distorted sources can either be magnified or demagnified.

- *time delays*: multiple light paths will be characterized by different lengths,

29
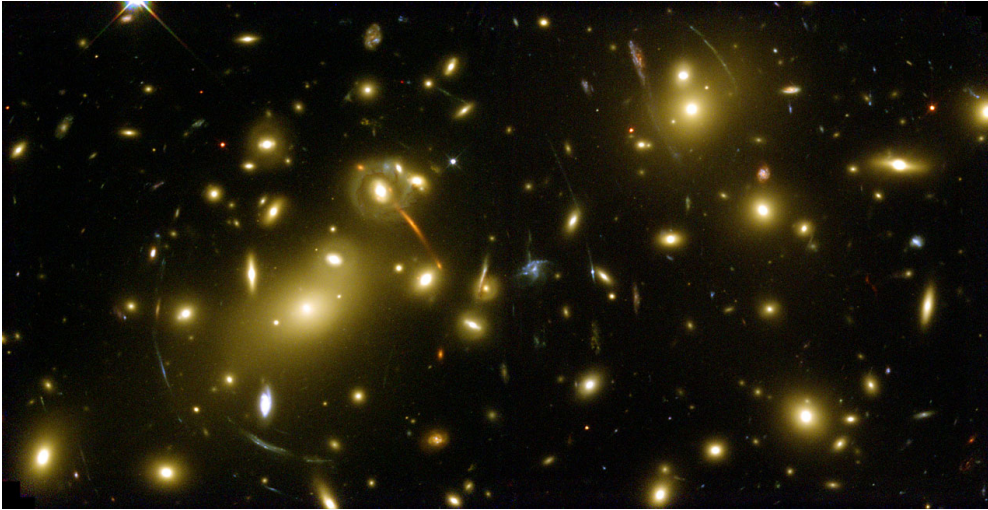
Figure 2.1: Galaxy cluster Abell 2218 as seen by the Hubble Space Telescope. Many strong lensing features, such as arcs and multiple images, can be seen. Credit: NASA, ESA

the travel time of the light will then differ for the different images, producing a time delay between different images of the same source.

The deflection of light by structures in the universe and the consequent phenomena mentioned above, are now referred to as *Gravitational Lensing*. All these phenomena have been observed in numerous cases.

The first gravitational lensed object (the quasar $SBS0957 + 561$) was observed in 1979 by Walsh et al. (1979). Some years later the first detection of giant arcs in galaxy clusters was published by Lynds and Petrosian (1986), but it was only in 1987, after the detection in Abell 370 of a blue structure with a ring-shape by Soucail et al. (1987), that Paczyński (1987) proposed to interpret these objects as gravitationally lensed background galaxies.

In the last decades many other cases of strong lensing (SL, hereafter) features have been observed and the list continues to grow. In figure 2.1 an image of a massive galaxy cluster taken with the Hubble Space Telescope is shown, in this cluster we can see many strong lensing features, such as giant arcs and multiple images.

Furthermore, clusters not only produce these giant luminous arcs, but also distort in a coherent way the images of faint background galaxies. This phenomenon is referred to as *weak gravitational lensing* (WL, hereafter), since these distortions are mostly weak and produce tiny deformations in the shape and orientation of the background sources. The corresponding images are re-

ferred to as arclets. Observations of these arclets can be used to reconstruct two-dimensional mass maps of the lens (Kaiser and Squires, 1993). The first cluster weak lensing analysis was done by Tyson et al. (1990). They detected for the first time a systematic alignment of 20-60 faint background galaxies centered on foreground galaxy clusters of high velocity dispersion. One decade later, in 2000, also weak gravitational lensing by the large-scale structure was observed for the first time. Several groups (Bacon et al., 2000b; Kaiser et al., 2000; Van Waerbeke et al., 2000; Wittman et al., 2000) measured coherent galaxy distortions in blind fields. We now refer to this phenomenon as *cosmic shear*.

Nowadays, the technique of gravitational lensing is a powerful tool in astrophysics. Lensing allows, indeed, to infer properties of the matter which induces the deflection independently of its dynamical status, it offers therefore an ideal way to detect and study dark matter and to investigate the growth of structures in the universe. Thanks to the magnification effect, it acts as a "cosmic telescope" allowing us to observe objects which are too distant or intrinsically too faint to be observed without lensing. Finally, it can be used to constrain important cosmological parameters, since many of the properties of individual lens systems or samples of lensed objects depend on the age, the scale and the overall geometry of the universe.

2.2 Gravitational lensing theory

In this section, we summarize the main concepts and equations that represent the basis for the description of light deflection by gravitational fields. In particular we concentrate on the theory necessary to describe weak gravitational lensing phenomena. For a complete overview on weak lensing we refer to Bartelmann and Schneider (2001), whose notation and logic is broadly followed in this chapter.

Granted the validity of Einstein's theory of general relativity, as well as of Maxwell's theory of electromagnetism, light propagates on the null geodesics of the space-time metric. The propagation of light in arbitrary curved space-times is in general a complicated theoretical problem. However, for almost all cases of relevance to gravitational lensing, a much simpler approximate description of light rays, which is called gravitational lens theory, is permitted.

In particular, we can assume that the overall geometry of the universe is well described by the Friedmann-Lemaître-Robertson-Walker metric and that the lensing is produced by local perturbations due to the matter inhomogeneities. Light paths propagating from the source to the observer, passing through the lens, can then be split into three distinct zones. In the first and third zone,

from the source to the lens and from the lens to the observer, light propagates through unperturbed space-time. While the deflection happens in the second zone, near the lens, where we can assume a locally flat Minkowskian space-time weakly perturbed by the Newtonian gravitational potential of the mass distribution constituting the lens. With this approach, which is legitimate if the Newtonian potential Φ is small, $|\Phi| \ll c^2$, and if the peculiar velocity v of the lens, with respect to the CMB rest frame, is small, $v \ll c$, we are able to study the light deflection induced by gravity in a much easier way. These conditions are satisfied in virtually all cases of astrophysical interest.

2.2.1   Deflection angle

Let's consider a very simple situation. A light ray departing from a background source S gets deflected due to the presence of a point mass M (the lens), as sketched in Fig.2.2. The magnitude and direction of the deflection are described by the so-called *deflection angle* $\hat{\boldsymbol{\alpha}}$, which depends on the mass of the deflector M and on the impact vector of the light ray $\boldsymbol{b}$. In the case of an impact parameter much larger than the Schwarzschild radius of the lens, general relativity quantifies this angle to be:

$$\hat{\boldsymbol{\alpha}} = \frac{4GM}{c^2} \frac{\boldsymbol{b}}{|\boldsymbol{b}|^2} \; , \tag{2.1}$$

once the *Born approximation*[1] has been used.

In reality any light ray gets deflected by many massive objects. Since the gravitational field can be considered weak, the field equations of general relativity can be linearized and therefore the total deflection angle is just the vectorial sum of the deflection angles caused by the single objects. In the continuum limit the sum becomes an integral over the density field along the line of sight:

$$\hat{\boldsymbol{\alpha}}(\boldsymbol{\xi}) = \frac{4G}{c^2} \int dz \int d^2\xi' \frac{(\boldsymbol{\xi} - \boldsymbol{\xi}')\rho(\boldsymbol{\xi}', z)}{|\boldsymbol{\xi} - \boldsymbol{\xi}'|^2} \; , \tag{2.2}$$

where z is the coordinate along the line of sight, and $\boldsymbol{\xi}$ is the two dimensional impact vector (orthogonal to the light path).

Furthermore, the dimension of the lens is typically much smaller than the distances between observer and lens and between lens and source[2]. This justifies

---

[1]In all cases of interest the deflection angle is very small, that means we can then approximate the potential along the deflected geodesic with the potential along the undeflected path.

[2]A cluster of galaxies, for instance, has a typical size of a few Mpc, whereas the distances D_d, D_s, and D_{ds} are fair fractions of the Hubble length $cH_0^{-1} = 3h^{-1} \times 10^3 Mpc$
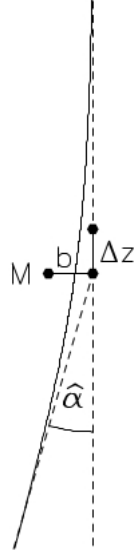
Figure 2.2: Light deflection by a point mass. The unperturbed light ray passes the mass at impact parameter b and is deflected by the angle $\hat{\alpha}$. Most of the deflection occurs within $\Delta z \sim \pm b$ of the point of closest approach. Figure taken from Narayan and Bartelmann (1996)

the usage of the *thin screen approximation*. The lens is approximated by a planar mass distribution, fully described by the surface mass density:

$$\Sigma(\boldsymbol{\xi}) = \int dz \rho(\boldsymbol{\xi}, z) \; , \tag{2.3}$$

which is simply the mass density projected onto a plane perpendicular to the line of sight, called the *lens plane*.

As long as the thin screen approximation holds, the deflection angle is given by:

$$\hat{\boldsymbol{\alpha}}(\boldsymbol{\xi}) = \frac{4G}{c^2} \int d^2\xi' \Sigma(\boldsymbol{\xi}') \frac{(\boldsymbol{\xi} - \boldsymbol{\xi}')}{|\boldsymbol{\xi} - \boldsymbol{\xi}'|^2} \; . \tag{2.4}$$

2.2.2 Lens equation

Making use of the expression calculated for the deflection angle and recalling the definition of angular diameter distance, we can now relate the true position

of the source to its observed position in the sky.

The situation is sketched in Fig. 2.3. A light ray departing from a source S at position $\boldsymbol{\eta}$ on the source plane and angular diameter distance D_s from us (the observer) is deflected by an angle $\hat{\boldsymbol{\alpha}}$ due to the presence of a mass distribution (the lens) at angular diameter distance D_d, and thus appears at position $\boldsymbol{\xi}$ on the image plane. The angle between the (arbitrarily chosen) optical axis and the true source position is $\boldsymbol{\beta}$ and the angle between the optical axis and the image I is $\boldsymbol{\theta}$, that means we can write: $\boldsymbol{\eta} = D_s\boldsymbol{\beta}$ and $\boldsymbol{\xi} = D_d\boldsymbol{\theta}$.

From Fig. 2.3, we can see that $\theta D_s = \beta D_s + D_{ds}\hat{\alpha}(\boldsymbol{\xi})$, where D_{ds} is the angular diameter distance between lens and source[3]. Therefore, the positions of the source and the image are related through the simple equation:

$$\boldsymbol{\beta} = \boldsymbol{\theta} - \frac{D_{ds}}{D_s}\hat{\boldsymbol{\alpha}}(D_d\boldsymbol{\theta}) \equiv \boldsymbol{\theta} - \boldsymbol{\alpha}(\boldsymbol{\theta}) \ , \tag{2.5}$$

where, for convenience, we have introduced the *reduced deflection angle* $\boldsymbol{\alpha} = \frac{D_{ds}}{D_s}\hat{\boldsymbol{\alpha}}$.

Equation 2.5 is called the *lens equation*, this fundamental equation, relating the true angular position $\boldsymbol{\beta}$ of the source to its observed position $\boldsymbol{\theta}$, is non-linear and admits in general more than one solution. This means that a source at a given position $\boldsymbol{\beta}$ can have multiple observed images.

It is now convenient to define the *critical surface mass density*:

$$\Sigma_{cr} = \frac{c^2}{4\pi G}\frac{D_s}{D_d D_{ds}} \ , \tag{2.6}$$

and the *convergence*, a dimensionless surface mass density:

$$\kappa(\boldsymbol{\theta}) = \frac{\Sigma(D_s\boldsymbol{\theta})}{\Sigma_{cr}} \ . \tag{2.7}$$

A lens with $\kappa > 1$ (that means $\Sigma > \Sigma_{cr}$) is called *supercritical*. A supercritical lens is a sufficient, but not necessary, condition to produce multiple images (Subramanian and Cowling, 1986). In this sense the convergence allows to define the threshold between strong and weak lensing: a mass distribution with $\kappa > 1$ constitutes a strong lens; the weak lensing regime, instead, is characterized by $\kappa \ll 1$.

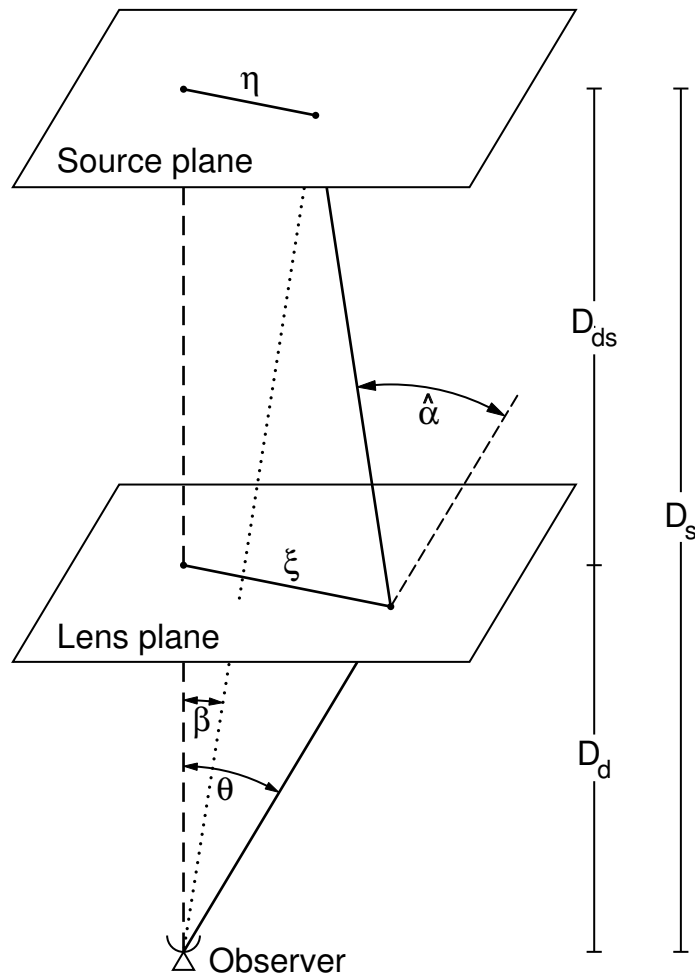[3]In general $D_d + D_{ds} \neq D_s$, since angular diameter distances are not additive.

Figure 2.3: Sketch of a typical gravitational lens system. Figure taken from Bartelmann and Schneider (2001)

2.2.3 Effective lensing potential

Given a certain distribution of matter, we can define its *effective lensing potential* as a properly scaled projection, along the line of sight, of the three-dimensional Newtonian potential of the lens:

$$\psi(\boldsymbol{\theta}) \equiv \frac{D_{ds}}{D_d D_s} \frac{2}{c^2} \int \Phi(D_d \boldsymbol{\theta}, z) dz . \tag{2.8}$$

The lensing potential has two important properties:

- the gradient of ψ is the reduced deflection angle:

$$\boldsymbol{\nabla}_\theta \psi = D_d \boldsymbol{\nabla}_\xi \psi = \frac{2}{c^2} \frac{D_{ds}}{D_s} \int \boldsymbol{\nabla}_\perp \Phi dz = \boldsymbol{\alpha} . \tag{2.9}$$

- the Laplacian of ψ is proportional to the surface mass density. In particular, we have:

$$\nabla_\theta^2 \psi = \frac{2}{c^2} \frac{D_{ds} D_d}{D_s} \int \nabla_\xi^2 \Phi dz = \frac{2}{c^2} \frac{D_{ds} D_d}{D_s} 4\pi G \Sigma = 2 \frac{\Sigma(\boldsymbol{\theta})}{\Sigma_{cr}} = 2\kappa(\boldsymbol{\theta}) , \tag{2.10}$$

where we have used Poisson's equation to relate the Laplacian of Φ to the mass density.

Given the validity of the two-dimensional Poisson's equation 2.10, between ψ and κ, we can write the effective lensing potential in terms of κ:

$$\psi(\boldsymbol{\theta}) = \frac{1}{\pi} \int \kappa(\boldsymbol{\theta'}) \ln |\boldsymbol{\theta} - \boldsymbol{\theta'}| d^2\theta' . \tag{2.11}$$

Hence, the deflection angle, which is the gradient of ψ, will be:

$$\boldsymbol{\alpha}(\boldsymbol{\theta}) = \boldsymbol{\nabla}\psi = \frac{1}{\pi} \int \kappa(\boldsymbol{\theta'}) \frac{\boldsymbol{\theta} - \boldsymbol{\theta'}}{|\boldsymbol{\theta} - \boldsymbol{\theta'}|^2} d^2\theta' . \tag{2.12}$$

2.2.4 Magnification and distortion

As we saw in section 2.2.1, the deflection angle is a function of the impact parameter $\boldsymbol{\xi}$. Thus, we expect extended sources (e.g. galaxies) to appear distorted, since light bundles will be deflected differentially in presence of matter along the line of sight.

We are now interested in quantifying the effect of gravitational lensing on the shape of the sources, and in finding a relation between the intrinsic shape

and the observed one. Ideally, we could determine the shape of the images by solving the lens equation for all the points within the extended source. In practice, however, the shape distortion is determined in a much simpler way, based on an important consideration. Liouville's theorem, together with the absence of emission and absorption of photons in the gravitational light deflection process, ensures that surface brightness is conserved by lensing. Hence, we will have:

$$I(\boldsymbol{\theta}) = I^s[\boldsymbol{\beta}(\boldsymbol{\theta})] , \qquad (2.13)$$

where $I^s(\boldsymbol{\beta})$ is the surface-brightness distribution in the source plane, and $I(\boldsymbol{\theta})$ is the observed one (in the lens plane).

If, moreover, the source is much smaller than the angular size on which the physical properties of the lens change substantially, we can locally expand the lens equation and truncate the expansion at low orders. In particular, in many weak lensing applications we can safely truncate the expansion to the first order. The distortion of the images is then described by the Jacobian matrix:

$$A \equiv \frac{\partial \boldsymbol{\beta}}{\partial \boldsymbol{\theta}} = \left(\delta_{ij} - \frac{\partial \alpha_i(\boldsymbol{\theta})}{\partial \theta_j} \right) = \left(\delta_{ij} - \frac{\partial^2 \psi(\boldsymbol{\theta})}{\partial \theta_i \partial \theta_j} \right) . \qquad (2.14)$$

In fact, the mapping between the image plane and the source plane is simply given by:

$$\beta_i \simeq A_{ij} \theta_j . \qquad (2.15)$$

Hence, if $\boldsymbol{\theta_0}$ is a point within an image, corresponding to the point $\boldsymbol{\beta_0} = \boldsymbol{\beta}(\boldsymbol{\theta_0})$ within the source, the invariance of the surface brightness, together with the locally linearised lens equation, provides:

$$I(\boldsymbol{\theta}) = I^s[\boldsymbol{\beta_0} + A(\boldsymbol{\theta_0})(\boldsymbol{\theta} - \boldsymbol{\theta_0})] . \qquad (2.16)$$

We introduce now an important quantity, the *shear* tensor, whose components are linear combinations of the second derivatives of the lensing potential:

$$\gamma_1(\boldsymbol{\theta}) = \frac{1}{2}(\psi_{,11} - \psi_{,22}) \equiv \gamma(\boldsymbol{\theta}) \cos(2\phi(\boldsymbol{\theta})) , \qquad (2.17)$$

$$\gamma_2(\boldsymbol{\theta}) = \psi_{,12} = \psi_{,21} \equiv \gamma(\boldsymbol{\theta}) \sin(2\phi(\boldsymbol{\theta})) , \qquad (2.18)$$

where $\gamma = (\gamma_1^2 + \gamma_2^2)^{1/2}$ and for convenience we have introduced the abbreviation:

$$\frac{\partial^2 \psi}{\partial \theta_i \partial \theta_j} \equiv \psi_{,ij} . \qquad (2.19)$$

Note that, because of the factor 2 in front of the angle ϕ, the two components of the shear are mapped into each other after rotations of $\phi = \pi$, rather than $\phi = 2\pi$, as it would be for vector components. The shear is therefore not a vector, but a trace-free symmetric tensor.

It is common to assign a property known as *spin* to weak lensing distortions. In particular, we will say that a lensing distortion has spin s, if it is invariant under rotations of $360°/s$. The shear is thus a spin-2 quantity.

If now we express also the convergence in terms of the lensing potential derivatives, making use of equation 2.10:

$$\kappa = \frac{1}{2}(\psi_{,11} + \psi_{,22}) \ , \tag{2.20}$$

we can rewrite the Jacobian matrix in following way:

$$A = \begin{pmatrix} 1 - \kappa - \gamma_1 & -\gamma_2 \\ -\gamma_2 & 1 - \kappa + \gamma_1 \end{pmatrix} \ . \tag{2.21}$$

In order to better understand the meaning of both convergence and shear, it is instructive to split a trace-free part off the Jacobian matrix. We can then re-express the distortion matrix as:

$$A = (1 - \kappa) \begin{pmatrix} 1 & 0 \\ 0 & 1 \end{pmatrix} - \gamma \begin{pmatrix} \cos 2\phi & \sin 2\phi \\ \sin 2\phi & -\cos 2\phi \end{pmatrix} \ . \tag{2.22}$$

The first term in the expression 2.22 is isotropic, that means it just re-scales the images by a constant factor in all directions; the second term, instead, introduces a stretch in the original shape of the source along one privileged direction. Hence, while the convergence isotropically enlarges or shrinks the images, the shear locally distorts them: the quantity γ describes the magnitude of the stretch and ϕ its orientation. This means that, as represented in figure 2.4, a circular source, whose angular size is much smaller than the characteristic angular scale on which the tidal field of the lens varies, is mapped into an ellipse, if κ and γ are both non-zero. The semi-major and -minor axes of the ellipse are:

$$a = \frac{r}{1 - \kappa - \gamma}, \qquad b = \frac{r}{1 - \kappa + \gamma} \ , \tag{2.23}$$

where r is the radius of the circular source. The orientation of the ellipse depends on the relative amplitudes of γ_1 and γ_2, as represented in Fig. 2.5.

The distortion introduced by lensing on the shape of objects has an important consequence. Since, as mentioned before, the conservation of surface brightness is ensured by Liouville's theorem together with the absence of emission and absorption of photons in the deflection process, a change of the solid
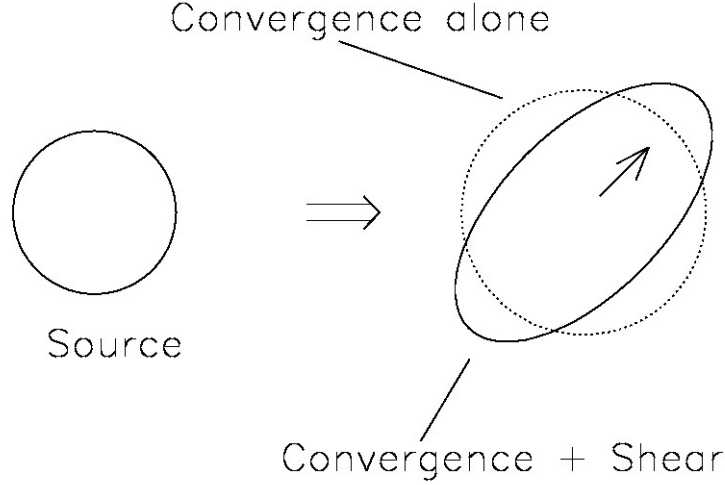
Figure 2.4: Distortions effects due to convergence and shear on a circular source. Figure from Narayan and Bartelmann (1996)

angle under which an object is seen implies that the flux received from the object is magnified (or demagnified). Therefore, the *magnification* is quantified by the ratio of the solid angles subtended by image and source, but this is simply the inverse of the determinant of the Jacobian matrix:

$$\mu = \frac{\delta\theta^2}{\delta\beta^2} = \det A^{-1} = \frac{1}{\det A} = \frac{1}{(1-\kappa)^2 - \gamma^2} \ . \tag{2.24}$$

Summarizing, lensing distorts both the shape and the size of the images. The tidal gravitational field described by the shear γ is responsible for the shape distortion, whereas the magnification is caused by both the isotropic focusing due to the convergence and the anisotropic one due to the shear.
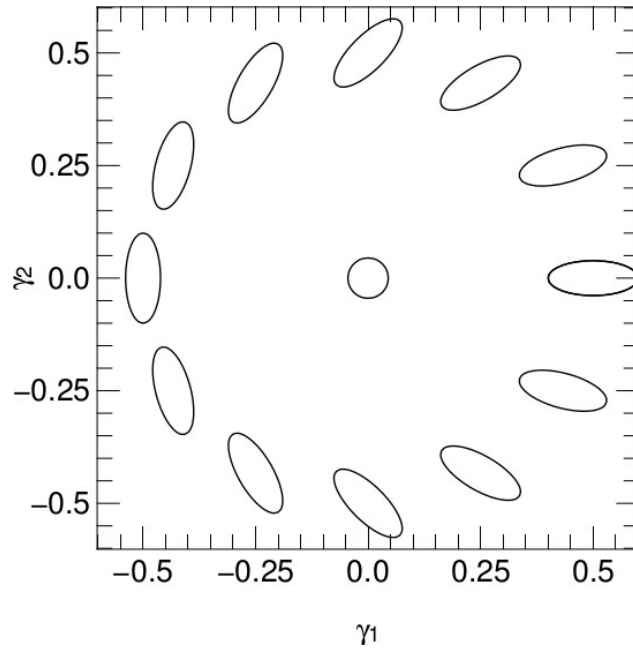
Figure 2.5: Effect of the relative amplitude of γ_1 and γ_2 on the shape and orientation of an originally circular source. Figure taken from Kilbinger (2015)

2.2.5   Complex notation

Before proceeding further with the gravitational lens theory, it is very useful to introduce a complex notation, that will be broadly used in the following. The notation consists in writing the two components of two-dimensional vectors, or the two components of the shear tensor, as complex quantities, e.g:

$$\gamma = \gamma_1 + i\gamma_2 \ . \tag{2.25}$$

Analogously we can define two complex operators by combining the components of the gradient:

$$\partial = \frac{\partial}{\partial\theta_1} + i\frac{\partial}{\partial\theta_2} \equiv \partial_1 + i\partial_2 \ , \qquad \partial^* = \partial_1 - i\partial_2 \ , \tag{2.26}$$

which in polar coordinates become:

$$\partial = e^{i\phi}\left(\frac{\partial}{\partial r} + \frac{i}{r}\frac{\partial}{\partial\theta}\right) \ , \qquad \partial^* = e^{-i\phi}\left(\frac{\partial}{\partial r} - \frac{i}{r}\frac{\partial}{\partial\theta}\right) . \tag{2.27}$$

The representation in polar coordinates shows clearly that when ∂ is applied to a spin-s quantity, it raises its spin by one, while ∂^* lowers the spin by one.

It is easily verified that, by applying these operators to the lensing potential, we can generate the convergence (spin-0) and shear (spin-2) fields:

$$\kappa = \frac{1}{2}\partial\partial^*\psi = \frac{1}{2}(\psi_{,11} + \psi_{,22}) \, , \tag{2.28}$$

$$\gamma = \frac{1}{2}\partial\partial\psi = \frac{1}{2}[(\psi_{,11} - \psi_{,22}) + 2i\psi_{,12}] \, . \tag{2.29}$$

2.2.6 Higher order distortions

As we said in section 2.2.4, when a source is much smaller than the angular scale on which the lens properties change, equation 2.15 is a sufficiently accurate approximation. If this is not the case, namely shear and/or convergence are not constant across the image of the source, equation 2.15 has to be extended to higher orders to encapsulate the variations in shear and convergence. We will then have:

$$\beta_i \simeq \theta_i - \psi_{,ij}\theta^j - \frac{1}{2}\psi_{,ijk}\theta^j\theta^k \, . \tag{2.30}$$

At this point, using the complex notation introduced in section 2.2.5, we can define two new lensing fields, which quantify how convergence and shear change across the image. They are obtained by applying the ∂ operator to convergence and shear, and we refer to them as $\mathcal{F} - flexion$ and $\mathcal{G} - flexion$, respectively:

$$\mathcal{F} \equiv \partial\kappa = \frac{1}{2}\partial\partial\partial^*\psi \, , \tag{2.31}$$

$$\mathcal{G} \equiv \partial\gamma = \frac{1}{2}\partial\partial\partial\psi \, . \tag{2.32}$$

It is easily seen that $\mathcal{F}$-flexion is a spin-1 quantity, while the $\mathcal{G}$-flexion has spin-3.

These two lensing fields are related to the third derivatives of the lensing potential. In particular, we have:

$$\mathcal{F} = \frac{1}{2}[(\psi_{,111} + \psi_{,122}) + i(\psi_{,112} + \psi_{,222})] \, , \tag{2.33}$$

$$\mathcal{G} = \frac{1}{2}[(\psi_{,111} - 3\psi_{,122}) + i(3\psi_{,112} + \psi_{,222})] \, . \tag{2.34}$$

As shown in Fig. 2.6, the flexion components give rise to characteristic image distortions. While the $\mathcal{F}$-flexion induces a skewness of the brightness
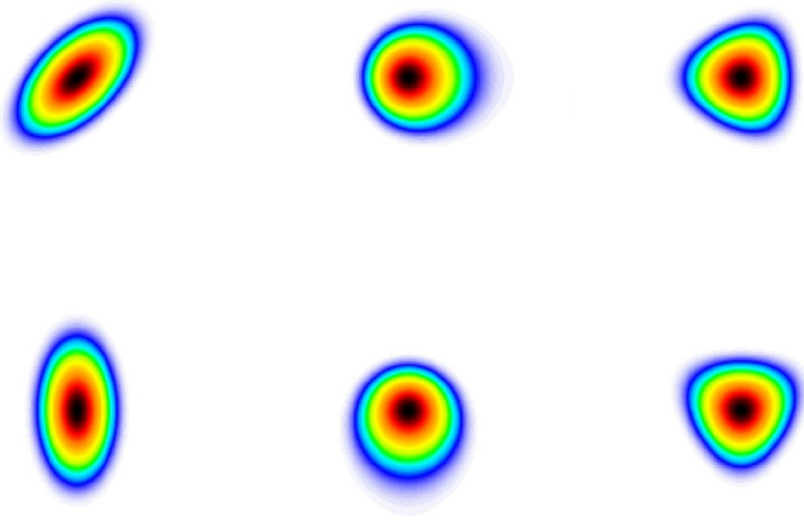
Figure 2.6: First and second order distortion on the image of a circular source. Effect of shear (left column), $\mathcal{F}$ flexion (middle column) and $\mathcal{G}$ flexion (right column). Figure taken from Bartelmann (2010).

profile, by shifting the centroid of the image, the $\mathcal{G}$-flexion creates a distortion with a three-fold rotational symmetry.

At this point we can rewrite equation 2.30, using our complex notation, in terms of the lensing fields so far introduced:

$$\beta \simeq (1 - \kappa)\theta - \gamma\theta^* - \frac{1}{4}\mathcal{F}^*\theta^2 - \frac{1}{2}\mathcal{F}\theta\theta^* - \frac{1}{4}\mathcal{G}(\theta^*)^2 \ . \qquad (2.35)$$

This equation relates the true and the observed position in terms of quantities obtained from specific combinations of the second- and third-order derivatives of the lensing potential and with well defined spin properties. Analogously to what we said in section 2.2.4 for the first order distortions, we can now use equation 2.35, together with the conservation of surface brightness, to get a description of the change induced by lensing in the shape of the images.

Every lensing field (convergence, shear, $\mathcal{F}$ and $\mathcal{G}$ flexion) will introduce, in an ideally circular source, a peculiar deformation of the object's shape, with specific rotational symmetry properties (as shown in Fig. 2.6). When combined all together these distortions cause the well-known banana shape (see Fig. 2.7),
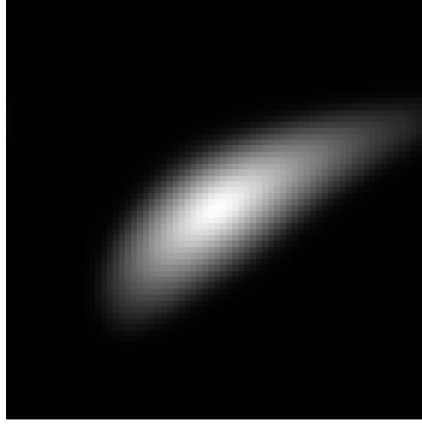
Figure 2.7: Shape of an intrinsically circular source after a lensing transformation, with non-zero values of both shear and flexion, has been applied.

characteristic of lensed galaxies. Measuring these deformations provides information on the shear and flexion fields, and, thus, on the derivatives of the lensing potential. How this is done in practice for the shear will be discussed in the next section, for the flexion we refer instead to chapter 3.

2.2.7 From shape measurements to shear

In general, galaxies are not intrinsically round, this means that the observed ellipticity will be a combination of intrinsic ellipticity and shear. Nevertheless, if we can assume the intrinsic ellipticities to be randomly oriented, an estimate of the shear can be obtained by locally average over many galaxy images.

In order to follow this strategy, we need first of all to find a definition for the ellipticity of a source, that is valid even when the source has more irregular shape or arbitrary isophotes, as this is the case for most faint galaxies. To this purpose the moments of surface brightness of the image turn out to be very useful.

Moments of surface brightness

Given an isolated source on the sky, whose surface brightness distribution is $I(\boldsymbol{\theta})$ (in the image plane), we define the moment of surface brightness of order $n = i + j$ as:

$$Q_{ij} \equiv \frac{\int d^2\theta I(\boldsymbol{\theta}) q_I[I(\boldsymbol{\theta})]\theta_1^i \theta_2^j}{\int d^2\theta I(\boldsymbol{\theta}) q_I[I(\boldsymbol{\theta})]} \ , \tag{2.36}$$

where $q_I(I)$ is a suitable weight function, chosen such that the integrals converge and that the noise contribution to the integral can be controlled.

The surface brightness moments can be used to describe some important properties of the image and quantifies its shape. In particular, the zero-order moment represents the observed flux of the source:

$$F = Q_{00} = \int d^2\theta I(\boldsymbol{\theta}) q_I[I(\boldsymbol{\theta})] \ . \tag{2.37}$$

The center of the image, instead, can be defined through the first-order moments:

$$\bar{\boldsymbol{\theta}} \equiv \frac{\int d^2\theta I(\boldsymbol{\theta}) q_I[I(\boldsymbol{\theta})]\boldsymbol{\theta}}{\int d^2\theta I(\boldsymbol{\theta}) q_I[I(\boldsymbol{\theta})]} \ . \tag{2.38}$$

For example, if $q_I(I) = H(I - I_{th})$, where H is the Heaviside step function, $\bar{\boldsymbol{\theta}}$ would be the center of light within the limiting isophote $I = I_{th}$ of the image.

The higher order moments can be used to construct quantities with the same rotational symmetry properties of the lensing fields we are interested in. Therefore, as we will explain in more detail in the following sections, using the surface brightness moments, we can build an estimator for each particular kind of distortion we want to study.

Note that, in complete analogy to what we have done for the image plane, we can define the moments of surface brightness in the source plane, we will just have to substitute $\boldsymbol{\theta}$ with $\boldsymbol{\beta}$ and $I(\boldsymbol{\theta})$ with $I^{(s)}(\boldsymbol{\beta})$ in the equations 2.38 and 2.36.

Now, employing the conservation of surface brightness together with the linearised lens equation (see eq. 2.16), we can obtain the transformation between the source and the image plane for the second order moments. In particular, if we define the tensor of second brightness moments in the following way:

$$\mathcal{Q} = \begin{pmatrix} Q_{20} & Q_{11} \\ Q_{11} & Q_{02} \end{pmatrix} \ , \tag{2.39}$$

the transformation between source and image plane for the second order moments is given by:

$$\mathcal{Q}^{(s)} = A\mathcal{Q}A^T = A\mathcal{Q}A \ , \tag{2.40}$$

where $A \equiv A(\bar{\boldsymbol{\theta}})$ is the Jacobian matrix at position $\bar{\boldsymbol{\theta}}$ and we have used the property that $A = A^T$ in the Born approximation.

Ellipticity and shear

The ellipticity of a given image, e.g. a galaxy, can now be quantified using the second-order moments of surface brightness. For this purpose we combine these moments in such a way to obtain a spin-2 quantity (since an ellipse has spin 2). In particular, it is very convenient to define the following two complex ellipticities:

$$\chi \equiv \frac{Q_{20} - Q_{02} + 2iQ_{11}}{Q_{20} + Q_{02}} , \qquad \epsilon \equiv \frac{Q_{20} - Q_{02} + 2iQ_{11}}{Q_{20} + Q_{02} + 2(Q_{20}Q_{02} - Q_{11}^2)^{1/2}} . \quad (2.41)$$

Note that both these quantities have the same phase (since they have the same numerator), but a different absolute value. For an image with elliptical isophotes of axis ratio $r \leq 1$, we will have:

$$\chi = \frac{1 - r^2}{1 + r^2} \exp(2i\phi) , \qquad \epsilon = \frac{1 - r}{1 + r} \exp(2i\phi) , \quad (2.42)$$

where ϕ is the position angle of the major axis (the factor 2 in the exponential assures that these ellipticities do not change if the image is rotated by π).

According to the context, one or the other definition of ellipticity can be more convenient. In any case, it is always possible to transform one into the other:

$$\epsilon = \frac{\chi}{1 + (1 - |\chi|^2)^{1/2}} , \qquad \chi = \frac{2\epsilon}{1 + |\epsilon|^2} . \quad (2.43)$$

Now, defining the complex ellipticity of the source $\chi^{(s)}$ in terms of $Q^{(s)}$, in analogy to what we have done for the image (eq. 2.42), we find, after some algebra, that ellipticities transform according to:

$$\chi^{(s)} = \frac{\chi - 2g + g^2 \chi^*}{1 + |g|^2 - 2\Re(g\chi^*)} ; \qquad \epsilon^{(s)} = \begin{cases} \frac{\epsilon - g}{1 - g^*\epsilon} & \text{if } |g| \leq 1 \\ \frac{1 - g\epsilon^*}{\epsilon^* - g^*} & \text{if } |g| > 1 \end{cases} \quad (2.44)$$

(Schneider and Seitz, 1995; Seitz and Schneider, 1997), where the asterisk denotes complex conjugation and g is the *reduced shear*:

$$g(\boldsymbol{\theta}) \equiv \frac{\gamma(\boldsymbol{\theta})}{1 - \kappa(\boldsymbol{\theta})} . \quad (2.45)$$

The inverse transformations are obtained by interchanging source and image ellipticities and replacing $g \to -g$ in the previous equations.

Equations 2.44 show that the ellipticity transformation does not depend on κ or γ separately, but only on their combination g. Hence the reduced shear g is the only quantity accessible through measurements of image ellipticities.

In the limit of 'weak' weak lensing, defined by the following conditions:

$$\left.\begin{array}{l} \kappa \ll 1 \\ |\gamma| \ll 1 \end{array}\right\} \Rightarrow |g| \ll 1 \ , \tag{2.46}$$

equations 2.44 become much simpler:

$$\chi \approx \chi^{(s)} + 2g \ ; \qquad \epsilon \approx \epsilon^{(s)} + g \ , \tag{2.47}$$

provided $|\epsilon| \approx |\epsilon^{(s)}| \lesssim 1/2$.

Local shear determination

As mentioned earlier, the observed ellipticity of a single background galaxy image is not sufficient to determine the local tidal gravitational field of the deflector, since the intrinsic ellipticity of the source is unknown. However, we can infer information on the local shear from a local ensemble of images, provided that the lens properties κ and γ do not change appreciably in the region where our images lie.

In fact, under the assumption that the intrinsic orientation of galaxies is random, the expectation value of the intrinsic ellipticities vanishes:

$$E(\chi^{(s)}) = 0 = E(\epsilon^{(s)}) \ . \tag{2.48}$$

Now, approximating the expectation value in the equations above by the average over a local ensemble of images, $\langle\chi^{(s)}\rangle \approx E(\chi^{(s)}) = 0$, using the ellipticity transformation laws obtained for the weak lensing limit (equations 2.47), and considering the case in which all sources are at the same redshift[4], we find:

$$\gamma \approx g \approx \langle\epsilon\rangle \approx \frac{\langle\chi\rangle}{2} \ . \tag{2.49}$$

Hence, the mean ellipticity of background galaxies in a patch of the sky near a deflector supplies us with a good estimate of the local (reduced) shear.

Note that equation 2.49 is valid under the simplifying assumptions of weak lensing ($\kappa \ll 1$, $|\gamma| \ll 1$) and the same redshift for all sources; if this is not the case, more generic relations between the average ellipticities, $\langle\epsilon\rangle$ or $\langle\chi\rangle$, and the reduced shear (or some function thereof) can be derived (see Schneider and Seitz (1995); Seitz and Schneider (1997)).

---

[4]This assumption, though not so realistic, applies approximately for clusters with low redshift.

2.3   Weak lensing in the universe

In this section we give a brief overview of the lensing phenomena produced by different kinds of extended lenses in the universe (galaxies, galaxy clusters, large scale structure) and we shortly outline the main techniques used to extract valuable information from the observation of these phenomena. For a complete and detailed overview we refer again to Bartelmann and Schneider (2001), and Schneider (2005).

As mentioned at the beginning, the lensing effects that we observe in the universe can be separated in two broad classes: *strong lensing* events (like multiple images or highly distorted images), that show up when the sources are at small angular distances from the centre of the lens and *weak lensing* events that, instead, appear in case of larger angular separations between source and lens.

We will here focus only on the weak lensing regime. This regime is characterized by the fact that the distortions are so weak that can hardly be recognized in individual images. However, they do show up across ensembles of images. In fact, since the distortion is coherent across regions on the sky surrounding the lens, it can be detected by averaging over a local ensemble of images. Weak lensing effects are therefore statistical in nature.

2.3.1   Weak lensing by galaxy clusters

Due to the very high number density of distant galaxies, clusters appear placed in front of a "cosmic wallpaper". Therefore, in addition to the occasional giant arcs, which are created when the angular separation between a source and the cluster center happens to be small, clusters also weakly distort the images of all those background galaxies. These weakly distorted images of faint galaxies are known as *arclets*. Arclets were first detected by Fort et al. (1988) in the cluster A 370.

Since the population of distant galaxies reaches a spatial density of about 30-80 galaxies per square arc minute at faint magnitude (Tyson and Seitzer, 1988), each cluster will show an order of 30-80 arclets per square arc minute, exhibiting a coherent pattern of distortions. These coherent distortions can be used to reconstruct the cluster mass distribution, independent of the physical state and nature of the matter, as first demonstrated by Tyson et al. (1990). The first systematic and parameter-free procedure to convert the observed ellipticities of arclets to a surface mass density map $\Sigma(\boldsymbol{\theta})$ of the cluster was developed by Kaiser and Squires (1993).

The Kaiser & Squires algorithm

In section 2.2.7 we described how the distortion of image shapes can be used to determine the local tidal gravitational field of the lens, e.g. a galaxy cluster. The method developed by Kaiser and Squires (1993) uses this information to construct two-dimensional mass maps of the cluster.

The technique is based on the fact that both convergence $\kappa(\boldsymbol{\theta})$ and shear $\gamma(\boldsymbol{\theta})$ are linear combinations of second derivatives of the effective lensing potential $\psi(\boldsymbol{\theta})$. If we transform ψ, γ and κ to Fourier space we find:

$$
\begin{aligned}
\kappa = \frac{1}{2}(\psi_{,11} + \psi_{,22}) &\quad \Rightarrow \quad \hat{\kappa} = -\frac{1}{2}(k_1^2 + k_2^2)\hat{\psi} \\
\gamma_1 = \frac{1}{2}(\psi_{,11} - \psi_{,22}) &\quad \Rightarrow \quad \hat{\gamma}_1 = -\frac{1}{2}(k_1^2 - k_2^2)\hat{\psi} \\
\gamma_2 = \psi_{,12} &\quad \Rightarrow \quad \hat{\gamma}_2 = -k_1 k_2 \hat{\psi} \ ,
\end{aligned}
\tag{2.50}
$$

where $\boldsymbol{k}$ is the two-dimensional wave vector conjugate to the angular position $\boldsymbol{\theta}$. We can then eliminate $\hat{\psi}$ from these relations and write the relation between κ and γ in Fourier space as:

$$
\begin{pmatrix} \hat{\gamma}_1 \\ \hat{\gamma}_2 \end{pmatrix} = k^{-2} \begin{pmatrix} k_1^2 - k_2^2 \\ 2k_1 k_2 \end{pmatrix} \hat{\kappa} \ ,
\tag{2.51}
$$

which immediately gives:

$$
\hat{\kappa} = k^{-2} \left(k_1^2 - k_2^2 \ , \ 2k_1 k_2 \right) \begin{pmatrix} \hat{\gamma}_1 \\ \hat{\gamma}_2 \end{pmatrix} \ .
\tag{2.52}
$$

This product in Fourier space can now be written as a convolution in real space, this yields:

$$
\kappa(\boldsymbol{\theta}) = \frac{1}{\pi} \int d^2\theta' [D_1(\boldsymbol{\theta} - \boldsymbol{\theta}')\gamma_1(\boldsymbol{\theta}') + D_2(\boldsymbol{\theta} - \boldsymbol{\theta}')\gamma_2(\boldsymbol{\theta}')] \ ,
\tag{2.53}
$$

whit:

$$
\begin{aligned}
D_1(\boldsymbol{\theta}) &= \frac{\theta_2^2 - \theta_1^2}{\theta^4} \ , \\
D_2(\boldsymbol{\theta}) &= \frac{2\theta_1 \theta_2}{\theta^4} \ .
\end{aligned}
\tag{2.54}
$$

Thanks to equation 2.53, we are now able to construct surface mass density maps of galaxy clusters from shear measurements. In fact, we can measure the shear field from the ellipticities of background galaxies (as explain in section 2.2.7), inserting it in the integral 2.53 we obtain $\kappa(\boldsymbol{\theta})$ and thereby $\Sigma(\boldsymbol{\theta})$. This is a remarkable result. However, several difficulties occur when we apply this

inversion technique to real data. They complicate the procedure, but they can all be overcome to some degree. We can summarize them as follows:

- Ellipticity measurements can be affected by different effects due to the atmosphere or the optical system used. The atmospheric turbulence (*seeing*) causes the images taken with ground-base telescopes to be blurred, galaxies appear then more circular than they actually are, producing an underestimation of the shear signal. On the other side, an anisotropic point spread function (PSF), or a PSF that varies across the field of view, will introduce spurious signal. All these effects can, in principle, be estimated and corrected for, however this requires high precision and is therefore challenging.

- The need to average over several background galaxies to get an estimate of the shear introduces a resolution limit to the cluster reconstruction. Assuming 50 galaxies per square arc minute, the typical separation of two galaxies is $\sim 8''$; thus, if the average is taken over ~ 10 galaxies, the spatial resolution is limited to $\sim 30''$.

- The mean ellipticity $\langle \epsilon \rangle$ is a good estimator for the shear only in the weak lensing limit. Hence, in the central region of the cluster, where the weak lensing assumption may not hold, the surface mass density obtained with the Kaiser & Squires technique will be biased low.

- The surface mass density is determined, by equation 2.53, only up to an additive constant. This is due to the fact that the transformation $\kappa' \to \lambda\kappa + (1 - \lambda)$, with λ an arbitrary scalar constant, leaves the reduced shear g invariant (Schneider and Seitz, 1995; Falco et al., 1985). This degeneracy, known as *mass sheet degeneracy*, cannot be broken if only shape measurements are used. However, it is possible to lift the degeneracy by taking into account magnification effects, as proposed by Broadhurst et al. (1995) and Bartelmann and Narayan (1995). In particular, while Broadhurst et al. (1995) proposed to measure the magnification by comparing the galaxy counts in cluster fields and in unlensed "empty" fields, Bartelmann and Narayan (1995) proposed to compare the sizes of the galaxies in these two kinds of fields.

- The integral in 2.53 extends over the entire plane $\boldsymbol{\theta}$, however, observational data are available only over a finite field (relatively small). Since we have no information on the shear outside the data field, the integration range has to be restricted, that means we have to set $\gamma = 0$ outside the data field. This cut-off in the integration can produce quite severe

boundary artifacts in the mass reconstruction. Modified reconstruction kernels have been proposed to overcome this limitation (Schneider, 1995; Kaiser et al., 1995b; Bartelmann, 1995; Seitz and Schneider, 1996; Lombardi and Bertin, 1998, 1999), a comparison between these finite-field inversion techniques can be found in Seitz and Schneider (1996) and in Squires and Kaiser (1996). An alternative approach based on the reconstruction of the lensing potential ψ (rather than κ), through a finite-field Maximum-Likelihood method, has been developed by Bartelmann et al. (1996). The method looks for the values of $\psi(\boldsymbol{\theta})$ on a finite grid that optimally reproduce the magnifications and distortions observed in the different grid cells.

- With the Kaiser & Squires reconstruction technique we obtain $\kappa(\boldsymbol{\theta})$, in order to calculate the surface mass density $\Sigma(\boldsymbol{\theta})$, we must then know the critical density Σ_{cr}, but this quantity depends on the redshift of the sources[5]. However, if the sources are at much higher redshift than the cluster, the influence of the source redshift can be neglected. Therefore, for low redshift clusters, we do not need to worry about this uncertainty.

2.3.2   Galaxy-galaxy lensing

Even though galaxies are much less massive than galaxy clusters, they can still act as lenses and deflect the light of background sources. The weak gravitational lensing effects induced by galaxies provide then a tool to study their mass profiles, in particular they allow us to investigate the profiles at very large radii (beyond ~ 100 kpc), where the standard dynamical studies are not applicable because of the lack of luminous tracers[6]. Indeed, the fact that we can observe these lensing effects at all galacto-centric distances makes them the perfect candidate for the missing dynamical tracers at large radii.

However, it has to be noticed that these effects are so weak that they cannot be detected on individual galaxy basis, due to the inherently random intrinsic shapes of the background sources. Nevertheless, even though the mass properties of individual galaxies cannot be accessed, we can study the statistical mass properties of a population of galaxies by superposing the signal of several of such galaxies. Basically, after stacking these lens-source systems, what we

---

[5]For a lens with a given surface mass density, the distortion increases with increasing source redshift.

[6]The mass distribution of galaxies is usually probed by studying their dynamical properties. The rotational velocity curves or velocity dispersion profiles of, respectively, spiral and elliptical galaxies are reconstructed using luminous tracers, like: stars and gas, in the most inner regions (till ~ 10 kpc), and globular clusters, planetary nebulae and satellite galaxies at larger galacto-centric distances.

will observe is that, on average, background galaxies are oriented tangentially to the transverse direction connecting lens and source; they thus seem to be aligned on a circular pattern around the lens, with the distortion decreasing in strength as the distance from the lens increases. Therefore, by measuring the average lensing distortion in circular bins of successively increasing size, centered on the lens, the density profile of the lens galaxy population can be studied in a statistical fashion.

The first attempt to detect such phenomenon was reported by Tyson et al. (1984), but we have to wait for the next decade to see the first detection and analysis of galaxy-galaxy lensing published by Brainerd et al. (1996).

In very short summary, the idea behind galaxy-galaxy lensing is the following: the lensing effect introduces a statistically tangential alignment of the background galaxies images with respect to foreground ones, and thus modifies the distribution of the position angles of the lensed galaxies (that will not appear anymore randomly oriented); by measuring this distribution, we can infer the mean shear due to the foreground galaxies and from it we can derive average properties of these galaxies.

Note that, while the shear components γ_1 and γ_2, introduced in section 2.2.4, are defined with respect to a Cartesian coordinate system, for galaxy-galaxy lensing it is more convenient to define the following two shear components, known as *tangential* and *cross* shear:

$$
\begin{aligned}
\gamma_t &= -\Re[\gamma e^{-2i\varphi}] = -2\gamma_1 \cos(2\varphi) - \gamma_2 \sin(2\varphi) \\
\gamma_\times &= -\Im[\gamma e^{-2i\varphi}] = \gamma_1 \sin(2\varphi) - \gamma_2 \cos(2\varphi) \ ,
\end{aligned}
\tag{2.55}
$$

with respect to the direction specified by φ. In our case, φ is the angle between the major axis of the source image and the line connecting image and lens. In full analogy to the shear, it is possible to define the tangential and cross components of an image ellipticity, ϵ_t and $\epsilon_\times$. An illustration of these definitions is given in figure 2.9.

Let us consider now the following situation: a foreground galaxy with axisymmetric mass distribution acts as a lens on a background galaxy, that appears at separation θ from the center of the lens. We assume to be in the weak lensing regime, meaning that we can approximate equation 2.44 with:

$$
\epsilon^{(s)} = \epsilon - \gamma \ .
\tag{2.56}
$$

If $p(\epsilon)$ and $p^{(s)}(\epsilon^{(s)})$ denote the probability distributions of the image and source ellipticities, then we can write:

$$
p(\epsilon) = p^{(s)}(\epsilon - \gamma) \sim p^{(s)}(\epsilon) - \gamma_i \frac{\partial}{\partial \epsilon_i} p^{(s)}(\epsilon) \ ,
\tag{2.57}
$$

$\varphi = 90°$
$\epsilon_t = 0.3$
$\epsilon_\times = 0.0$

$\varphi = 45°$
$\epsilon_t = 0.0$
$\epsilon_\times = 0.3$

$\varphi = 0°$
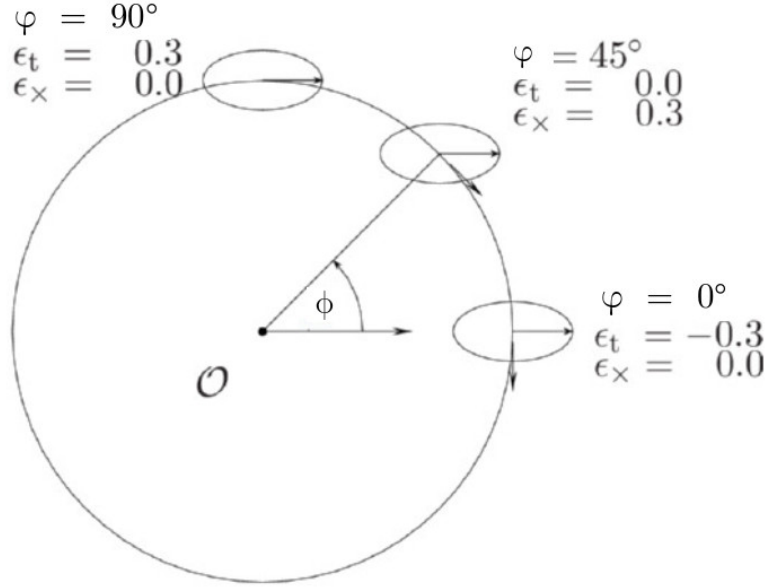$\epsilon_t = -0.3$
$\epsilon_\times = 0.0$

ϕ

$\mathcal{O}$

Figure 2.8: Illustration of the tangential and cross component of the ellipticity for an image with $\epsilon_1 = 0.3$, $\epsilon_2 = 0$, when varying orientation of the image φ with respect to the lens (located at the center $\mathcal{O}$). The cross component $\epsilon_\times$ will be null in two cases: for tangentially or radially oriented galaxy; in the first case, though, the tangential component ϵ_t is positive, while in the second case $\epsilon_t < 0$. A non-zero cross term, with no tangential component, means instead that the galaxy is oriented at $45°$ relative to the line connecting lens and image. The figure is taken from Schneider (2005)

having assumed the weak lensing limit, $|\gamma| \ll 1$. If φ is the angle between the major axis of the image ellipse and the line connecting source and lens, then the probability distribution of φ is obtained by integrating 2.57 over the modulus of ϵ:

$$p(\varphi) = \int d|\epsilon| |\epsilon| p(\epsilon) = \frac{1}{2\pi} - \gamma_t \cos(2\varphi) \frac{1}{2\pi} \int d|\epsilon| p^{(s)}(\epsilon), \qquad (2.58)$$

where φ varies within $[0, 2\pi]$. Because of the symmetry of the problem, we can restrict φ within $[0, \pi/2]$, so that the probability distribution reads:

$$p(\varphi) = \frac{2}{\pi} \left[1 - \gamma_t \left\langle \frac{1}{\epsilon^{(s)}} \right\rangle \cos(2\varphi) \right], \qquad (2.59)$$

showing a skewness towards values langer than $\pi/4$, that means a preferentially tangential alignment.

If we consider now an ensemble of foreground-background pairs of galaxies, instead of a single pair, the probability distribution for the angle φ simply becomes:

$$p(\varphi) = \frac{2}{\pi} \left[1 - \langle \gamma_t \rangle \left\langle \frac{1}{\epsilon^{(s)}} \right\rangle \cos(2\varphi) \right] , \qquad (2.60)$$

where $\langle \gamma_t \rangle$ is the mean tangential shear at separation θ.

Equation 2.60 shows us how we can get insight into the mass properties of the population of foreground galaxies. The function $p(\varphi)$ is an observable, thus $\langle \gamma_t \rangle$ can be determined once an estimate for $\left\langle \frac{1}{\epsilon^{(s)}} \right\rangle$ is known, which can be directly inferred from observed galaxy images. From $\langle \gamma_t \rangle$ we can then derive the average mass profiles of the foreground galaxies. For sufficiently large samples of galaxies, we can split the lens sample into several subsamples, e.g. according to their color, morphology, luminosity, etc. The mass properties can then be derived for each of the subsamples.

2.3.3 Cosmic shear

The treatment of weak lensing phenomena carried out so far considered the presence of one single lens along the line of sight (a localized mass concentration, like a galaxy or a galaxy cluster). However, light rays propagating through the universe are continuously deflected and distorted by the mass inhomogeneities along the path from the source, where they were emitted, till our telescopes. The coherent distortion of images of distant galaxies due to weak gravitational lensing by the large-scale structure in the Universe is referred to as *cosmic shear*.

Cosmic shear aims to infer cosmological information from the statistics of these distortions and has become a very important tool in observational cosmology over the last years, providing measurements of the expansion history of the universe and the growth of its structures. Even though it is quite challenging, first of all, because the distortions are very weak (on the order of a few percent) and therefore difficult to measure, and, second, because the light deflection does not occur any more in a lens plane but across a 3D matter distribution and thus a different description of the lensing optics is required, the rewards are potentially great. Indeed, the two-point correlation function of the image distortions gives direct information on the power spectrum of the density perturbations $P_\delta(k)$ in the universe.
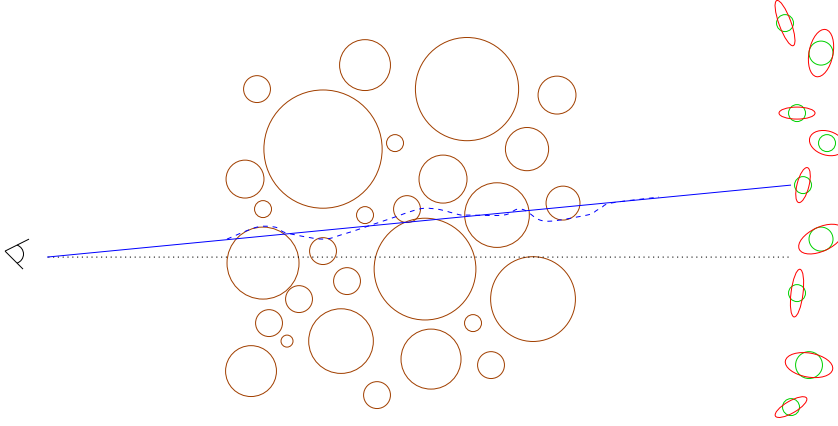
Figure 2.9: Illustration of the effect of weak lensing by large-scale structure. The figure is taken from Refregier (2003a)

Even though cosmic shear cannot make use of the thin lens approximation used to derive the lensing results so far presented, since the distortion does not take place in a localized region, it turns out that under the assumption that the deflection angle is small, the 3D cosmological mass distribution can be considered as an effective surface mass density κ_{eff}, just like in ordinary lensing.

In particular, it can be shown that the *effective convergence* has the following form:

$$\kappa_{\mathrm{eff}}(\boldsymbol{\theta}) = \frac{3H_0^2\Omega_m}{2c^2} \int_0^{w_H} dw\bar{W}(w)f_K(w)\frac{\delta(f_K(w)\boldsymbol{\theta}, w)}{a(w)} \ , \qquad (2.61)$$

where w is the comoving radial distance, $f_K(w)$ the comoving angular distance (whose functional form depends on the curvature K), $a = (1+z)^{-1}$ the scale factor, normalized to unity today, and we have used the 3D Poisson equation to replace the Laplacian of the potential with the density contrast δ:

$$\nabla^2\Phi = \frac{3H_0^2\Omega_m}{2a}\delta \ . \qquad (2.62)$$

The weighting function:

$$\bar{W}(w) \equiv \int_w^{w_H} dw' n(w')\frac{f_K(w-w')}{f_K(w)} \qquad (2.63)$$

takes into account that the sources might have a redshift distribution $n(w)$ and that the efficiency of the lenses varies along the line-of-sight. Finally, the upper intergration limit w_H is the comoving horizon distance, defined as the comoving distance obtained for infinite redshift $(a \to 0)$.

Note that the effective convergence is proportional to the matter density parameter Ω_m, not just to the density contrast δ.

Equation 2.61 is a direct consequence of the geodesic deviation equation in general relativity, we refer to Bartelmann and Schneider (2001) for a derivation of this result.

Ultimately, we are interested in the statistical properties of the effective convergence, since they will give us insight into the statistical properties of the matter density field. In particular, using Limber's equation[7], we can relate the convergence power spectrum to the matter density power spectrum:

$$P_\kappa(l) = \frac{9H_0^4\Omega_m^2}{4c^2} \int_0^{w_H} dw \frac{\bar{W}^2(w)}{a^2(w)} P_\delta\left(\frac{l}{f_K(w)}, w\right) , \qquad (2.64)$$

with the same weighting function given in equation 2.63. Equation 2.64 tells us that the power spectrum P_κ, if observable, can be used to constrain the 3D power spectrum P_δ and thus the cosmological parameters on which P_δ depends.

Analogously to the effective convergence an *effective shear* can be defined and it is possible to show that the statistical properties of convergence and shear, i.e. their power spectra, are the same.

Measuring the cosmic shear power spectrum is very interesting, since this quantity is sensitive to cosmology in three different ways: explicitly through the pre-factor Ω_m^2, through the geometrical factor $\frac{f(w-w')}{f(w)}$, and through the 3D matter power spectrum P_δ and its evolution with time.

In practice, however, the quantity that is measured is not the power spectrum P_κ but the two-point correlation functions of the shear components, which can be fully described in terms of P_κ. These functions are defined by considering pairs of galaxies at positions $\boldsymbol{\theta}$ and $\boldsymbol{\theta} + d\boldsymbol{\theta}$, and by defining the tangential and cross-component of the shear for this pair at these positions: $\gamma_t = -\Re(\gamma e^{-2i\varphi})$, and $\gamma_\times = -\Im(\gamma e^{-2i\varphi})$, as in 2.55, where φ is the polar angle of the separation vector. In particular, the following combinations of correlation functions of the two shear components turn out to be very convenient:

$$\xi_\pm(\theta) = \langle\gamma_t\gamma_t\rangle(\theta) \pm \langle\gamma_\times\gamma_\times\rangle(\theta), \qquad \xi_\times(\theta) = \langle\gamma_t\gamma_\times\rangle(\theta) . \qquad (2.65)$$

Due to parity symmetry, $\xi_\times(\theta)$ is expected to vanish, since under a mirror transformation $\gamma_t \to \gamma_t$, while $\gamma_\times \to -\gamma_\times$. The functions $\xi_\pm$, instead, are related to the power spectrum in the following way (Kaiser, 1992):

---

[7]It's an approximation introduced by Limber (1953) used to relate any projected correlation function to the spatial, three dimensional correlation function. We can make use of this approximation, if we assume that the density field varies on scales much smaller than the extent of the integration.

$$\xi_+(\theta) = \int_0^\infty \frac{dl\, l}{2\pi} J_0(l\theta) P_\kappa(l), \qquad \xi_-(\theta) = \int_0^\infty \frac{dl\, l}{2\pi} J_4(l\theta) P_\kappa(l) , \qquad (2.66)$$

where $J_n(x)$ is the n-th order Bessel function of the first kind.

The procedure to actually obtain $\xi_\pm$ is the following: all pairs of background galaxies on the data field with separation $d\theta$ from θ are selected and the average $\langle \epsilon_{ti}\, \epsilon_{tj} \rangle$ over all these pairs is evaluated, since in this regime $\epsilon_i = \epsilon_i^{(s)} + \gamma(\boldsymbol{\theta}_i)$, under the assumption that source ellipticities are uncorrelated, we will have $\langle \epsilon_{ti}\, \epsilon_{tj} \rangle = \langle \gamma_t\, \gamma_t \rangle(\theta)$. Similarly the correlation for the cross component is obtained.

Apart from the shear correlation functions $\xi_\pm$, there exist other second-order statistics of the cosmic shear, like the shear dispersion in a circular aperture and the aperture mass dispersion, that can be related to the power spectrum. We are here not interested to go into more detail, but for further information about two point shear statistics we refer to Bartelmann and Schneider (2001), and Schneider (2005).

In summary, the cosmic shear provides an ideal tool to investigate the large-scale structure of the cosmological density field, since it directly probes the total matter content of our universe without any need to relate luminosity and matter. In a universe dominated by cold dark matter few parameters determine the statistical properties of the mass distribution, among them Ω_m, Ω_Λ, the shape parameter of the power spectrum Γ, and the normalization of the power spectrum σ_8. Theoretical predictions of the cosmic shear signal obtained with different sets of these parameters can then be compared to observations in order to constrain these parameters. Furthermore, even tighter constrains can be obtained by combining the results from cosmic shear studies with the ones from Cosmic Microwave Background (CMB) analyses, since the degeneracy between different parameters is largely reduced in this case. Of course, from a practical point of view, measuring such a weak signal is not a trivial task and many technical difficulties are encountered and must be treated properly.

Chapter 3

SHAPE MEASUREMENT METHODS

When trying to estimate flexion from lensed images of background galaxies, we encounter two main difficulties. The first difficulty concerns the recovery and measurement of the galaxy shapes, while the second one regards the relation between the distortions we measure and the flexion fields that induced them.

The work presented in this thesis focuses on possible solutions to the first of these problems. We developed and applied three different methods to measure the shape of weakly flexed galaxies under realistic observational conditions. These methods and the results we obtained will be described in the next chapters. In this chapter, instead, we are going to shortly review the main shape measurements methods available today (mostly developed for shear measurements, but in some cases extended to address flexion measurements too), and we will introduce the flexion formalism necessary to understand the results presented in the next chapters. Finally, we will briefly discuss how we can relate the flexion fields to the shape distortions we aim to measure.

3.1   Shape measurements for weak lensing analyses

Measuring with high precision the shape of lensed galaxies is one of the most challenging aspects of weak lensing. In fact, as sketched in figure 3.1, any observed image is the result of different processes that contribute to modify and degrade the original shape.

First of all, when we observe a lensed galaxy, we have to consider that the optical system used to observe and the atmospheric turbulence (for ground-based observations) will smear out the light coming from the source. This blurring can be described mathematically as a convolution between the lensed image and the Point Spread Function (PSF), a function which characterizes the

response of the imaging system to a point source. A spherically symmetric PSF circularizes the object, while potential anisotropies in the PSF are translated into spurious distortions of the object. Hence, to avoid severe systematics in the measurements of the lensing fields, it is necessary to properly correct for the PSF effects.

Another important aspect that we have to consider is the pixelisation of the images we work with. In fact, astronomical data used for weak lensing are supplied by CCD images, these devices count the total number of photons arriving in a certain area of the detector, a so-called pixel. For the faint and small images, typical of weak lensing surveys, this inevitable pixelisation can severely influence the shape measurement.

Finally, the quality of the images is degraded by pixel noise, due to finite number of photons from source, CCD electronics and sky brightness.

Intrinsic shape   Gravitational   PSF convolution   Pixelisation   Noise
(unknown)   lensing distortions   (atmosphere and telescope)   (detector)
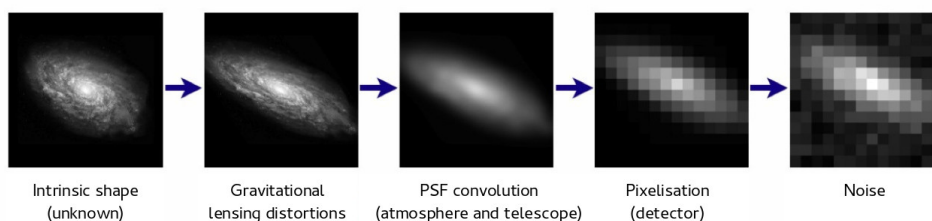
Figure 3.1: Figure adopted from Bridle et al. (2009)

In the last twenty years a lot of effort has gone into developing different techniques to extract lensing information from convolved and very noisy images of galaxies, though the focus has primarily been on shear estimates. A brief summary of the main methods available is given here, while we refer to Bridle et al. (2009) for a more complete overview.

Shape measurement methods for weak lensing applications can be separated in two big classes, *active* and *passive* techniques (Massey et al., 2007a). Active approaches start defining a model for the unlensed and unconvolved galaxy, then they apply a lensing transformation and they convolve the transformed image with a PSF model; finally, with a minimisation procedure they identify the values of the lensing fields that provide the best fit. On the other side passive approaches are based on the measurement of the moments of the surface brightness (SB moments, hereafter) of the convolved image. Shear and flexion estimators are then constructed from combinations of SB moments of second and third or fourth order, respectively. Finally, corrections for the PSF effects are applied.

3.1.1 Model-fitting methods

The general idea of this kind of methods is the following: given the image of a lensed galaxy, a model for the galaxy and one for the PSF are created, the convolved model is then compared to the observed image to understand how much the source has been lensed.

A large variety of model-fitting techniques exists, the main differences being related to the modeling of the galaxies or to the minimization technique used to find the best-fit parameters.

One possible way for modelling galaxies is to decompose them into a series of orthonormal basis functions, called *shapelets*, which are given by products of Gaussians with Hermite or Laguerre polynomials (in Cartesian or polar coordinates, respectively), as proposed by Bernstein and Jarvis (2002); Refregier (2003a); Refregier and Bacon (2003). A linear combination of these basis functions can model any compact image and can be used to filter out high frequency features such as noise. The shapelet basis functions are then sheared, to make them elliptical, and pixelised by being evaluated at the centre of each pixel. By decomposing also the PSF in shapelets, the convolution is obtained as a simple matrix multiplication, hence, the deconvolution can be done analytically through a matrix inversion (Refregier and Bacon, 2003). The transformation of shapelet coefficients under lensing transformations is quite simple, making the shapelet method well suited to shear measurement. On the other hand, the limit of this method is that it assumes galaxies to be well described by a Gaussian brightness distribution, which is often not the case. In particular, in order to reproduce the extended wings of a galaxy, a large number of basis elements has to be used, something which is usually difficult because of the noise dominating in the external parts of the galaxies. An improper modeling of the wings can introduce a systematic underestimation of the ellipticity and have even more severe consequences on the flexion measurements. Many different implementations of this method have been developed in the last years (Kuijken, 2006; Massey et al., 2007b; Nakajima and Bernstein, 2007; Velander et al., 2011). In particular, regarding flexion, Massey et al. (2007b) constructed flexion estimators based on the shapelets coefficients, while in Velander et al. (2011) the shapelet method has been applied to flexion measurement in galaxy-galaxy lensing.

A method related to shapelets is *Sersiclets* (Ngan et al., 2009; Andrae et al., 2011), in which galaxies are decomposed into a more realistic basis set derived from the Sérsic description of galaxy profiles (Sérsic, 1963, 1968). Furthermore, other methods exist, which model the galaxies as sums of elliptical Gaussians (Kuijken, 1999; Bridle et al., 2002; Voigt and Bridle, 2010).

The pipelines for shape measurements mentioned so far use likelihood-based

methods to determine the relevant parameters of the modelling. Another possibility, however, is to estimate these parameters using a Bayesian statistical approach, as it is done in LENSIFT (Miller et al., 2007; Kitching et al., 2008). This shear measurement pipeline models galaxies through the superposition of two Sérsic profiles (to represent the bulge and the disk components) and produces a likelihood surface in (ϵ_1, ϵ_2). This likelihood is then used in a Bayesian fashion to estimate the shear, once a prior for the intrinsic ellipticity distribution is assumed.

To conclude, model-fitting methods represent an optimal choice for strongly degraded data, since, thanks to the priors introduced, e.g. the source ellipticity smaller than one, the results are kept within reasonable bounds. However, if the data differ a lot from the expectations, unknown biases can affect the outcome.

3.1.2   Moment-based methods

As we saw in section 2.2.7 for the shear case, and as we will explain in more detail in section 3.2, a widespread approach for determining the shape of a galaxy image is based on the measurement of the SB moments of the image. The idea at the basis of the method is that it is possible to build, with these moments, some quantities with the same rotational symmetry properties of the distortions we want to measure, each of these quantities will thus represent an estimator for a specific kind of distortion (ellipticity, skewness, "bananinity", etc.). Note that, in most applications, a weight function is applied to the surface brightness when measuring the moments, in order to limit the effect of the noise. Even if necessary, this operation has an impact on the shape that we eventually measure, this effect needs then to be taken into account and possibly corrected for. The prototype of moments-based methods is the KSB method (Kaiser et al., 1995a; Luppino and Kaiser, 1997; Hoekstra et al., 1998), which also represents the first method historically used in weak lensing analysis. This method is easy to implement and very fast in performing. Its main limit, however, is the assumption made on the PSF shape. The PSF is, in fact, described by a convolution of a small, but highly anisotropic, distortion (representing effects of misalignments in the optics) with a large circularly symmetric function (representing the atmospheric turbulence effects). Moreover, KSB does not apply a proper deconvolution algorithm, but it gives an approximate PSF correction. Despite these shortcomings, the method has been highly successful in practical shear measurements and still competes well with newer methods. Many versions of KSB exist today, most of them measuring shear only (e.g. Bacon et al. 2000a; Erben et al. 2001; Heymans et al. 2005; Schrabback et al. 2007). The extension of KSB to flexion measurements is known as HOLICS (Higher Order Lensing Image Characteristics, Okura et al. 2007, 2008).

A substantial part of the work presented in this thesis is based on the algorithm DEIMOS (Melchior et al., 2011), which follows the general philosophy of KSB by working with multipole moments, and thus maintaining the strength of model-independent approaches, but adopts a different method to correct for the impact of the weight function on the measured ellipticity and does not rely on any assumption about the shape of the PSF. A detailed description of DEIMOS is given in chapter 4.

Most recently, some alternative moment-based methods, which aim to infer ensemble shears rather than per-object shears, have been introduced (e.g. Bernstein and Armstrong 2014, Zhang et al. 2015). The algorithm proposed by Bernstein and Armstrong (2014) is based on the measurement of the SB moments in Fourier space and employs a Bayesian technique. The method requires the unlensed distribution of galaxy moments as a prior, as well as derivatives of this prior under applied shear. The authors suggest that this distribution can be extracted from a high-SNR subset of the data to be analysed. This method looks promising, but an application to real survey data has not been performed yet.

To conclude, an important advantage of moment-based methods is that they do not assume particular knowledge about the data that need to be analysed, making them a preferable choice, compared to model-fitting approaches, in those situations where priors are not obvious.

3.2 From shape measurements to flexion

In section 2.2.6, we explained how flexion is related to the third derivatives of the lensing potential and show that it is responsible for the skewed and arclike appearance of lensed galaxies. In particular, we identified two combinations of the third derivatives of the lensing potential, that we called $\mathcal{F} - flexion$ and $\mathcal{G} - flexion$, which, respectively, measure the local variation of the convergence, $\mathcal{F} = \partial \kappa$, and of the shear, $\mathcal{G} = \partial \gamma$.

In order to be able to exploit the information carried by the flexion fields, we need to find some observable quantities that can be eventually related to them. Following the approach of moment-based methods, we can construct these estimators from combinations of the SB moments, in complete analogy to what was done for the shear field and discussed in section 2.2.7.

The first requirement we will impose is that the estimators we construct have the same spin properties as the fields we want to measure. Therefore, we need to find combinations of the SB moments with spin-1, for the $\mathcal{F} - flexion$ estimator, and spin-3, for the $\mathcal{G} - flexion$ estimator.

As proposed by Okura et al. (2007), two good candidates are represented

by the following combinations of third order moments:

$$\hat{\zeta} = \hat{\zeta}_1 + i\hat{\zeta}_2 \equiv (Q_{30} + Q_{12}) + i(Q_{21} + Q_{03}) \,,$$
$$\hat{\delta} = \hat{\delta}_1 + i\hat{\delta}_2 \equiv (Q_{30} - 3Q_{12}) + i(3Q_{21} - Q_{03}) \,, \tag{3.1}$$

which have the requested rotational symmetry properties. However, since flexion has the dimension of L^{-1}, we need to normalize $\hat{\zeta}$ and $\hat{\delta}$ with a combination of moments having spin-0 and dimension L^4. This can be done using the normalization factor:

$$\xi \equiv Q_{40} + 2Q_{22} + Q_{04} \,, \tag{3.2}$$

which is a combination of fourth order moments.

Hence, the two flexion estimators will be given by:

$$\zeta \equiv \frac{\hat{\zeta}}{\xi} = \frac{(Q_{30} + Q_{12}) + i(Q_{21} + Q_{03})}{\xi} \,,$$
$$\delta \equiv \frac{\hat{\delta}}{\xi} = \frac{(Q_{30} - 3Q_{12}) + i(3Q_{21} - Q_{03})}{\xi} \,. \tag{3.3}$$

The next step, in order to relate these quantities to the flexion fields, is to find how they transform under lensing. For this purpose we refer to the work of Viola et al. (2012), who derived the transformation of ζ and δ under lensing transformation, keeping all terms of first order in shear, flexion and the product of shear and flexion, differently from previous works.

The calculations that Viola et al. (2012) performed rely on two steps. First, the transformation of the 3rd and 4th order moments under lensing is computed neglecting the centroid shift induced by flexion and using the Jacobian obtained from the lens equation at second order (equation 2.35). Then, a correction for the centroid shift is applied. The result of these lengthy calculations are represented by the following transformation laws, between the pre-lensing spin-1 and spin-3 quantities, ζ^s and δ^s, and their observable counterparts, ζ and δ:

$$\zeta^{\rm s} \simeq \frac{1}{[1 - 4\Re(g^*\eta)](1-\kappa)} \Bigg[\zeta - 2g\zeta^* - g^*\delta - 2F^\star\eta$$
$$- \frac{9}{4}F - \frac{1}{2}G\eta^\star - \frac{1}{4}G^*\lambda + 3F^\star g + \frac{3}{2}Fg^\star\eta + \frac{3}{2}(F^\star g^\star\lambda)$$
$$+ \frac{1}{2}Gg\lambda^\star + \frac{7}{2}Fg\eta^\star + \mu\bigg(4F^\star\chi + \frac{1}{2}Fg^\star\chi + gG^\star\chi + 3F$$
$$+ Gg^\star - 4F^\star g - \frac{9}{2}gF\chi^\star + \frac{1}{2}G\chi^\star - 3F\Re(g\chi^\star)\bigg)\Bigg] \,, \tag{3.4a}$$

$$\delta^{\mathrm{s}} \simeq \frac{1}{[1 - 4\Re(g^*\eta)](1 - \kappa)} \left[\delta - 3g\zeta - \frac{5}{2}F\eta - \frac{7}{4}F^*\lambda - \frac{3}{4}G \right.$$
$$+ 6Fg - \frac{1}{2}Fg^\star\lambda + 4F^\star g\eta + \frac{3}{2}Gg\eta^\star - \frac{1}{2}G^\star g\lambda - \frac{1}{2}Gg^\star\eta \qquad (3.4\text{b})$$
$$\left. + 3\mu\left(\frac{3}{2}F\chi + \frac{1}{2}Gg^\star\chi - \frac{1}{2}F^\star g\chi - 3Fg + \frac{1}{2}Gg\chi^\star\right)\right],$$

where F and G are the *reduced flexion* fields:

$$F \equiv \frac{\mathcal{F}}{1 - \kappa} , \qquad G \equiv \frac{\mathcal{G}}{1 - \kappa} , \qquad (3.5)$$

the following dimensionless spin-2 and spin-4 quantities have been introduced:

$$\eta \equiv \frac{1}{\xi} \frac{\int d^2\theta I(\theta)\theta^3\theta^\star}{\int d^2\theta I(\theta)} = \frac{(Q_{40} - Q_{04}) + 2i(Q_{31} + Q_{13})}{\xi} ,$$
$$\lambda \equiv \frac{1}{\xi} \frac{\int d^2\theta I(\theta)\theta^4}{\int d^2\theta I(\theta)} = \frac{(Q_{40} - 6Q_{22} + Q_{04}) + 4i(Q_{31} - Q_{13})}{\xi} , \qquad (3.6)$$

and μ is a spin-0 quantity defined as:

$$\mu \equiv \frac{Tr(\mathcal{Q})^2}{\xi} = \frac{(Q_{20} + Q_{02})^2}{\xi} . \qquad (3.7)$$

Note that μ encodes the steepness of the surface brightness profile of the source, since it is defined as the ratio of two spin-0 quantities both describing the size of the source; one, $Tr(\mathcal{Q})$, in terms of 2nd-order moments and the other, ξ, in terms of 4th-order moments. The smaller μ, the steeper the surface brightness profile is.

Equations 3.4 relate the intrinsic deformations (ζ^s, δ^s) with the lensing-induced ones (ζ, δ), via different combinations of the reduced lensing fields (g, F, G), involving SB moments up to the fourth order (all moments higher than fourth order have been dropped in the derivation, since considered practically immeasurable). These equations are conceptually equivalent to the much simpler equations 2.44 for the spin-2 distortions.

Analogously to what we did for the shear, the step that follows consists in averaging equations 3.4 over a population of galaxies belonging to a region on the sky where the lensing fields can be considered constant. This is done in order to average to zero the intrinsic distortion terms ζ^s and δ^s, whose values are unknown. While doing this, some approximations can be made to simplify the equations. In particular, Okura et al. (2008), assuming that η and

λ are small and thus negligible, and that the shear and convergence are small, obtained a linear relation between the flexion fields and the estimators ζ and δ:

$$F \sim \left\langle \frac{\zeta}{9/4 - 3\mu} \right\rangle \tag{3.8a}$$

$$G \sim \frac{4}{3}\langle\delta\rangle \tag{3.8b}$$

However, Viola et al. (2012) argued that the assumptions made by Okura et al. (2008) are too restrictive, especially for cluster lensing applications. In particular, they claimed that shear and convergence cannot be neglected at the scale where flexion is usually measured, [0.1-1] Mpc/h from the cluster center. Hence, terms of the form *shear* $\times$ *flexion*, contribute with important corrections and cannot be neglected, as done in previous works (Goldberg and Leonard, 2007; Okura et al., 2008; Leonard et al., 2011). Viola et al. (2012) showed how the linear relations 3.8 can lead to biases up to 85% and 150% for ζ and δ, respectively. This bias generally depends on the strength of the lensing fields, on the intrinsic ellipticity dispersion and on the concentration of the galaxies. They also provided more accurate formulae for the spin-1 and spin-2 distortion estimators, concluding, however, that ζ and δ cannot be related in a straightforward way to F and G flexion, in particular not for strongly elliptical galaxies or near the centers of galaxy clusters. In fact, terms coupling shear and flexion produce non-negligible spin-1 and spin-3 deformations, which contribute to those induced by flexion alone. Furthermore the flexion deformations depend on the morphology (ellipticity and concentration) of the source galaxy. Therefore, the equations proposed by Viola et al. (2012), do not provide direct flexion estimators, but they describe the average measured spin-1 and spin-3 distortions in terms of lensing fields and galaxy properties:

$$
\begin{aligned}
\langle\zeta\rangle \simeq & \left(\frac{9}{4} - 3\langle\mu\rangle - \frac{5}{4}\langle\mu|\chi|^2\rangle\right)F + \left(\frac{9}{4} - \frac{5}{4}\langle\mu|\chi|^2\rangle - \langle\mu\rangle\right)Gg^\star + \\
& + \left(\frac{15}{2} - 3\langle\mu|\chi|^2\rangle - 2\langle\mu\rangle\right)F^\star g - 4\langle\mu\chi\rangle F^\star - \frac{1}{2}\langle\mu\chi^\star\rangle G
\end{aligned}
\tag{3.9a}
$$

$$
\langle\delta\rangle \simeq \frac{3}{4}(1 - \langle\mu|\chi|^2\rangle)G + \left(\frac{33}{4} - \frac{3}{4}\langle\mu|\chi|^2\rangle\right)gF - \frac{9}{2}\langle\chi\mu\rangle F \tag{3.9b}
$$

Following the suggestion of the authors, in the rest of this thesis, we will refer to ζ and δ as *distortion estimators*, rather then flexion estimators.
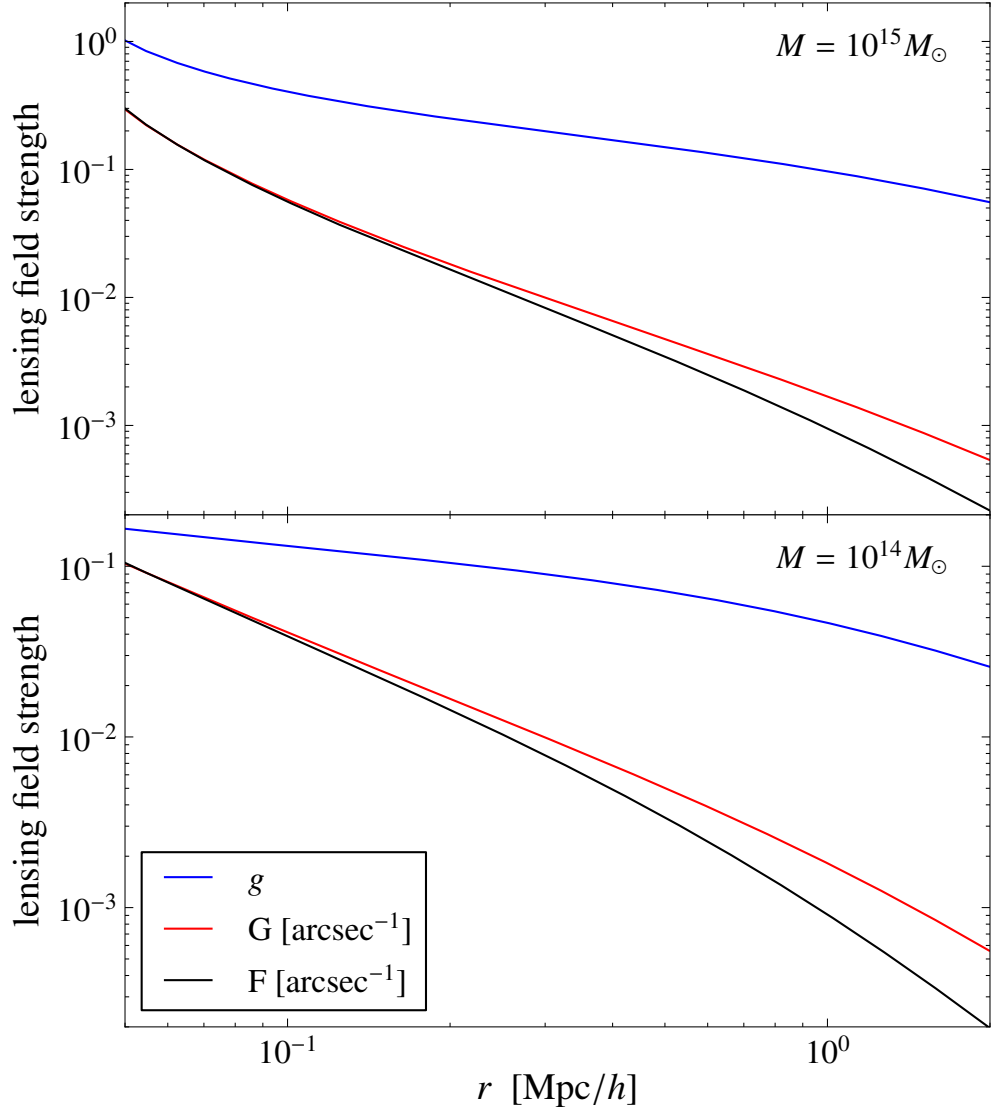
Figure 3.2: Profiles of reduced shear g and reduced flexions G and F (top to bottom lines) for a halo with analytic NFW profile, with mass $10^{15} M_\odot$ (top panel) and $10^{14} M_\odot$ (bottom panel) at redshift $z = 0.5$. Background galaxies are located at $z_s = 2$. These values represent a realistic case for cluster lensing studies. Figure taken from Viola et al. (2012)

Chapter 4

FLEXION WITH DEIMOS

As we discussed in the previous chapter, the first fundamental step in the process of measuring flexion (or shear) is the accurate recovery of the shape of the lensed galaxies. In particular, since the flexion fields induce deformations with spin-1 and spin-3, we need to estimate the amount of distortions, in a given lensed galaxy, which exhibit these rotational symmetry properties. A possible way to do this is through the estimators ζ and δ, introduced in section 3.2. However, since these estimators are combinations of third- and fourth-order SB moments, their measurement is very challenging in practical applications. In fact, the impact of the noise becomes more important when we move to the outer regions of the galaxies, making the measurements of the high-order moments of SB very complicated. The work presented in this thesis deals with this precise issue, the measurement of spin-1 and spin-3 distortions in weakly lensed background galaxies. In particular, we try to answer the question: are ζ and δ measurable in the typical observational conditions of weak lensing surveys?

In this chapter we present the first method we have applied to measure these estimators, which is based on a modified version of the DEIMOS algorithm for weak-lensing measurements (Melchior et al., 2011). First, we will introduce the standard version of the algorithm as presented in the original paper Melchior et al. (2011); we will, then, describe how the method can be extended in order to determine flexion-induced distortions and test its performance in the measurement of such kind of distortions.

Notation

We introduce in this chapter a slight change of notation, to follow the notation used by Melchior et al. (2011). Given the brightness distribution $I(\boldsymbol{x})$, we will

denote the moment of surface brightness of order $n = i + j$ as:

$$\{I\}_{i,j} \equiv \int d^2x I(\boldsymbol{x}) x_1^i x_2^j \; , \tag{4.1}$$

replacing the old notation Q_{ij}.

4.1 The DEIMOS algorithm

The DEIMOS (DEconvolution In MOment Space) algorithm for weak lensing measurements is a model-independent approach which has been proposed by Melchior et al. (2011) as en extension to the KSB method in order to overcome the main shortcomings of that method. In particular DEIMOS, differently from KSB, does not rely on any assumption about the shape of the PSF. The main innovation of DEIMOS is thus the deconvolution algorithm. DEIMOS applies an exact deconvolution, which requires only the knowledge of the PSF moments of the same order as the galaxy moments to be corrected. This is allowed since it is possible to derive an analytic relation between the convolved and unconvolved moments. To derive this relation Melchior et al. (2011) used the fact that any square-integrable one-dimensional function $G(x)$ has an exact representation in Fourier space:

$$G(x) \quad \rightarrow \quad \phi_G(k) = \int dx \; G(x) \; e^{ikx} \; . \tag{4.2}$$

In statistics, ϕ_G is usually called the *characteristic function* of G and can as well be expressed in the following form:

$$\phi_G(k) = \sum_n^{\infty} \{G\}_n \frac{(ik)^n}{n!} \; , \tag{4.3}$$

obtaining in this way a relation between the Fourier transform of the function G and its moments $\{G\}_n$ (given by the one-dimensional version of equation 4.1). Now, if we imagine to convolve the function G with a kernel P, using the convolution theorem, we can express the convolution of these two functions as a product in Fourier space:

$$G^\star(x) \equiv \int dx' \; G(x) \; P(x - x') \quad \rightarrow \quad \phi_{G^\star} = \phi_G \cdot \phi_P \; . \tag{4.4}$$

If we assume, for convenience, the kernel P to be normalized, $P_0 = 1$, using equation 4.3, we can rewrite the Fourier transform of the convolved function in the following way:

$$\phi_{G^\star}(k) = \Big[\sum_n^\infty \{G\}_n \frac{(\mathrm{i}k)^n}{n!}\Big]\Big[\sum_n^\infty \{P\}_n \frac{(\mathrm{i}k)^n}{n!}\Big] =$$

$$= \sum_n^\infty \sum_m^n \{G\}_m \frac{(\mathrm{i}k)^m}{m!} \{P\}_{n-m} \frac{(\mathrm{i}k)^{n-m}}{(n-m)!} = \tag{4.5}$$

$$= \sum_n^\infty \Big[\sum_m^n \binom{n}{m}\{G\}_m\{P\}_{n-m}\Big]\frac{(\mathrm{i}k)^n}{n!} \,,$$

where we have used the Cauchy product. By definition, the term in square brackets represents the moment of order n of the convolved function $G^\star$:

$$\{G^\star\}_n = \sum_m^n \binom{n}{m}\{G\}_m\{P\}_{n-m}. \tag{4.6}$$

Therefore, the convolution of the function G with the kernel P can now be expressed entirely in moment space. Note, that even though the series in equation 4.3 is infinite, the nth-order moment of $G^\star$ is obtained from a finite sum of n terms given by the products of moments of G and P up to order n. This result is valid for any shape of G and P, as long as their moments do not diverge.

It is possible to generalize this result to the case of two-dimensional functions. Given a surface brightness distribution $G(\boldsymbol{x})$ and a PSF kernel $P(\boldsymbol{x})$, the moments of the convolved function will be given by:

$$\{G^\star\}_{i,j} = \sum_k^i \sum_l^j \binom{i}{k}\binom{j}{l}\{G\}_{k,l}\{P\}_{i-k,j-l} \,, \tag{4.7}$$

as also shown by Flusser and Suk (1998).

In astronomical applications, what we need is the inverse relation, in fact, we want to obtain the unconvolved moments starting from the measured convolved ones. An important feature of equation 4.7 makes this task possible. The convolved moment of order $n = i + j$ is, in fact, only a function of unconvolved moments of lower order and PSF moments of at most the same order. Hence, starting from the zeroth order convolved moment, which has to be corrected only if the PSF is not flux-normalized, we obtain the unconvolved zeroth order moment that we can use, together with the first moments of the PSF, to correct the first order moments of the galaxy, and so on. For convenience, we report in table 4.1 the set of equations which need to be solved to obtain the deconvolved moments up to second order. This hierarchical build-up of the deconvolved moments is the heart of the DEIMOS method.

Table 4.1: Equations for the deconvolution of the moments up to order $n = 2$. These formulae are specializations of the equation 4.7.

$\{G\}_{0,0} \{P\}_{0,0} = \{G^\star\}_{0,0}$

$\{G\}_{0,1} \{P\}_{0,0} = \{G^\star\}_{0,1} - \{G\}_{0,0} \{P\}_{0,1}$

$\{G\}_{1,0} \{P\}_{0,0} = \{G^\star\}_{1,0} - \{G\}_{0,0} \{P\}_{1,0}$

$\{G\}_{0,2} \{P\}_{0,0} = \{G^\star\}_{0,2} - \{G\}_{0,0} \{P\}_{0,2} - 2\{G\}_{0,1} \{P\}_{0,1}$

$\{G\}_{1,1} \{P\}_{0,0} = \{G^\star\}_{1,1} - \{G\}_{0,0} \{P\}_{1,1} - \{G\}_{0,1} \{P\}_{1,0} - \{G\}_{1,0} \{P\}_{0,1}$

$\{G\}_{2,0} \{P\}_{0,0} = \{G^\star\}_{2,0} - \{G\}_{0,0} \{P\}_{2,0} - 2\{G\}_{1,0} \{P\}_{1,0}$

Noise and weighting

In real applications however an extra complication in the measurements of SB moments has to be faced. It arises from the inevitable presence of noise in the images. In fact, what we measure in practice is not the surface brightness $G(\boldsymbol{x})$ of the galaxy, rather the function:

$$I(\boldsymbol{x}) = G(\boldsymbol{x}) + N(\boldsymbol{x}) , \qquad (4.8)$$

where the noise N can considered to be independently drawn from a Gaussian distribution with certain variance σ_n^2, that means $\langle N(\boldsymbol{x}_i)N(\boldsymbol{x}_j)\rangle = \sigma_n^2 \delta_{ij}$ for any two positions $\boldsymbol{x}_i$ and $\boldsymbol{x}_j$. It follows from the definition of moments itself (equation 4.1) that, when measuring the SB moments of a certain galaxy, the largest contribution is given, for $n > 0$, by the values of SB at large distances from the galactic center. Unfortunately, for finite and compact brightness distribution G, these values are dominated by the noise. For this reason, it is necessary to introduce a weight function W of finite width that is centered on the galaxy and allows to limit the integration range for the SB moments measurement to regions in which G dominates. Basically, what we will actually measure are the moments of the following function:

$$I_w(\boldsymbol{x}) \equiv W(\boldsymbol{x})I(\boldsymbol{x}) . \qquad (4.9)$$

The particular choice for the shape of the weight function (WF, hereafter) differs from method to method. DEIMOS, following the idea of Bernstein and Jarvis (2002), uses a WF given by an elliptical Gaussian whose parameters (centroid $\mathbf{x}_c$, size s and ellipticity (ϵ_1, ϵ_2)) are matched to the shape of the source[1] to be measured:

---

[1]The matching procedure iteratively determines centroid, size, and ellipticity of the WF such as to maximize the measured signal-to-noise ratio.

$$W(\boldsymbol{x}) \equiv \exp\left(-\frac{\boldsymbol{x'}^2}{2s^2}\right) , \qquad (4.10)$$

with:

$$\boldsymbol{x'} = \begin{pmatrix} 1 - \epsilon_1 & -\epsilon_2 \\ -\epsilon_2 & 1 + \epsilon_1 \end{pmatrix} (\boldsymbol{x} - \boldsymbol{x}_c) . \qquad (4.11)$$

Unfortunately, the weighting procedure influences the outcome. We, thus, need to find a way to correct the change induced by the WF on the moments. The solution proposed in DEIMOS is to approximate the moments of I by using their *deweighted* counterparts $\{I^{dw}\}_{i,j}$, which, as we will now explain, are obtained as linear combinations of weighted moments of higher order. Basically, if we invert equation 4.9, by writing $I = I_w W^{-1}$, and then expand W^{-1} in a Taylor series around the center $\boldsymbol{x} = \boldsymbol{0}$ and truncate the expansion at order n_w (which represents a parameter of the method), we can write:

$$\{I\}_{i,j} = \int d^2x \ I(\boldsymbol{x}) \ x_1^i x_2^j \simeq \int d^2x \ I_w(\boldsymbol{x}) W_{tay}^{-1}(\boldsymbol{x}) \ x_1^i x_2^j \equiv \{I^{dw}\}_{i,j} , \quad (4.12)$$

Now, being W_{tay}^{-1} a polynomial function of the variables x_1 and x_2 with terms up to degree n_w, if we insert its actual polynomial expression in equation 4.12, it appears clear that we can re-express the last integral as the sum of specific moments of I_w multiplied by certain coefficients (given by the polynomial coefficients). In this way, we are now able to write the deweighted moment of order n, $\{I^{dw}\}_n$, as a linear combination of weighted moments $\{I_w\}$ up to order $n + n_w$, as we reported in table 4.2 for the different cases: $n_w = 0, 2, 4, 6$.

Summarizing, when measuring in real applications the shape of distant galaxies from their SB moments, we encounter the following complications: the presence of noise degrades the images and requires the employment of a WF, the weighting procedure introduces a bias in the measured moments, finally, the convolution with the PSF kernel changes the observed shape of galaxies. The recipe proposed by DEIMOS to deal with these problems can be synthesized in the following three steps:

- *Weigthing:* a WF is applied to the galaxy in order to control the effect of noise. The center, size and ellipticity of the WF are matched to the source, according to an iterative process which, by varying the centroid position and ellipticity of the WF at a fixed scale, looks for those values

Table 4.2: Correction terms for deweighting moments of order $n = i + j$. The deweighted moments $\{I_{dw}\}_{i,j}$ are given by the sum of the correction terms up to the limiting order n_w.

n_w	correction terms
0	$\{I_w\}_{i,j}$
2	$\frac{1}{2s^2}\left[c_1\{I_w\}_{i+2,j} - 4\,\epsilon_2\{I_w\}_{i+1,j+1} + c_2\{I_w\}_{i.j+2}\right]$
4	$\frac{1}{8s^4}\left[c_1^2\{I_w\}_{i+4,j} - 8\,c_1\epsilon_2\{I_w\}_{i+3,j+1} + \left[2\,c_1c_2 + 16\,\epsilon_2^2\right], \{I_w\}_{i+2,j+2} - \right.$ $\left. 8\,c_2\epsilon_2\{I_w\}_{i+1,j+3} + c_2^2\{I_w\}_{i,j+4}\right]$
6	$\frac{1}{48s^6}\left[c_1^3\{I_w\}_{i+6,j} - 12\,c_1^2\epsilon_2\{I_w\}_{i+5,j+1} + \left[3\,c_1^2c_2 + 48\,c_1\epsilon_2^2\right]\{I_w\}_{i+4,j+2} - \right.$ $\left[24\,c_1c_2\epsilon_2 + 64\,\epsilon_2^3\right]\{I_w\}_{i+3,j+3} + \left[3\,c_1c_2^2 + 48\,c_2\epsilon_2^2\right]\{I_w\}_{i+2,j+4} - $ $\left. 12\,c_2^2\epsilon_2\{I_w\}_{i+1,j+5} + c_2^3\{I_w\}_{i,j+6}\right]$

that maximize the signal-to-noise ratio. The procedure is then repeated for different initial scales. When the matching converges, the weighted moments $\{I_w\}$ are calculated.

- *Deweighting:* in this step the change induced on the moments by the weighting process is corrected. The real moments are approximated by specific combinations of higher order weighted moments (see table 4.2).

- *Deconvolution:* in the last step DEIMOS corrects for the effect of PSF convolution. Once the moments of the PSF have been evaluated (from the images of stars), the deweighted moments obtained in the previous step are corrected according to the deconvolution equations given in table 4.1.

4.1.1 Performance on shear measurements

The ability of DEIMOS to measure shear has been tested by Melchior et al. (2011) making use of the simulations with realistic noise level provided by the GREAT08 challenge (Bridle et al., 2010). We report in this section the main result of this study. In order to understand this result, it is necessary to introduce some quantities, which have been used by the authors to show how their method is highly competitive. In particular, the DEIMOS performance has been described in terms of the following quality factors:

- The GREAT08 quality metric Q, defined as:

$$Q = \frac{10^{-4}}{\langle(\langle g_{ij}^m - g_{ij}^t \rangle_{j \in k})^2\rangle_{ikl}} \ , \tag{4.13}$$

where g_{ij}^m is the ith component of the measured shear for simulation j, g_{ij}^t is the corresponding true shear component; the inner angle brackets denote an average over sets representing different realizations with same shear value and observing conditions $j \in k$, and the outer angle brackets denote an average over simulations with different true shears k, observing conditions l and shear components i.

- The analogous metric Q_l for a single simulation branch:

$$Q_l = \frac{10^{-4}}{\langle(\langle g_{ij}^m - g_{ij}^t \rangle_{j \in k})^2\rangle_{ik}} \ , \tag{4.14}$$

where the average over different observing conditions l is omitted.

- The multiplicative shear accuracy parameters m_i, obtained from a linear fit of the shear estimate $\tilde{g}_i$ to the true shear values g_i, as defined in the shear testing program STEP (Heymans et al., 2006; Massey et al., 2007a):

$$\tilde{g}_i - g_i = m_i g_i + c_i \ . \tag{4.15}$$

The results obtained with DEIMOS are shown in figure 4.1 for the different branches of RealNoise_Blind simulations from the GREAT08 challenge (Bridle et al., 2009, 2010). These simulations are, in fact, divided into 9 different branches, which differ from each other by the values/characteristics of the following parameters: signal-to-noise ratio, galaxy size, galaxy model and PSF model. For the fiducial branch the value of these parameters is indicated by the central point in each panel. The other 8 branches, instead, are obtained by varying one of the four parameters/features (to the value indicated on the right or on the left), while keeping the other three equal to the fiducial value. The DEIMOS algorithm was run on the different branches by keeping the scale s of the WF and the correction order n_w fixed to the values inferred by optimizing the outcome for a set of simulations with known shears ($s = 4$, $nw = 4$). In figure 4.1, we can see that DEIMOS performs well in most of the branches, yielding $Q > 200$ in seven out of nine branches, with a particularly high value of Q for the single-component galaxy models (branch labeled "b or d"). The two cases in which DEIMOS does not perform well correspond to the "low S/N" branch and the "small galaxy size" branch. Nevertheless, an improvement for both branches was obtained by adjusting the values of s and n_w to the source characteristics of the specific branch (specifically, shrinking the WF

to $s = 2.5$). Similarly, the performance on the high S/N branch improves when a higher deweighting order $n_w = 6$ is assumed. The improvement obtained in these three branches is highlighted in figure 4.1 by the points connected by dashed lines, which correspond to the values found before adapting s and n_w to the characteristics of the specific branch.

4.2   Simulating galaxy images to test DEIMOS

Before presenting the tests that we performed with DEIMOS in order to investigate the ability to measure flexion, we will describe in this section the tools that we used for this investigation. Indeed, all the tests that are presented in this chapter and the following ones were performed making use of different sets of mock images of weakly lensed galaxies. The images were produced with the *shapelens* library[2], inside which the DEIMOS algorithm has been developed. Each galaxy postage stamp was generated on its own grid of $L \times L$ pixels, according to the following scheme:

1. A PSF model is assumed. In particular, unless differently specified, we assume the PSF to follow a Moffat profile (Moffat, 1969), which is defined as:

$$P_{mof}(R) \propto (\ 1 + \alpha R^2\ )^{-\beta}\ , \tag{4.16}$$

   where $R = \sqrt{x_1^2 + x_2^2}$ represents the position on the image plane; the parameter α sets the width of the profile and is related to the full width at half maximum[3] (FWHM, hereafter) by the following relation: $\alpha = (2^{1/\beta} - 1)/(\text{FWHM}/2)^2$. Finally, the slope of the profile is set by β. Note that as β increases the Moffat function tends to approximate a Gaussian profile, which in fact represents a limiting case for the Moffat profile for $\beta \to \infty$ (Trujillo et al., 2001).

2. A galaxy model is assumed and simultaneously modified through a coordinate transformation which represents a particular lensing transformation. In all our simulations the galaxies are modeled with a Sérsic profile (Sérsic, 1963):

$$I(R) \propto \exp\left\{ -b_n \left[\left(\frac{R}{R_e} \right)^{1/n_s} - 1 \right] \right\}\ , \tag{4.17}$$

---

[2]https://github.com/pmelchior/shapelens

[3]The FWHM of a given function is defined such that at $R = \text{FWHM}/2$ the function drops to half of its central value.
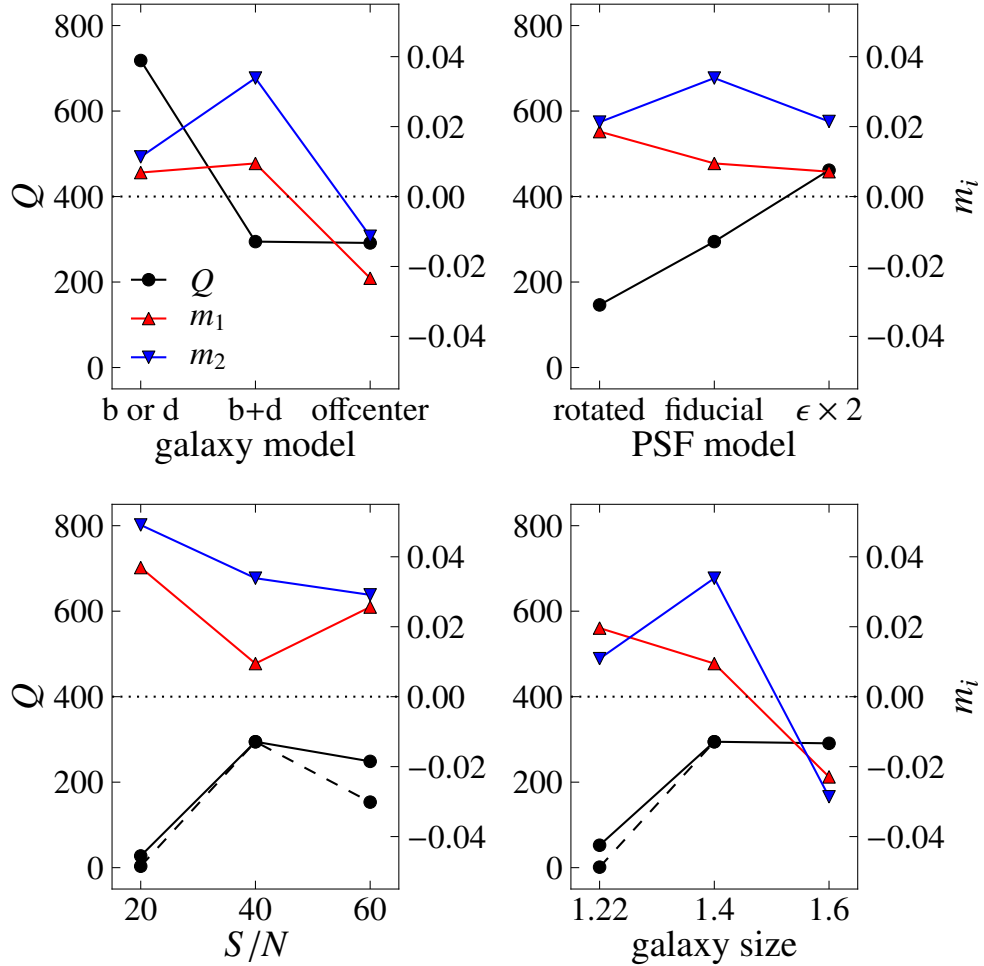
Figure 4.1: DEIMOS shear accuracy tests: GREAT08 Q metric and multiplicative shear errors m_i for the nine different branches of the GREAT08 challenge RealNoise_Blind simulations (we refer to Bridle et al. (2010) for a detailed description of the different branches). In each panel, the scale on the left describes the values of Q and the scale on the right the values of m_i. The points connected by dashed lines denote the values obtained before re-running DEIMOS with values of s and n_w adjusted to the source characteristics. Figure taken from Melchior et al. (2011)

which is characterized by two parameters: R_e and n_s. The effective radius R_e is defined as the radius that encloses half of the total light from the model. The Sérsic index n_s denotes, instead, the slope of the profile. Profiles with $n_s = 1$ are good approximations for disk galaxies, while profiles with $n_s = 4$ represent elliptical galaxies, finally $n_s = 0.5$ corresponds to a Gaussian profile. The constant b_n is defined in terms of the Sérsic index, by the following relation between the complete and the incomplete gamma functions: $\Gamma(2n_s) = 2\gamma(2n_s, b_n)$, which for $0.5 < n_s < 10$ approximately yields: $b_n \approx 1.9992n_s - 0.3271$ (Capaccioli, 1989; Prugniel and Simien, 1997). The profile given in equation 4.17 is then reshaped by adding an intrinsic ellipticity ϵ_{int} and applying a lensing transformation with specified values of the lensing fields: κ, γ, $\mathcal{G}$, $\mathcal{F}$.

3. The light of both the PSF and the galaxy profiles is binned into a grid of $L \times L$ pixels, in the format of a FITS image.

4. The galaxy image is convolved with the PSF image.

5. Finally, Gaussian noise is added to the convolved image. In particular, each pixel value is modified by adding a random number drawn from a Gaussian distribution with mean $\mu_n = 0$ and standard deviation σ_n.

The mock images that we obtain at the end of this procedure incorporate all the processes that in real applications degrade the quality of our data. They represent then an ideal candidate to test the ability of a certain algorithm to recover the shape of noisy images of weak lensed galaxies. The idea is the following: we will compare the distortion estimators, constructed with the SB moments measured with our algorithm on the final mock image (as obtained after step 5), to the estimators constructed with the SB moments measured on the image at step 3, i.e. before applying PSF convolution and noise degradation. In this way we can test how the method performs in different situations, for example, by changing the intrinsic characteristics of the galaxy population, the lensing regimes or the observing conditions. A first example of this kind of tests is given in the next section.

4.3   Preparatory tests

We present here some preliminary tests we made with DEIMOS, following the procedure described in the previous section. These tests concern the measurement of ellipticity and shear in absence of flexion.

The first test was run on a sample of 10000 mock images of Sérsic galaxies with $n_s = 1$ and $R_e = 3$ pixels. The galaxies have intrinsic ellipticities

randomly drawn from a Rayleigh distribution with $\sigma_\epsilon = 0.3$. We did not apply any lensing transformation in this case. The PSF is of Moffat-type with $\epsilon = (0.05, 0.05)$, $\beta = 3$, FWHM = 3 pixels. The flux of the galaxies is fixed at unity, and the images are degraded by Gaussian pixel noise with null mean and dispersion $\sigma_n = 10^{-3} \times flux$, which translates into a signal-to-noise ratio: SNR ~ 50, as measured by SExtractor[4], connoting particularly favorable observational conditions[5]. The image of one of these galaxies is shown in figure 4.2, both before and after PSF convolution and noise degradation are applied (left and right panel, respectively). In figure 4.3, we report the comparison between the first component of the ellipticity measured by DEIMOS on the noisy convolved images, ϵ^{dei}, and the true ellipticity, ϵ^{true}, represented by the ellipticity measured with a flat WF on the noise-free pre-convolution images. The correction order used for the deweighting is $n_w = 4$ and we let DEIMOS find, for each galaxy, the optimal WF scale among a set of scales $s \in [2, 7]$ pixels.

As we can see in figure 4.3, there are some galaxies for which the ellipticity measured with DEIMOS differs quite strongly (more than 50%) from the true one. This is, unfortunately, an inevitable problem, shared by all shape measurement methods, due to the noise interference. Nevertheless, we have to consider that in order to measure the shear it is essential to average over the ellipticities of many galaxies, since the shear is approximated by the mean ellipticity of a population of galaxies assumed to undergo the same lensing transformation. Hence, as long as the estimate of the mean ellipticity of a group of galaxies subject to the same lensing distortions is accurate, the presence of some outliers with offset measured ellipticity does not represent a worrisome factor. In this regard, we present in figure 4.4 the results of a second test, concerning shear inference. The figure shows the errors committed by DEIMOS on the estimate of the reduced shear g as a function of the shear strength, for a population of 500 galaxies subject to the same lensing fields. For the galaxy and PSF modelling we assumed the same parameters described in the previous paragraph, besides we lensed the galaxies with constant values of the lensing fields (κ, γ_1, γ_2). We repeated this operation for 7 different values of γ_1, and for each of these shear values we run two different simulations, increasing, in the second simulation, the root mean square (rms) of the Gaussian pixel noise from the

---

[4]SExtractor (Source-Extractor), developed by Bertin and Arnouts (1996), is a program widely use in astronomy that builds a catalog of all sources in a given astronomical image and provides for each object many useful parameters describing its astrometry and photometry in a fast way. It is mostly used as first pass over the data, in order to select objects for further study. [http://www.astromatic.net/software/sextractor]

[5]In current weak lensing surveys, galaxies with SNR ~ 50 belong to the high-value tail of the SNR distribution (Chang et al., 2013; Mandelbaum et al., 2015).
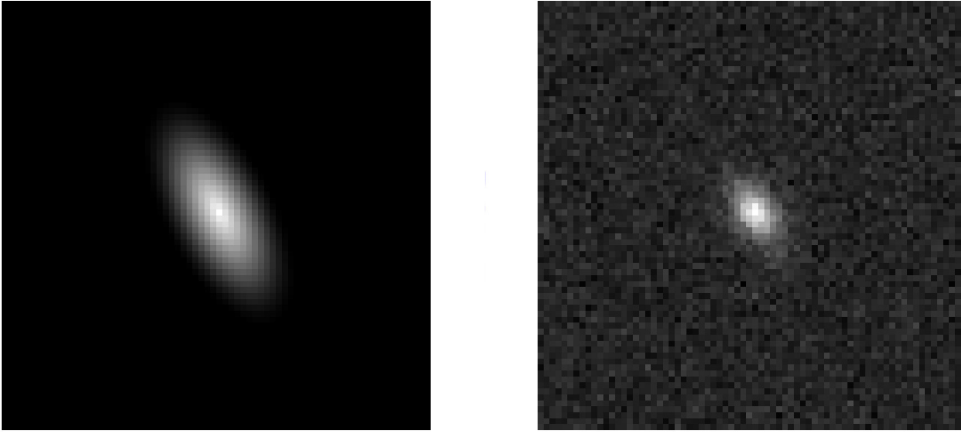
Figure 4.2: Example of simulated galaxy images. *Left panel:* Image of an elliptical Sérsic galaxy, before convolution with the PSF and noise addition; the SB moments measured on this image with a flat WF are used to construct the true ellipticity ϵ^{true}. *Right panel:* Image of the same galaxy after convolution with the PSF and degradation due to Gaussian pixel noise; this is the image that is given as input to DEIMOS to measure the SB moments and with them construct its estimate ϵ^{dei} of the true ellipticity. The left image is plotted in logarithmic scale colormap, while the right one in linear scale colormap.
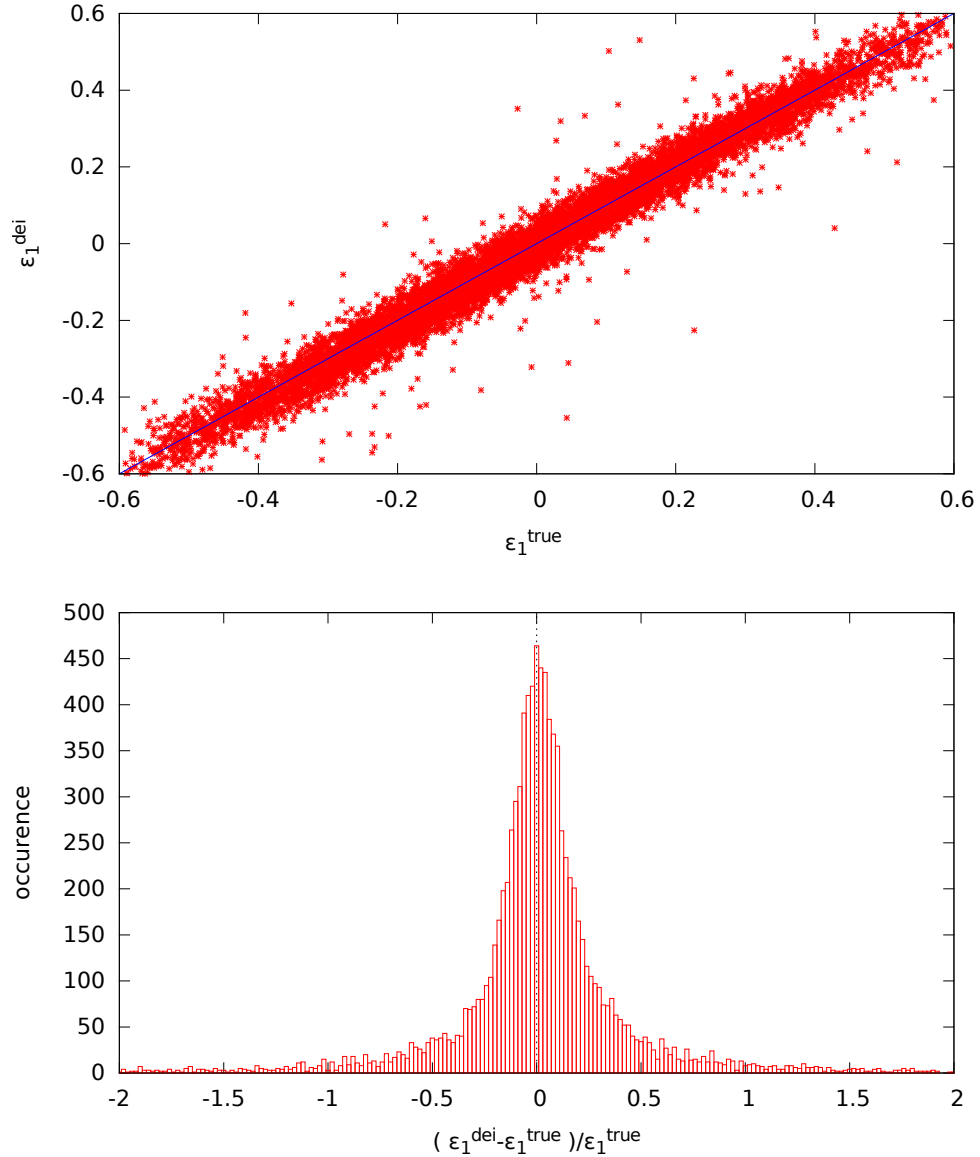
Figure 4.3: Deimos ellipticity measurements for a population of 10000 Sérsic galaxies with $n_s = 1$, $R_e = 3$ pixels and intrinsic ellipticities sampled from a Rayleigh distribution with $\sigma_\epsilon = 0.3$. The galaxies are convolved with a Moffat PSF with $\beta = 3$ and FWHM= 3 pixels, and degraded with Gaussian pixel noise with standard deviation $\sigma_n = 10^{-3}$ for flux-normalized sources. *Upper panel:* First component of the ellipticity as measured by DEIMOS vs first component of the true ellipticity (as estimated from the noise free unconvolved image). *Lower panel:* Distribution of the relative residuals. For both panels, the situation is analogous for the second component of the ellipticity.
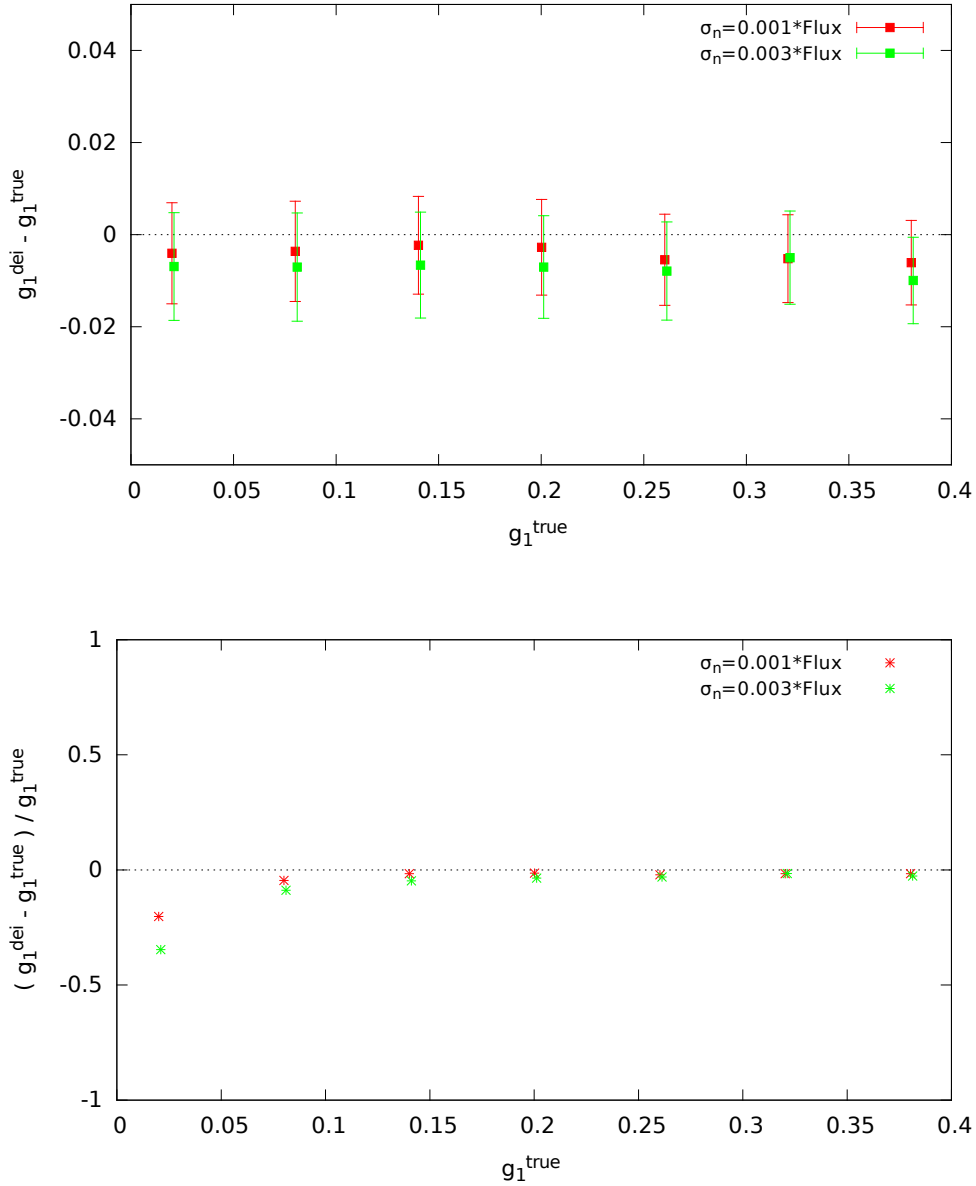
Figure 4.4: Deimos shear estimate, $g_1^{dei} \equiv \langle \epsilon_1^{dei} \rangle$, as a function of the applied shear, $g_1^{true} = \gamma_1/(1-\kappa)$, for a population of 500 noisy and convolved Sérsic-type galaxy images. The total flux of the sources was fixed to unity. Two different noise level were considered: *red points* correspond to images with noise rms $\sigma_n = 10^{-3}$, while *green points* to images with $\sigma_n = 3 \cdot 10^{-3}$. Errorbars denote standard deviation of the mean.

fiducial value $\sigma_n = 0.001$ in units of flux to $\sigma_n = 0.003$.

4.4   Flexion measurements with DEIMOS

After having shown how the standard version of DEIMOS performs on ellipticity measurements, we can now focus on the measurement of spin-1 and spin-3 distortions.

   To test the ability of DEIMOS to measure this kind of distortions, we need, first of all, to produce mock images of flexed galaxies. To this purpose we proceeded as described in section 4.2, setting, this time, non-zero values for the flexion fields $\mathcal{F}$ and $\mathcal{G}$.

Test 1: Standard DEIMOS on sheared and flexed galaxies

One of the advantages of the DEIMOS algorithm is that it can be easily extended to the measurement of higher order distortions, by simply increasing the order of SB moments to be measured. In this regard, we performed a first test which consisted in applying the standard version of the DEIMOS algorithm (i.e. elliptical WF matched to the source shape) to a sample of flexed and sheared galaxy images. In particular, we estimated the shape of 5000 galaxies, characterized by different intrinsic ellipticities, but subject to the same lensing transformation, by making use of the distortion estimators ϵ, χ, δ, ζ.

   In figure 4.5 we show three examples of the mock images we used for our test. The galaxies are Sérsic-type galaxies with $R_e = 3$ pixels and $n_s = 1$, they have flux fixed to unity and random intrinsic ellipticity drawn from a Rayleigh distribution with $\sigma_\epsilon = 0.3$. They are convolved with a Moffat PSF with $\beta = 3$, FWHM= 3 pixels and $\epsilon_{PSF} = (0.05, 0.05)$, and degraded with Gaussian pixel noise with null mean and rms $\sigma_n = 0.001$ in flux units. The values of the fields used for the lensing transformation are obtained from a realistic lensing situation, in particular we assumed: $\kappa = 0.1$, $\gamma = (0.09, 0)$, $\mathcal{F} = (0.0072, 0)$, $\mathcal{G} = (0.009, 0)$, which correspond to typical values for a NFW cluster of $10^{14} M_\odot$ at distance $r \sim 200 - 300$ kpc$/h$ from the cluster center (see figure 3.2).

   The result we obtained for the estimate of ϵ, δ, and ζ are presented in figures 4.7 and 4.6. From these plots it appears immediately clear that using an elliptical WF to measure the shape of flexed galaxies is not a suitable choice, this being true regardless of the parameters s and n_w used. In fact, as we can see in figures 4.6 and 4.7, the values of the spin-1 and spin-3 distortion estimators, ζ_1 and δ_1, obtained with DEIMOS do not reproduce at all the corresponding real values, being almost uniformly distributed in a large interval
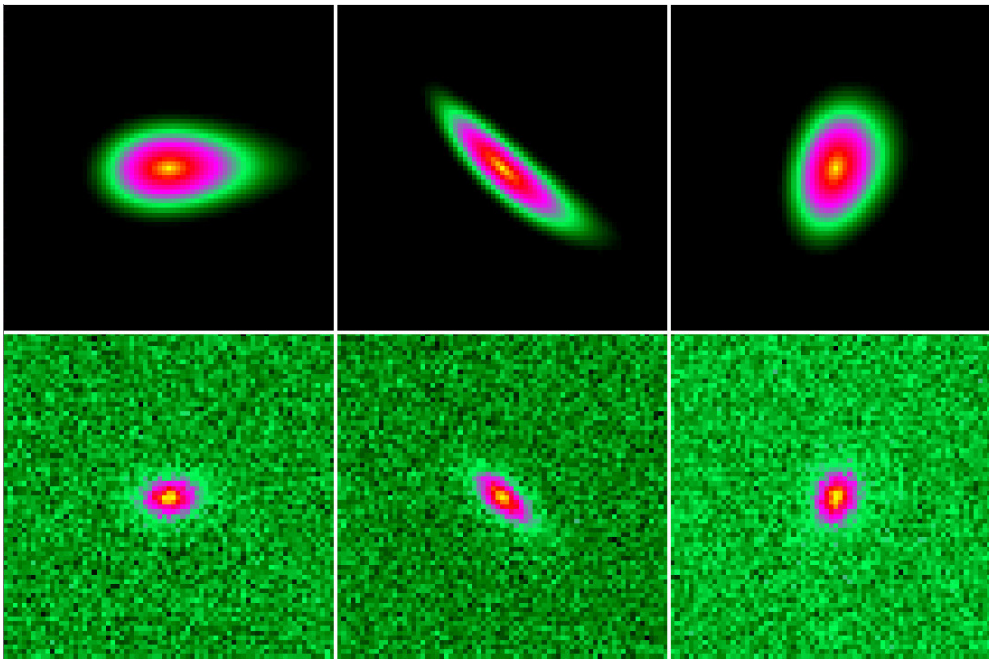
Figure 4.5: Examples of mock images of flexed galaxies. The galaxies are intrinsically elliptical and are lensed with non-zero values of both shear and F and G flexion. *Upper panels*: galaxies as appear before convolution and noise degradation; images are plotted in logarithmic scale colormap. *Lower panels*: final images used for shape measurements (pixel noise has rms $\sigma_n = 0.001 \times flux$); in this case images are plotted in linear scale colormap.

of values around the true one. On the other side, it is important to note that the ellipticity measurements continue to be reliable, even if the galaxies are now characterized by this more complex "banana shape".

Test 2: DEIMOS with (known) flexed WF

As we explained in section 4.1, the idea behind DEIMOS measurements of ellipticity is to use a Gaussian WF, whose scale, centroid and ellipticity are matched to the ones of the source, through an iterative process based on the maximization of the signal-to-noise ratio. It is, then, natural to expect that to measure the higher order distortions induced by flexion, the use of a WF with flexed shape becomes necessary. Especially, if we consider that in the case of flexion the noise impact is more severe than for the shear, since the estimators for the spin-1 and spin-3 distortions are built from the 3rd and 4th order SB
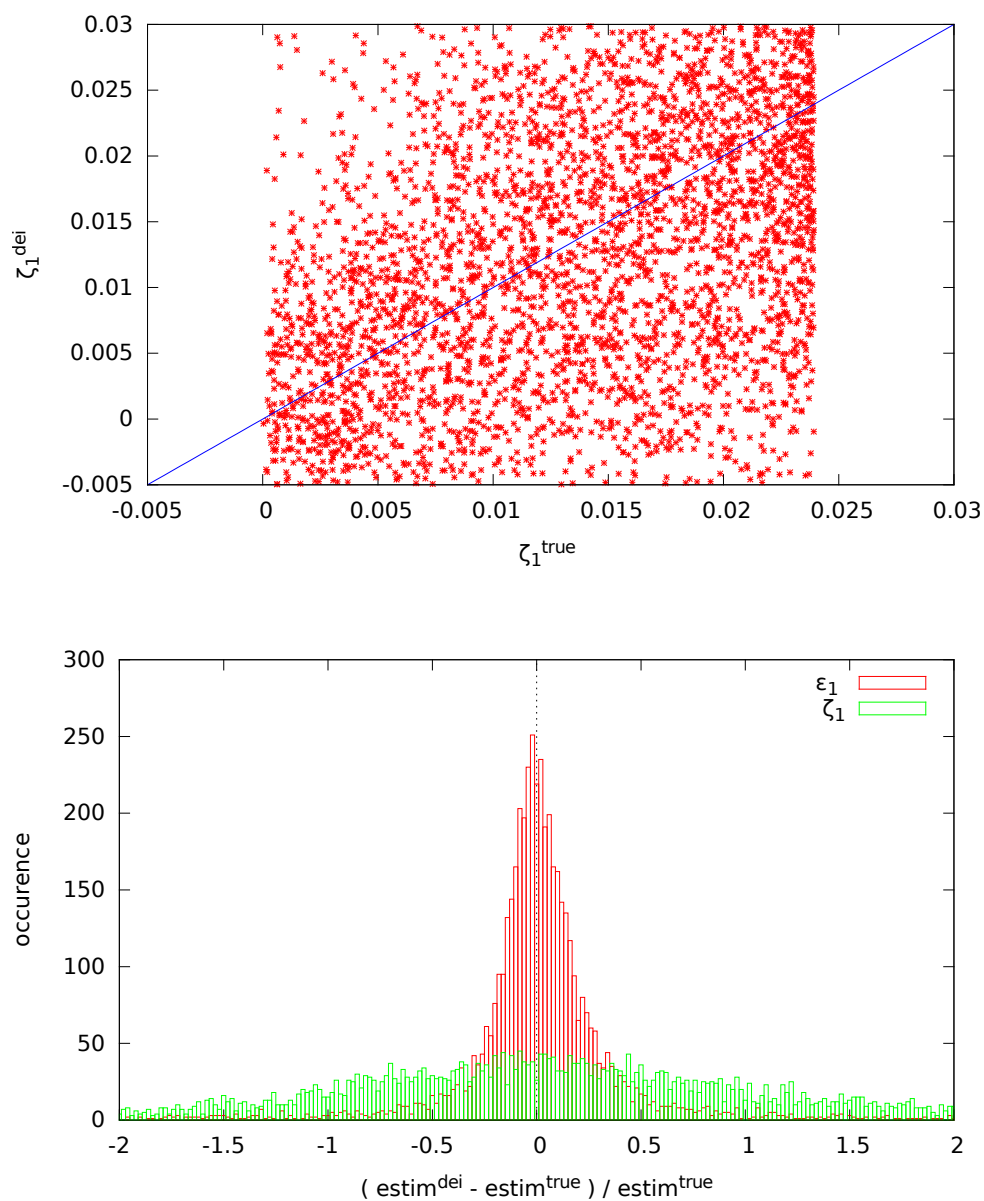
Figure 4.6: Deimos shape measurements for flexed galaxies. *Upper panel:* Values measured by DEIMOS for the spin-1 distortion estimator ζ_1 vs real values. *Lower panel:* Distribution of the relative residuals for the estimator ζ_1 (in green) and for the ellipticity estimator ϵ_1 (in red).
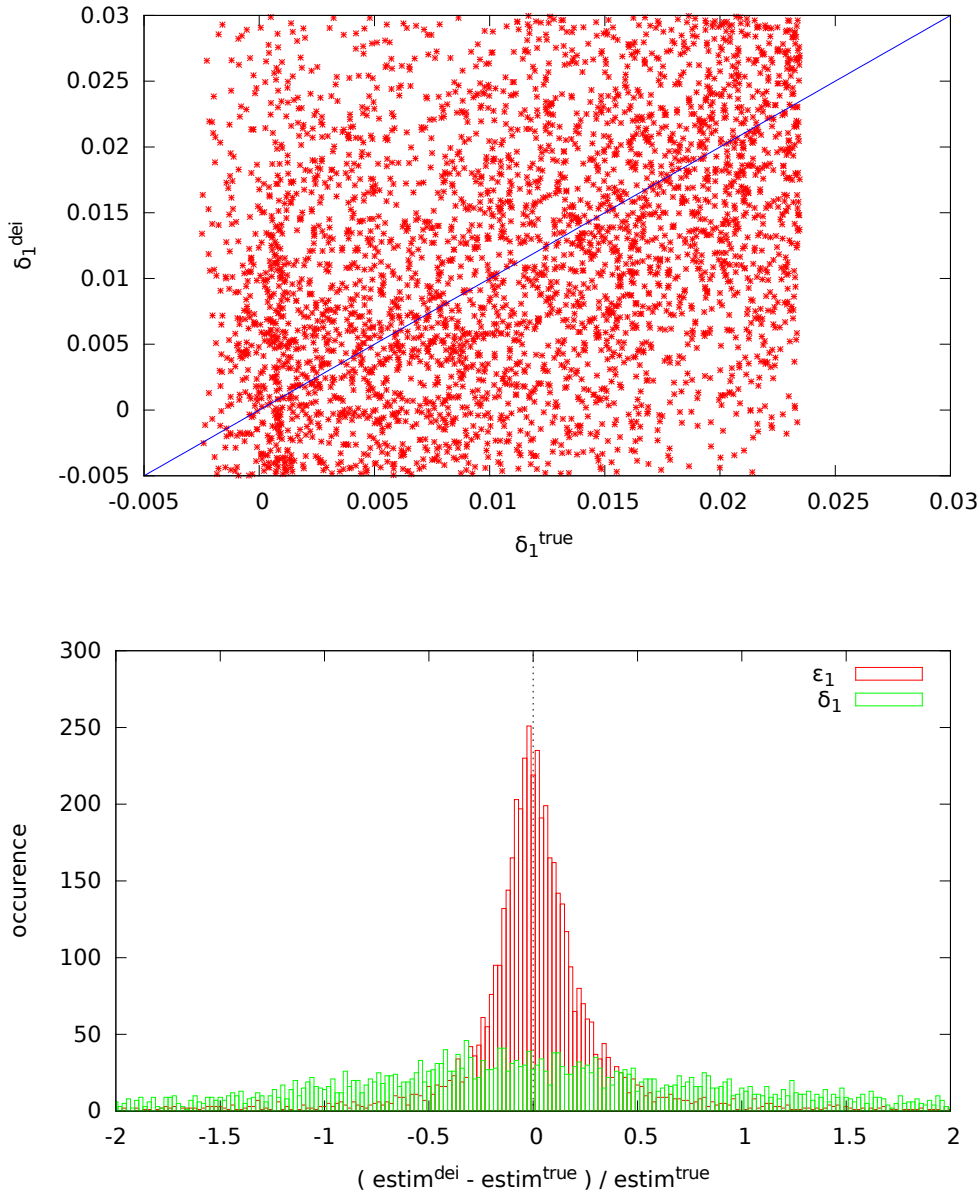
Figure 4.7: Deimos shape measurements for flexed (and sheared) galaxies. *Upper panel:* Values measured by DEIMOS for the spin-3 distortion estimator δ_1 vs real values. *Lower panel:* Distribution of the relative residuals for the estimator δ_1 (in green) and for the ellipticity estimator ϵ_1 (in red).

moments. This fact, then, suggests that a proper choice of the WF shape could turn out to be essential in order to extract the low signal from the noise.

To understand the role played by the shape of the WF on the spin-1 and spin-3 distortion measurements, we performed the following test, based on a simple toy model: we assumed a circular Sérsic galaxy and we lensed it, assuming a non-zero value only for the G flexion field. In this test, we did not convolve the galaxy with a PSF. We then produced 5000 different noisy realizations of the image of this G-flexed circular galaxy and we measured the SB moments of these images, using a flexed WF obtained by lensing a circular Gaussian WF. The shape of the flexed weight function is obtained from the coordinate transformation described by equation 2.35, and in the specific case of only G flexion having non-zero values, it is given by the following formula:

$$W(x_1, x_2) \equiv \exp\left(-\frac{x_1'^{\,2} + x_2'^{\,2}}{2s^2}\right) \, , \tag{4.18}$$
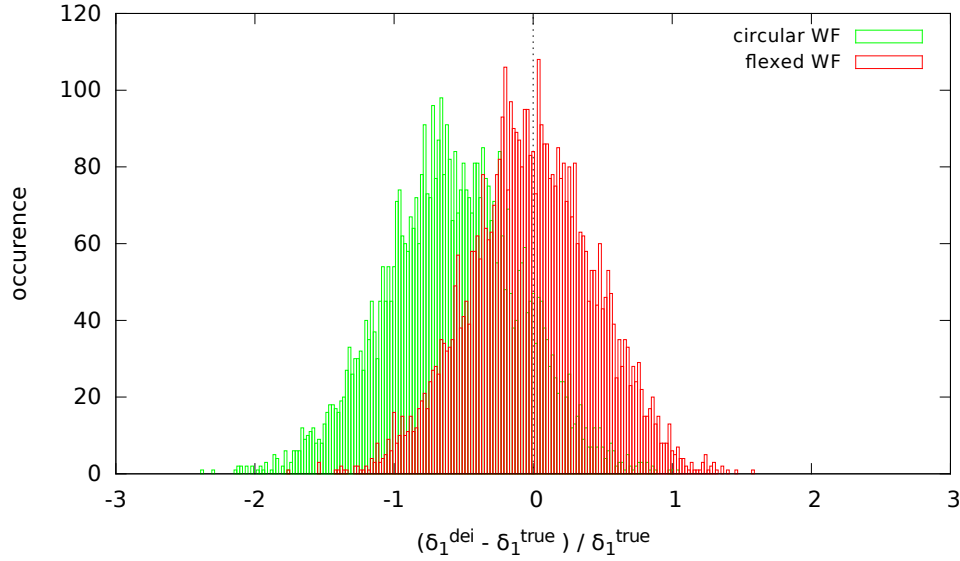
where:

$$
\begin{aligned}
x_1' &= x_1 + \frac{1}{4}G_1(x_1^2 - x_2^2) + \frac{1}{2}G_2 x_1 x_2 \, , \\
x_2' &= x_2 - \frac{1}{2}G_1 x_1 x_2 + \frac{1}{4}G_2(x_1^2 - x_2^2) \, .
\end{aligned}
\tag{4.19}
$$

For this test, we proceeded in a non-blind manner, and we assigned to the WF the correct size and the correct amount of G flexion. The performance of this version of DEIMOS in the measurement of the spin-3 distortion estimator δ, for 5000 different noisy realizations of the image of a circular Sérsic galaxy ($R_e = 3$ pixels, $n_s = 1$), lensed with reduced flexion $G = (0.01.0)$, is shown in figure 4.8. In the same plot we present also the results obtained with a version of the code which uses instead a circular WF of correct size. As we can see in these plots, the adoption of a flexed WF greatly improves the estimates of δ, producing a distribution of the measured δ_1 which, though still quite broad, is centered on the real value of δ_1, differently from the distribution obtained when applying a circular WF, which, instead, appears biased towards lower values of δ_1.

It is important to note that, while performing these tests, we realized that, in the case of flexed WF, a crucial factor to obtain reasonable estimates of δ is to set the correction order for the deweighting n_w to odd values. We ascribe this to the fact that the odd order terms in the Taylor expansion of the inverse of the WF are the ones that depend linearly on the G flexion, while the even oder terms depend only on the square of G. When truncated to even order the approximated inverse WF is thus more circular then when truncated at odd
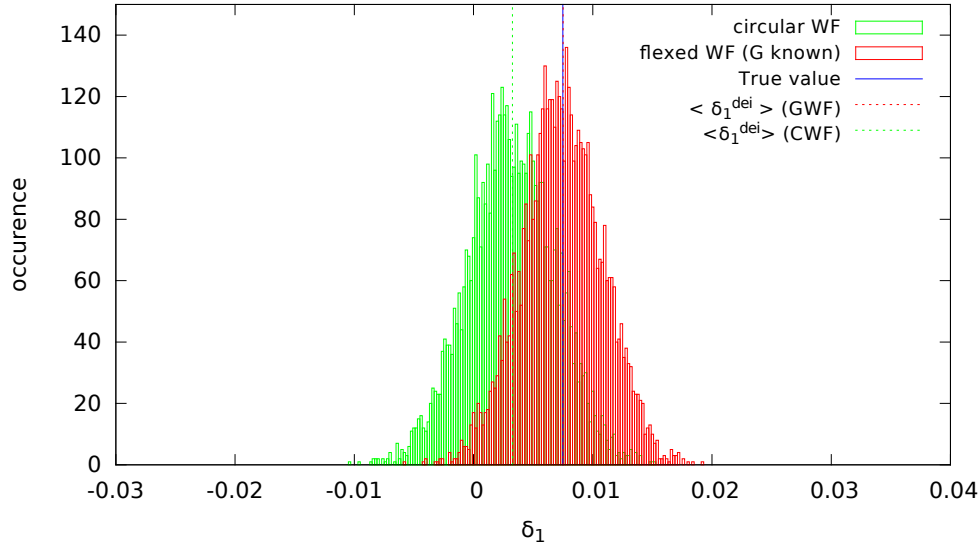
(a) Distribution of the spin-3 distortion estimator

(b) Distribution of residuals

Figure 4.8: Deimos shape measurements for flexed (intrinsically circular) galaxies. The results shown are obtained with two different versions of DEIMOS: in *red* the results obtained by applying a flexed WF, where the correct value of flexion is assumed; in *green* the results obtained when applying a circular WF. In both cases we assumed a scale for the WF $s = 3$ pixels, while we set $n_w = 3$ for the flexed WF case and $n_w = 4$ for the circular WF run. *Upper panel:* Distribution of the values of δ_1 measured by DEIMOS. The dashed vertical lines represent the mean of the distributions and the solid vertical line the true value of δ_1. *Lower panel:* Distribution of the relative residuals for the δ_1 estimator.
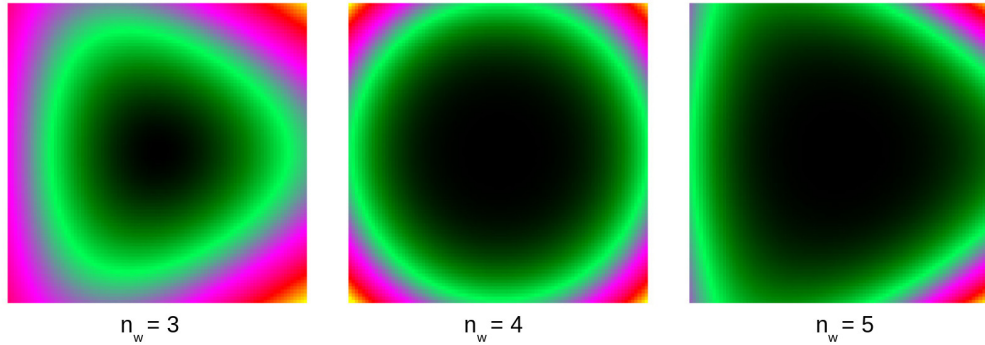
$n_w = 3$ $n_w = 4$ $n_w = 5$

Figure 4.9: Taylor expansions of the inverse of the flexed WF, truncated at different orders n_w. This function is the function W_{Tay}^{-1} used in equation 4.12, to obtaine the deweighted moments as combinations of higher order weighted moments.

order (see figure 4.9), leading to a residual WF contamination in the measured moments.

Test 3: DEIMOS with blind flexed WF

With Test 2 we showed how assuming a correct shape for the weight function makes an important difference in the estimate of the higher order distortions. We, now, try to loosen some of the assumptions made in that test.

The test consists in running DEIMOS on the same 5000 noisy images of the circular flexed galaxy, but, this time, in a blind fashion, meaning that we start from a circular WF and allow DEIMOS to match, through an iterative process, the value of the G flexion by which to lens the WF. The results are presented in figure 4.10, where they are compared to the results of the previous non-blind test. We can see that, although the distribution of the measured δ is still centered on the right true value, the dispersion significantly increases, meaning that there is a good fraction of images for which the measured δ differs from more than 100% from the real value.

Tests on convolved flexed galaxies

Before drawing our conclusions, we still want to mention the results obtained by loosening a different assumption among the ones made in Test 2. In particular, we dropped the assumption that the impact of the PSF on the galaxy shape is negligible. We thus run the same version of DEIMOS used in Test 2 on 5000
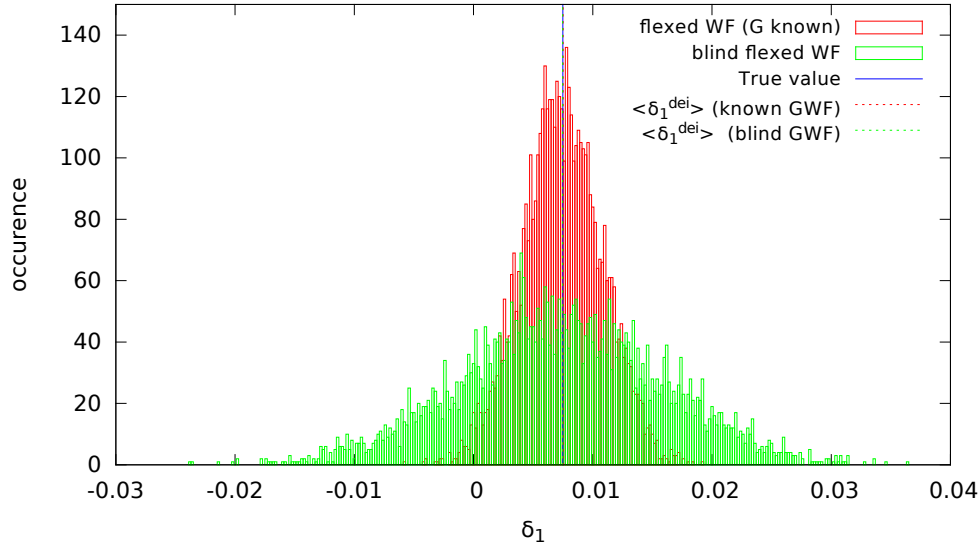
(a) Distribution of the spin-3 distortion estimator
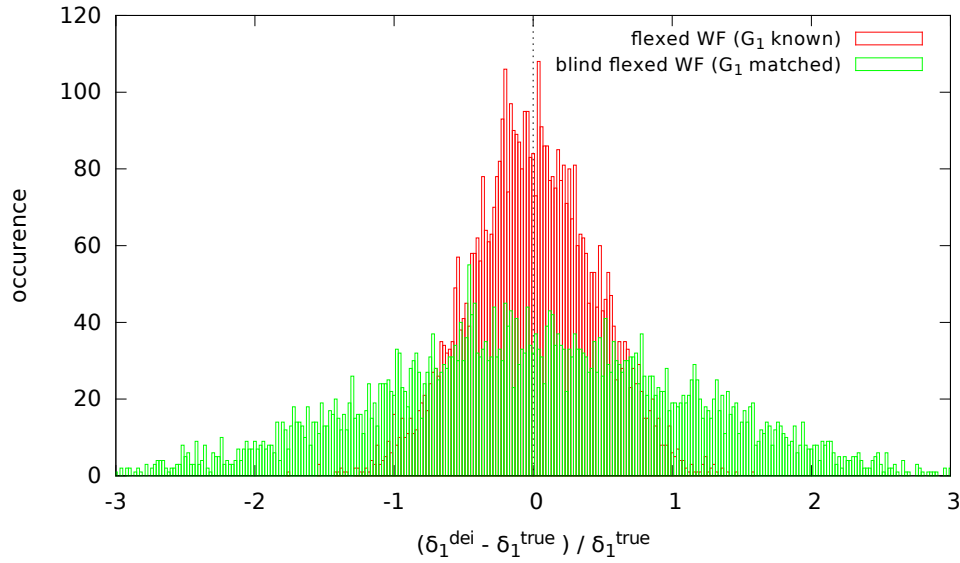
(b) Distribution of residuals

Figure 4.10: Deimos shape measurements for flexed (intrinsically circular) galaxies. The results shown are obtained with two different versions of DEIMOS: in *red* the ones obtained by applying a flexed WF, where the correct value of flexion is assumed; in *green* the results obtained by using a blind flexed WF, matched to the source through an iterative process which looks for the WF shape which maximizes the signal-to-noise ratio. In both cases we assumed $s = 3$ pixels and $n_w = 3$. *Upper panel:* Distribution of the δ_1 values measured by DEIMOS. The dashed vertical lines represent the mean of the distributions and the solid vertical line the true value of δ_1. *Lower panel:* Distribution of the relative residuals for the δ_1 estimator.
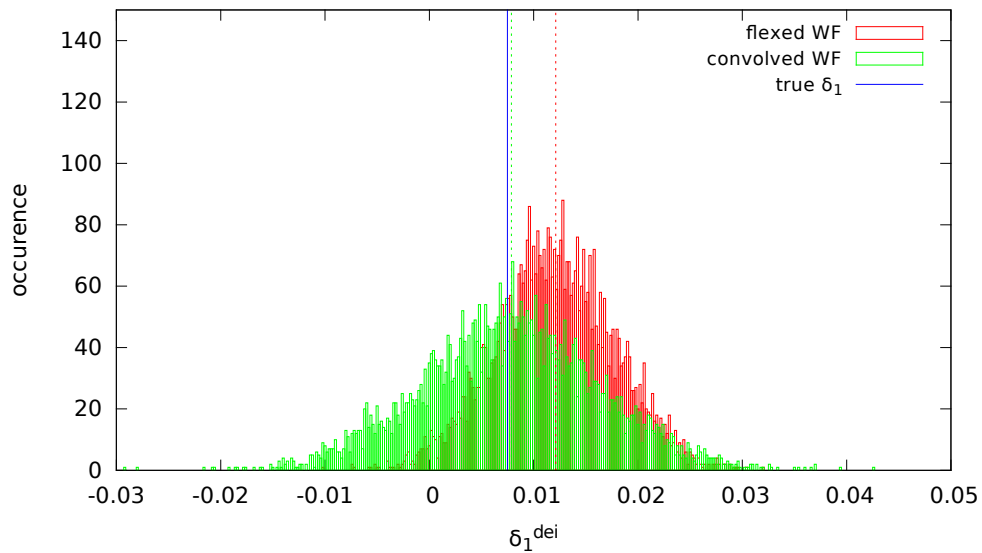
Figure 4.11: Deimos shape measurements for flexed (intrinsically circular) galaxies convolved with a circular PSF. The distribution of values of δ_1 estimated with DEIMOS is compared to the true value (vertical blue line) for two different tests. In *red* the results obtained by applying a flexed WF to the convolved images; in *green* the results obtained by applying a WF with the same shape of the convolved object. The vertical dashes lines represent the mean values of the two distributions.

different noisy realizations of a circular galaxy, lensed with only G flexion and convolved with a circular Moffat PSF with $\beta = 9$ and FWHM= 2 pixels. The distribution that we obtained by applying the non-blind flexed WF version of DEIMOS on this sample of images appeared biased towards higher values of δ and presented a larger dispersion compared to the distribution obtained in Test 2. We ascribed this bias to the fact that the convolution changes the shape of the galaxy, thus making a WF given by a flexed circular Gaussian not an appropriate choice anymore.

To investigate this idea, we calculated, under some simplifying hypothesis, the analytic shape of the object obtained by the convolution of galaxy and PSF, in order to later assign this shape to the DEIMOS WF. The assumptions we made are the following: the galaxy is described by a circular Gaussian profile with standard deviation σ, lensed with only G_1 flexion, while the PSF is represented by a circular Gaussian with standard deviation β. Under these conditions, the convolved profile reads:

$$[I * P](x_1, x_2) = \frac{1}{2\pi(\sigma^2 + \beta^2)} e^{-\frac{x_1^2 + x_2^2}{2(\sigma^2 + \beta^2)}} \left[1 + \frac{G_1}{4} \frac{\sigma^4(x_1^3 - 3x_1 x_2^2)}{(\sigma^2 + \beta^2)^3} \right]. \quad (4.20)$$

The calculations that led to this profile followed this line of thought: first we calculated the Fourier transforms of the PSF and of the galaxy profiles, in particular, we used the stationary phase method[6] to obtain the Fourier transform of the flexed Gaussian, then we multiplied the two Fourier transforms and finally back-transform their product.

We, then, produced 5000 different noisy realizations of the image of a flexed Gaussian galaxy convolved with a circular Gaussian PSF and we applied DEIMOS to these images, using a WF with shape given by equation 4.20. The bias in the measured δ distribution, observed in the previous test, in this case drastically decreases, as shown in figure 4.11.

Conclusions

In this chapter, we have presented some representative tests used to investigate the ability of the DEIMOS algorithm to measure flexion-induced distortions. Based on the results we showed, it appears clear that measuring these higher order distortions is not an easy task, even in very simplified situations, like those considered in the previous tests. Even if based on simple toy models, these tests

---

[6]The stationary phase method is a procedure for evaluating oscillatory integrals of the form: $I = \int_{-\infty}^{\infty} F(x)e^{-i\phi(x)}$, where $\phi(x)$ is a rapidly-varying function of x, and $F(x)$ is slowly-varying (by comparison).

allowed us to realize that an accurate match of the weight function shape to the source shape is of fundamental importance for a successful inference of the δ estimator. However, this matching does not seem to be a feasible task, due to the higher impact of noise on the 3rd and 4th order moments, compared to the case of shear measurements. Based on these considerations, we decided to try a different approach and, as will be explained in the next chapter, instead of matching the shape of the WF to the source, we opted for using a circular WF, estimate the bias that this operation induces on the distortion estimators and finally correct for this bias.

Chapter 5

FLEXION WITH BIAS CORRECTION

In continuation of the work presented in the previous chapter, we will here describe a new approach that we have tested concerning the measurement of the spin-1 and spin-3 distortion estimators ζ and δ. The method we used is still based on DEIMOS, and thus on the measurements of the SB moments, however it differs in the solution chosen to correct for the changes induced in the moments by the necessary weighting procedure. Based on the results of the tests illustrated in chapter 4, we decided to follow a new approach and, instead of matching the shape of the WF to the source shape and then calculating the deweighted moments with the formulae given in table 4.2, we opted for applying a circular WF and then correcting the SB moments for the bias introduced into them by this weighting process.

The algorithm we used to perform the tests presented in this chapter is derived from a modified version of DEIMOS. In the following, we will highlight the changes we introduced, while we refer to chapter 4 for a detailed description of the original DEIMOS algorithm.

The chapter is organized as follows: in section 5.1 we explain how the bias is defined and how we can estimate it; in section 5.2 and 5.3 we present the results of some tests performed with different versions of the bias correction method; finally, in section 5.3, we draw our conclusions.

5.1   Correcting for the weight function impact

Let us imagine to observe a source characterized by surface brightness $I(\boldsymbol{x})$. Unfortunately, what we actually observe is not $I(\boldsymbol{x})$, but the function:

$$G(\boldsymbol{x}) = I(\boldsymbol{x}) * P(\boldsymbol{x}) + N(\boldsymbol{x}) , \tag{5.1}$$

where $P(\boldsymbol{x})$ is the PSF kernel, which embodies the effects of atmospheric turbulence and misalignments in the optics, and $N(\boldsymbol{x})$ represents the noise, due to finite number of photons from the source, CCD electronics and sky brightness. For this reason, though we aim to obtain the following SB moments:

$$\{I\}_{i,j} \equiv \int d^2 x \, I(\boldsymbol{x}) x_1^i x_2^j \;, \tag{5.2}$$

we have no access to them. Instead, what we can actually measure are the weighted moments of the noisy and convolved object:

$$\{I^w\}_{i,j} \equiv \int d^2 x \, [I(\boldsymbol{x}) * P(\boldsymbol{x}) + N(\boldsymbol{x})] \cdot W(\boldsymbol{x}) \, x_1^i x_2^j \;, \tag{5.3}$$

where W is a properly chosen WF.

We saw in chapter 4 how DEIMOS deals with the convolution effects and recovers, in an exact manner, the unconvolved moments, $\{I\}_{i,j}$, from the convolved ones, $\{I^*\}_{i,j}$, and how it corrects for the WF-induced changes in the moments. In this chapter, we propose and test a different solution to this second problem. The moments de-weighted with the new method, which we are going to illustrate below, will then be deconvolved according to the standard deconvolution algorithm of DEIMOS.

In order to find the correction terms that we have to apply to the moments to compensate the changes induced by the weight function, let us imagine to measure the weighted moment $\{I^w\}_{i,j}$ of a given source, for m different noise realizations of its image. In this case, we can define the bias introduced by the weighting procedure on the corresponding unweighted moment $\{I^*\}_{i,j}$, in the following way:

$$b_{i,j} \equiv \langle \, \{I^*\}_{i,j} - \{I^w\}_{i,j} \, \rangle, \tag{5.4}$$

where the angle brackets denote here an average over the m different noise realizations. Inserting in equation 5.4 the correct expressions for the moments, we get:

$$
\begin{aligned}
b_{i,j} &= \int d^2 x \, \langle I(\boldsymbol{x}) * P(\boldsymbol{x}) - [I(\boldsymbol{x}) * P(\boldsymbol{x}) + N(\boldsymbol{x})] \cdot W \rangle \, x_1^i x_2^j \;= \\
&= \int d^2 x \, \langle I(\boldsymbol{x}) * P(\boldsymbol{x}) \rangle \cdot (1 - W) \, x_1^i x_2^j + \int d^2 x \, \langle N(\boldsymbol{x}) \rangle \cdot W \, x_1^i x_2^j \;= \\
&= \int d^2 x \, [I(\boldsymbol{x}) * P(\boldsymbol{x})] \cdot (1 - W) \, x_1^i x_2^j \;,
\end{aligned}
\tag{5.5}
$$

where we have used the fact that $\langle N(\boldsymbol{x}) \rangle = 0$. For a given object, the bias on the moment $\{I^*\}_{i,j}$ is thus given by the moment $i + j$ of the convolved

object weighted with the function $1 - W$. Hence, if we are able to obtain a first approximation for the shape of the convolved object, we can use it to estimate the bias by which the weighted moments need to be corrected.

In the situation typical for lensing studies, in which we observe many different objects subjected to the same lensing fields (instead of having different noisy realizations of the same object), we can follow an analogous reasoning. In this case, the average used in the bias definition 5.4 refers to the average over the different objects. Hence, for each galaxy, the bias on the moment $i + j$ is given by the moment of the mean convolved object weighted with the function $1 - W$:

$$b_{i,j} = \int d^2x \ \langle \ I(\boldsymbol{x}) * P(\boldsymbol{x}) \ \rangle \cdot (1 - W) \ x_1^i x_2^j \ . \tag{5.6}$$

Having obtained an expression for the bias induced on the different moments by the application of a generic weight function $W(\boldsymbol{x})$, we can now implement a bias correction algorithm and test its performance in the measurement of the spin-1 and spin-3 distortion estimators. For this purpose, we will again make use of mock images of lensed galaxies, produced with the pipeline illustrated in section 4.2.

5.2 Mean object bias correction

The first tests that we are going to present refer to the second case we mentioned above, i.e. the case in which the bias is estimated on the mean object of the convolved galaxy population. To perform these tests, we simulated a population of 1000 elliptical Sérsic galaxies, lensed with both shear and G flexion ($g = (0.1, 0)$, $F = (0, 0)$, $G = (0.01, 0)$). We measured the weighted moments of each image using a circular Gaussian weight function W and then we corrected these moments by adding the biases estimated on the mean convolved object, as defined in equation 5.6:

$$\{I^*\}_{i,j} = \{I^w\}_{i,j} + b_{i,j} \ . \tag{5.7}$$

Finally, we deconvolved the moments obtained in this way, following the standard DEIMOS algorithm for deconvolution (see section 4.1). With this set of moments we constructed, for each galaxy, the estimator δ^{meas} and compared it to the one calculated before applying convolution and noise degradation, δ^{true}.

Initially, we estimated the bias making use of the mean object of the population obtained from the noise-free convolved images. In figure 5.1, we report, for this first test, the comparison between the measured and the real distributions

of δ_1 (upper panel) and the distribution of the relative residuals of δ_1 (bottom panel). From these plots it appears clear that the bias correction method, in the version in which the bias is estimated on the mean object, leaves a residual bias in the values that we measure for the δ estimator. We ascribe this surviving bias to the fact that the corrections for the moments estimated on the mean object cannot compensate exactly for the effect of the WF on a specific galaxy, whose shape will generally be more peculiar compared to the shape of the mean object. Nevertheless, the distribution of the residuals shows how the relative errors have considerably decreased compared to the tests presented in the previous chapter, where the deweighting algorithm of DEIMOS was used. In particular, with the bias correction method we do not obtain relative errors larger than 45% on any object.

Unfortunately, in practical applications we do not have access to the noise-free images in order to construct the mean object used to estimate the bias. For this reason, we run a second test in which the mean object is obtained from the noisy convolved images. Note that, due to the fact that, in the bias definition 5.6, the function $1-W$ is used for the weighting, the largest contribution to the correction terms is given by the external regions of the mean object image. In the case in which the mean object is obtained from noisy images, these regions will show a residual noise signal (see figure 5.2). It becomes then necessary, in order to avoid a nonsensical outcome, to set to zero the pixels whose value is below a certain threshold. We set the threshold empirically, seeking for the lowest value for which none of the background pixels survive the cutoff. In our case, the optimal threshold is found to correspond to $1/7 \cdot \sigma_n$[1]. The distribution of the residuals on the δ_1, that we obtained in this more realistic case, is shown in figure 5.3, where it is compared to the distribution obtained in the first test (where the corrections for the moments were calculated on the noise-free mean object image). It appears immediately clear that the results are, now, much more biased than in the previous test. We attribute this worsening in the outcome to the fact that the noise, which survives the average process, does not allow a sufficiently precise reconstruction of the mean object shape. This is confirmed by the fact that the distribution of the measured δ appears to be less biased if we increase the number of galaxies in the population, allowing a less noisy reconstruction of the mean object shape.

Based on these considerations, we decided to return to the first definition of bias that we gave in section 5.1, and calculate (and correct for) the bias introduced by the WF on each specific object, as we will explain in the next section.

---

[1]Identifying the value for the cutoff with this procedure is essentially equivalent to set the threshold equal to three times the standard deviation of the mean object background.
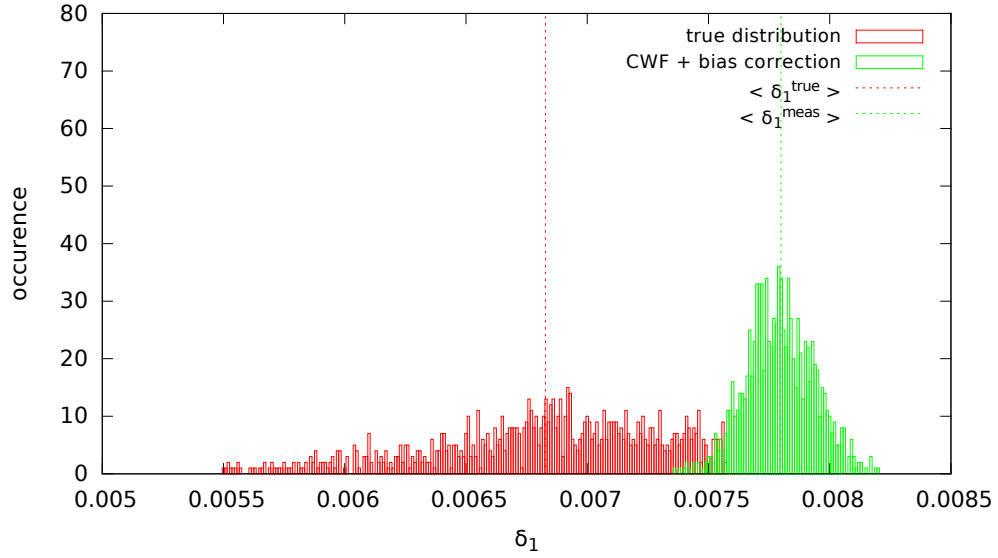
(a) Distribution of spin-3 distortion estimator
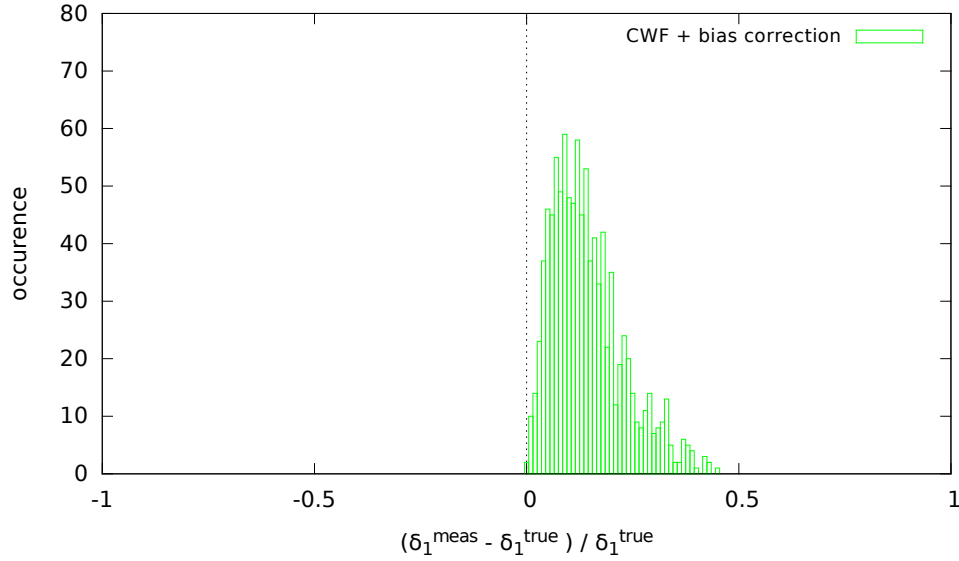
(b) Distribution of relative residuals

Figure 5.1: Performance of the bias correction method (bias estimated on the noise-free mean object) on the measurement of the δ estimator for a population of 1000 Sérsic galaxies with $n_s = 1$, $R_e = 3$ pixels and intrinsic ellipticities sampled from a Rayleigh distribution with $\sigma_\epsilon = 0.3$. The galaxies are convolved with a Moffat PSF ($\beta = 3$, FWHM= 3 pixels), and degraded with Gaussian pixel noise with standard deviation $\sigma_n = 10^{-3} \cdot$ flux. Finally, they are lensed with the following reduced lensing fields: $g = (0.1, 0)$, $F = (0, 0)$, $G = (0.01, 0)$. *Upper panel:* Comparison between the real and the measured distributions of the δ_1 estimator. *Lower panel:* Distribution of the relative residuals.
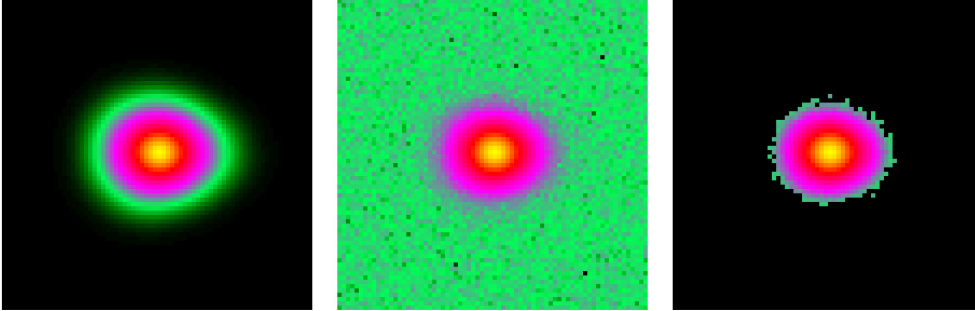
Figure 5.2: Mean object of the mock population of galaxies. *Left panel:* Mean object obtained from the noise-free images. *Central panel:* Mean object obtained from the noisy images. *Right panel:* Mean object obtained from the noisy images, setting to zero the pixels under a certain cutoff ($1/7 \cdot \sigma_n$ in this specific case). The images are plotted in logarithmic scale colormap.

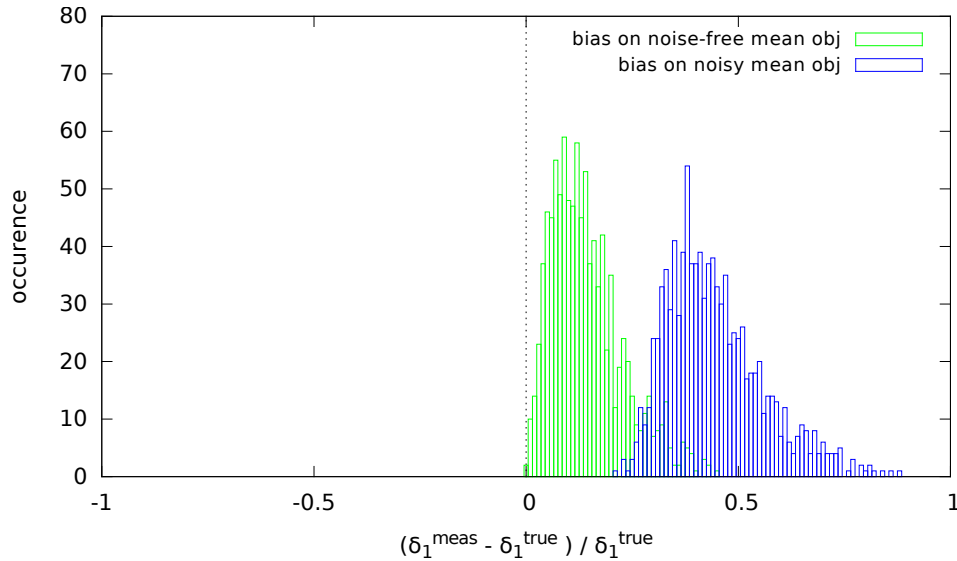Figure 5.3: Distribution of the δ_1 relative residuals for two different tests made with the bias correction method: in *green* the values obtained when the bias is estimated on the noise-free mean object; in *blue* the results obtained when the correction terms are estimated on the mean object constructed using the noisy images and then setting to zero the pixels with values smaller than $1/7 \cdot \sigma_n$.

5.3   Single object bias correction

As we saw in section 5.1, the change in the SB moments induced by using a weight function W to control the noise can be corrected by adding to the weighted moments the terms given by equation 5.5, which are simply the moments of the convolved object itself, weighted with the function $1 - W$. In light of this situation, we implemented and tested an algorithm in which the correction terms are estimated, for each object, on a reconstructed noise-free image of the object itself.

To obtain this first approximation for the shape of the convolved object we assumed some prior knowledge about our population. In particular, the reconstructed galaxies have been modeled with the right type of profile (a Sérsic profile with the correct values of R_e and n_s) and the PSF profile was also assumed to be known exactly. On the other side, ellipticity, centroid and lensing fields have been estimated, for each object, from the noisy image itself, by running a standard version of the DEIMOS algorithm with circular WF. Indeed, from the moments measured with DEIMOS, we obtained an estimate of centroid and ellipticity (both intrinsic ellipticity and shear) of each galaxy; finally, we used the mean ζ and mean δ values found with DEIMOS to estimate, through the approximated linear relations 3.8, the flexion fields F and G, by which to lens the galaxies.

The results that we are going to show in this section were obtained with the following procedure: we started by simulating 1000 mock images of lensed elliptical Sérsic galaxies ($n_s = 1$, $R_e = 3$pixels, $\sigma_\epsilon = 0.3$), convolved with a Moffat PSF ($\beta = 3$, FWHM=3pixels) and degraded with Gaussian pixel noise with $\sigma_n = 0.001 \cdot$ flux. We run on these images a standard version of DEIMOS with circular WF, from which we obtained an estimate of the ellipticity and centroid of each object, as well as an estimate of the flexion fields. We used this information to create a reconstructed noise-free image of each object, which in turn was used to calculate the correction terms for the weighted moments of the specific object, as defined in equation 5.5. Then, using a circular WF, we measured the moments of the noisy image and modified them according to the correction terms just evaluated. Finally, we deconvolved the moments with the standard deconvolution algorithm of DEIMOS. With this final set of moments we constructed the spin-1 and spin-3 distortion estimators and compared them to their true values.

In figure 5.4, we present the distribution of the residuals on δ_1 obtained with this method. The figure shows the results obtained in two different cases: in green we report the results obtained with an extra assumption about the galaxies, compared to ones listed before, in particular, we assumed to know
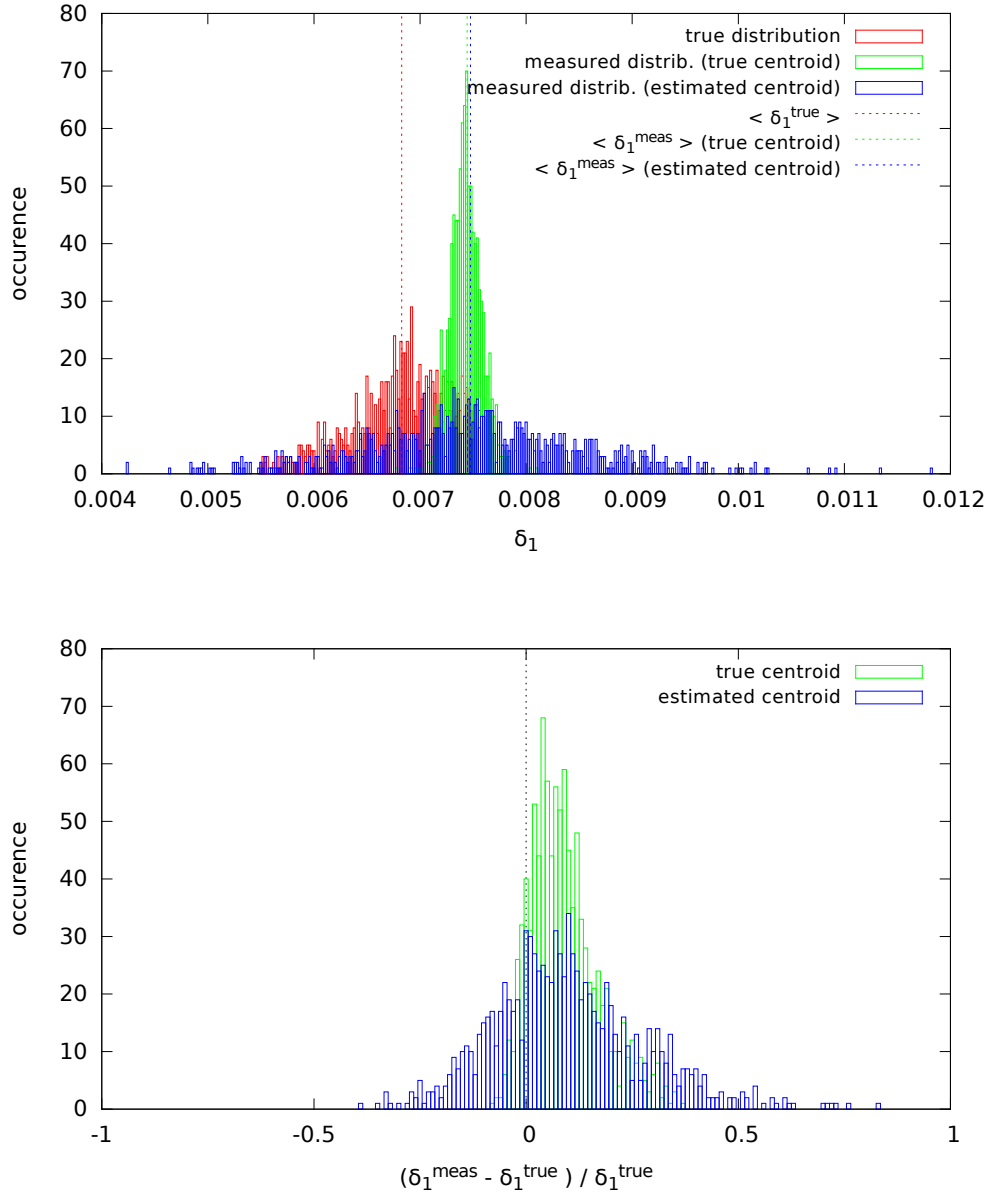
Figure 5.4: Performance of the bias correction method (bias estimated on the single objects) on the measurement of the δ estimator for the same population of galaxies described in the caption of figure 5.1. *Upper panel:* Comparison between the real (in *red*) and the measured distributions of the δ_1 estimator for two different tests: the *green* distribution refers to the case in which the WF is centered on the true object centroid; the *blue* distribution refers, instead, to the case in which the centroid estimated with DEIMOS is used. *Lower panel:* Distribution of the relative residuals (the same color code of the upper panel is used).

the real centroid of the galaxy in order to center the WF (instead of using the centroid estimated by DEIMOS); in blue, the results obtained in the general case in which the true centroid is not known and the one estimated with DEIMOS is used. Comparing these plots to those in figure 5.3, we can see that the final measured distribution of δ_1 is less biased than in the case in which the correction terms are estimated on the mean object. It is also to be noted that using the correct centroid does not decrease the final amount of bias in a significant way, however the imperfect choice of the centroid broadens the residual distribution, allowing larger relative errors.

Conclusions

Taking stock, we can conclude that, provided that a good reconstruction of the shape of the single objects is supplied, the bias correction method is definitely more successful in measuring the amount of spin-3 deformation compared to the DEIMOS algorithm, yielding a more precise, though slightly biased, measure of the δ estimator. Nevertheless, we have to consider that many assumptions on the shape of the galaxies, and of the PSF, have been made when performing our tests, as it cannot always be done in reality, and that we worked in noise conditions relatively good for weak lensing applications.

Based on these considerations, we realized that, to get a positive outcome with the bias correction algorithm, it is essential to find a method which is able to provide a good first approximation of the shape of the galaxies, without making strong assumptions on the characteristics of the sources. For this purpose, we decided to take advantage of the *PCALens* pipeline developed, within our group, by Maturi (2015, in prep.), which, given a set of background galaxy images, provides a noise-free reconstruction of these objects, through a principal component analysis (PCA, hereafter) algorithm. Even though, we, initially, thought to use the *PCALens* pipeline just in order to obtain an image reconstruction to be used in the bias estimation, we then decided to adopt the PCA approach as a new de-noising technique. In particular, as will be explain in the next chapter, we decided to measure the SB moments directly on the reconstructed noise-free image, abandoning, therefore, the idea of using a WF and then correcting for it. A detailed description of how PCA can be used to de-noise images of weak lensed galaxies and, thus, measure their SB moments is provided in the next chapter, together with a study of the performance of *PCALens* in the measurements of the higher order distortions induced by flexion.

Chapter 6

FLEXION WITH PCALens

In this chapter, we will present a new approach to galaxy shape measurements for weak lensing applications. The *PCALens* method, which we will introduce, has been developed, within our group, by Maturi (2015, in prep.). It exploits principal component analysis to de-noise the images of weak lensed galaxies, in order to measure their shape and extract weak lensing signals. In the first two sections of this chapter, we will give a brief overview of the main ideas behind PCA methods and we will describe how this technique is used for image de-noising in the *PCALens* pipeline. We will then present the results we obtained by applying the pipeline to samples of mock images of faint background galaxies. The main focus of the chapter is on the measurements of flexion-induced distortions, but we will also briefly show how the method performs in the the measurement of galaxy ellipticities. The main conclusions drawn from the results of the tests we performed are summarized in section 6.5.

6.1   Principal Component Analysis

Principal Component Analysis, or simply PCA, is a statistical procedure which aims to identify, through an orthogonal linear transformation, the most meaningful basis to re-express a given data set. PCA has become a standard tool in modern data analysis with widespread applications, like analysis of large data sets, signal de-noising, blind source separation, and data compression.

This technique, essentialy, consists in identifying the principal directions in which the data varies, the idea behind is that large variance values denote interesting dynamics in the data. Hence, the implicit hope is that a reasonable characterization of the complete data set can be obtained by projecting the data along a small number of principal components, i.e. directions of largest
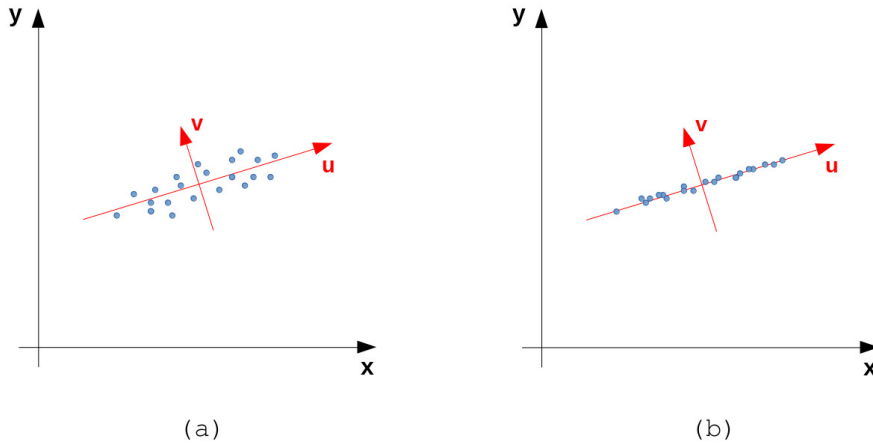
Figure 6.1: The PCA basis transformation.

variance, filtering out the noise and revealing, in this way, hidden structure.

A simple example to illustrate the PCA procedure is given in figure 6.1. In the left panel of the figure, a set of two-dimensional data points is represented in the $x-y$ coordinate system, where it has been measured. The direction along which the data points show the largest variance is indicated by the u axis, the axis v is chosen to be orthogonal to u (in a higher dimensional problem, the v axis must be chosen orthogonal to u and along the direction of second largest variance). Placing the $u-v$ coordinate system at the mean of the data, they appear, in these new coordinates, de-correlated. Moreover, we can imagine to characterize our data by using only the position along the u axis, and still obtaining a reasonable representation of the data set, as illustrated in panel b. In this way we can compress the data set, reducing the dimensionality of the problem by one. Furthermore, in case the variation of the data along the v axis is mostly due to experimental error, expressing the data by means of the only first component can be used as a de-noising technique.

The requirements that the new basis must fulfill are the following: $i)$ the new basis is a linear combination of the original basis; $ii)$ the basis vectors are orthonormal; $iii)$ the largest variance of the data comes to lie on the first basis vector (called the first principal component), the second largest variance on the second coordinate and so on.

The mathematical procedure to determine this new coordinate system consists in finding the eigenvectors and eigenvalues of the data covariance matrix. The eigenvector with the largest eigenvalue will represent the first principal

component, the eigenvector with the second largest eigenvalue the second principal component and so on.

To see how this computation is done, let us assume to start from a data set composed by n data points of dimension m. We can then represent the data set as a $n \times m$ matrix $\mathbf{X}$, where each row represents the vector corresponding to a data point in our m-dimensional space. The first step in PCA is to move the origin of the system to the mean of the data; this is done by subtracting the mean vector from each data vector. Let us call this new matrix, whose rows are the mean centered data vectors, $\mathbf{U}$. At this point the covariance matrix of the data is simply given by:

$$\mathbf{C} = \frac{1}{n-1}\mathbf{U}^T\mathbf{U} \ , \tag{6.1}$$

and has dimension $m \times m$. The following step consists in diagonalizing the matrix $\mathbf{C}$. Once the eigenvectors have been found and normalized they form an orthonormal basis. If we order them according to a decreasing value of their eigenvalues, we finally obtain the new basis that we were searching for in order to re-express our data. At this point, for example, data compression or signal de-noising can be carried out by representing the data in the subspace defined by the first $k < m$ eigenvectors.

6.2 PCALens for image de-noising

The pipeline *PCALens*, developed by Maturi (2015, in prep.), exploits PCA to perform weak lensing studies. In particular, given a set of noisy images of weakly lensed galaxies, the PCA technique is used to produce noise-free models of the galaxies in order to estimate their shape. We can summarize the method in the following steps:

- a set of n postage stamps representing the images of n weakly lensed galaxies is given as input to the pipeline;

- the images are re-written as vectors, $\boldsymbol{x}^{(1)}$, ..., $\boldsymbol{x}^{(n)}$, by simply concatenating the pixel rows of each image;

- the mean vector $\boldsymbol{x}_{mean}$ is evaluated and subtracted from each image;

- the matrix $\mathbf{U}$, which has the image vectors as rows, is used to construct the data covariance matrix $\mathbf{C} \equiv \frac{1}{n-1}\mathbf{U}^T\mathbf{U}$;

- the eigenvectors, $\boldsymbol{e}_i$, and eigenvalues, λ_i, of $\mathbf{C}$ are calculated and the eigenvectors are ordered according to decreasing eigenvalues;

- for each image $\boldsymbol{x}^{(i)}$ a de-noised model is obtained by projecting the image on the first $k \leq m$ eigenvectors:

$$\boldsymbol{x}_{mod}^{(i)} = \boldsymbol{x}_{mean} + \sum_{j=0}^{k} a_j^{(i)} \boldsymbol{e}_j \ , \qquad (6.2)$$

  where $a_j^{(i)} = (\boldsymbol{x}^{(i)} - \boldsymbol{x}_{mean}) \cdot \boldsymbol{e}_j$ and the value of k where the series is truncated depends on the specific task at hand, in particular, it can be set equal to the last component which shows features, by visually inspecting the basis, or can be found automatically, through a χ^2 minimization algorithm[1];

- the SB moments of the galaxy are evaluated on the de-noised model obtained in this way;

- the exact same procedure is performed on a sample of star images, in order to determine the PSF moments;

- once the convolved galaxy moments and the PSF moments have been evaluated, the deconvolution algorithm used in DEIMOS (see section 4.1) is applied;

- the deconvolved SB moments are finally used to construct the various distortions estimators, ϵ, χ, ζ, δ.

A general illustration of how PCA can be exploited to de-noise images of galaxies is shown in figure 6.2. In figure 6.3, we report, instead, three examples of de-noised models constructed for the images of three galaxies observed with the Subaru Telescope, the principal components used to model the galaxies have been obtained by applying the *PCALens* pipeline to a sample of 1000 galaxies from the same data set.

6.3   Ellipticity measurements with PCALens

Before using the *PCALens* method to measure the shape of galaxies which exhibit flexion-induced distortions, we want to show how the method performs

---

[1]Given an image, $\boldsymbol{x}^{(i)}$, and a model for it, $\boldsymbol{x}_{mod}$, constructed with k components, we defined: $\chi_k^2 \equiv \sum_{s=1}^{m} [x_s^{(i)} - x_{mod,s}]^2$, where the index s denotes the different pixels. Starting from $k = 1$, an iterative process is used to add, at each step, a new component to the modeling. The number of components, k, at which to stop can, then, be identified by looking for the smallest k that yields $\chi_k^2 \leq 1$, or for the smallest k which satisfies the following convergence criterion: $\{ \min\{k\} \in \aleph : \chi_k^2 - \chi_{k+1}^2 \leq t \}$, where t is a free threshold to be set.
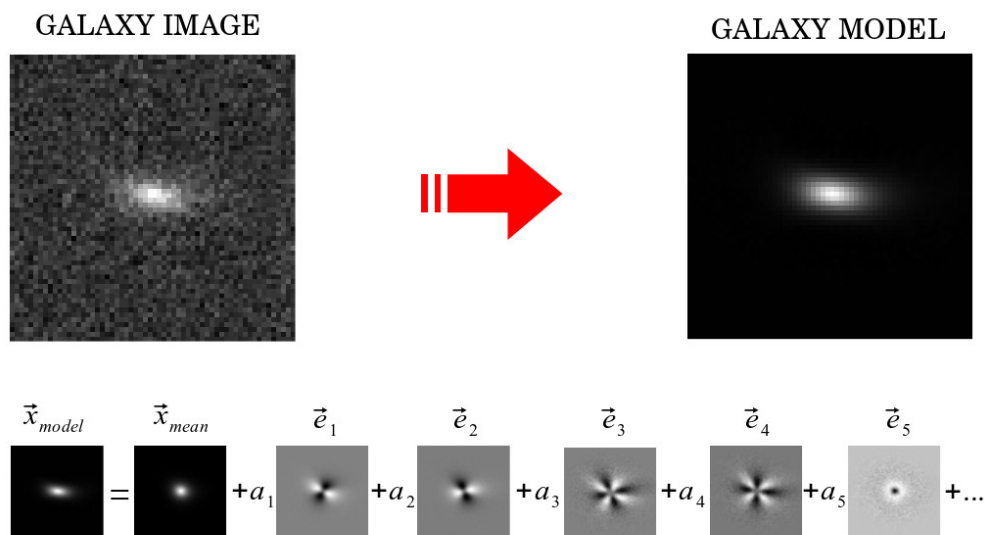
GALAXY IMAGE

GALAXY MODEL

Figure 6.2: Image de-noising with PCA. Starting from a sample of n noisy galaxy images of m pixels each, the PCA technique identifies the principal components of the sample and uses them to construct a noise-free model for each image, as the one shown in the top right panel, which represents the de-noised version of the image on the top left panel. The model is obtained by projecting the galaxy image on the first $k < m$ principal components, as sketched in the lower panel, where, for visualization purposes, the mean vector, $\boldsymbol{x}_{mean}$, and the principal components, $\boldsymbol{e}_j$, are rearranged as images. The number k of principal components to be used in the modeling can be determined with a χ^2 minimization criterion, based on the comparison of the original image to the constructed model, as well as set to a specific value, by visually inspecting the basis.
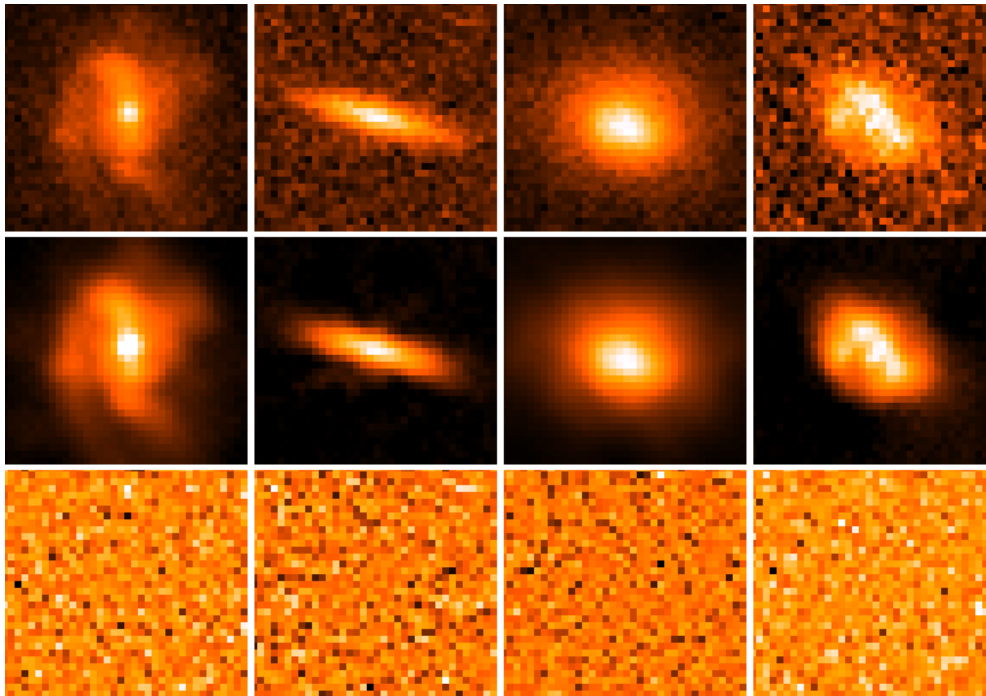
Figure 6.3: Image de-noising with PCA. *Upper panels:* Images of three real galaxies observed at the Subaru Telescope, the images are taken from the SMOKA Science Archive (http://smoka.nao.ac.jp). *Middle panels:* Corresponding de-noised models constructed with *PCALens*, using 1000 galaxy images from the SMOKA Science Archive. *Lower panels:* Residual images, obtained by subtracting the model image from the galaxy image. Figure courtesy of Matteo Maturi.

in the measurement of galaxy ellipticities. For this purpose we produced a mock sample of galaxies images, following the simulation pipeline explained in section 4.2. We, then, identified the principal components of this sample and used them to model the galaxies, according to the method explained in section 6.2. The galaxy population that we simulated is made of 5000 elliptical Sérsic galaxies with $n_s = 1$, $R_e = 3$ pixels and ellipticity randomly drawn from a Rayleigh distribution with $\sigma_\epsilon = 0.3$. In this case, we did not apply any PSF convolution or lensing transformation. Finally, the images were degraded with Gaussian pixel noise with standard deviation $\sigma_n = 10^{-3} \cdot$ flux.

The eigenvalues corresponding to the different principal components of this population are plotted in figure 6.4. We can note here how the amplitude of the eigenvalues drops rapidly with the order of the components, reaching a plateau at the 14th order, identifying the noise level. This behavior emphasizes the fact that very few components contain most of the relevant information. In figure 6.5 we present the mean object (top left panel) and the first principal components obtained for this population. As we could already expect by looking at the trend of the eigenvalue amplitudes, the last component showing features is the 13th principal component (second panel from left in the last row), afterwards the noise starts to dominate. Note that, in order to decrease the noise impact, before constructing the principal components of the sample, in each postage stamp, we set to zero all the pixels outside an ellipse enclosing the galaxy; the ellipse is aligned with the galaxy and has axes equal to 7 times the axes of the galaxy itself[2], as measured with SExtractor.

Using the principal components showed in figure 6.5, we modeled the galaxies of the mock population, letting the pipeline automatically choose the number of components to use for the modeling, through a χ^2 minimization algorithm, which looks for the smallest number of components, k, yielding a $\chi_k^2 \leq 1$. We, then, measured the SB moments on the de-noised models and constructed with them the ellipticity estimator, ϵ, which we, finally, compared to the one constructed from the moments measured on the mock image before adding the noise. In figure 6.6, we show the results of this test and we compared them to the results obtained with the standard DEIMOS pipeline on the same mock images. As can be seen from these plots, *PCALens* performs very well in the measurement of ellipticity, showing a much tighter distribution of the relative residuals on ϵ, compared to the DEIMOS method.

The results we presented in this section refer to a quite simple situation in which all galaxies have the same size and the same brightness profile and the observing conditions are relatively good (SNR $\sim 60 - 70$, as measured

---

[2]The factor 7 was found empirically, as the one representing the best compromise to obtain reconstructions less noisy but still unbiased.
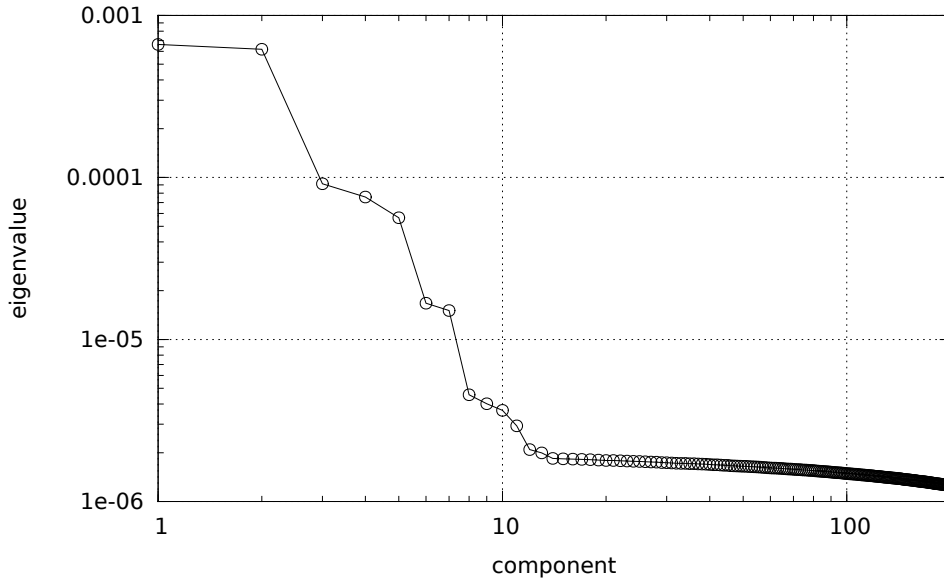
Figure 6.4: Amplitude of the eigenvalues of the principal components derived from a sample of 5000 noisy mock images of Sérsic galaxies with $n_s = 1$, $R_e = 3$ and random ellipticity.

with SExtractor). The test was just meant to compare, in a simple case, the performance of *PCALens* with that of a standard WL method like DEIMOS. Maturi (2015, in prep.) have tested *PCALens* in more realistic conditions, in particular using a simulation with 10000 galaxies having the same properties of those used in the RealNoise_Blind simulations from the GREAT08 challenge (Bridle et al., 2009, 2010), as well as in a simulation where the noise variance and the distribution in flux, scale radius and ellipticity of the sources resemble those of a stacked image obtained in a 20 minutes exposure time with the Omega-Cam mounted on the Subaru telescope. He obtained results, concerning the ellipticity measurements, similar to those reported in this chapter, hence, showing how the PCA technique can be successfully applied to WL analysis.

6.4   Flexion measurements with PCALens

Having shown how *PCALens* successfully measures the ellipticity of small faint galaxies typical of WL surveys, we now focus on the main goal of this thesis: the measurements of higher order distortions, which are introduced in the shape of the galaxies when shear and/or convergence are not constant across the image
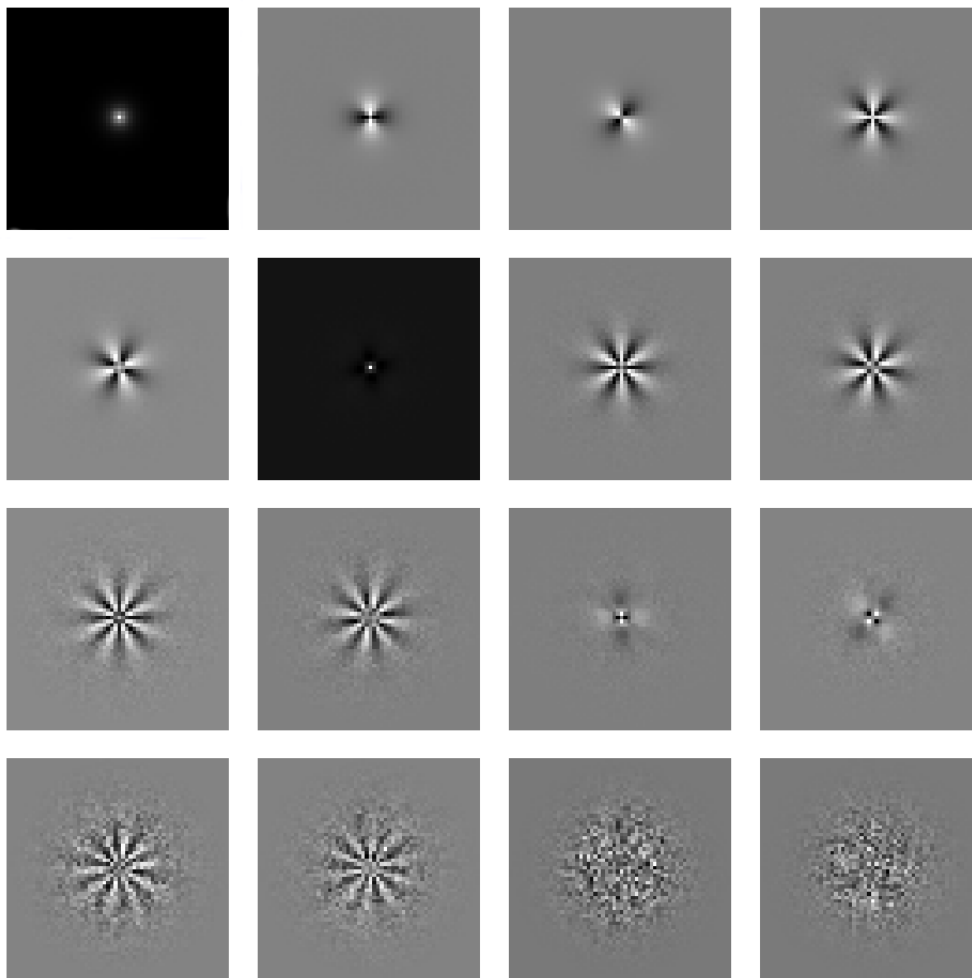
Figure 6.5: Mean vector (top left panel) and first 15 principal components derived from the noisy mock images of a population of 5000 Sérsic galaxies with $n_s = 1$, $R_e = 3$ and random ellipticity. Both the mean vector and the principal components are rearranged as images, for visualization purposes. The components are shown according to a decreasing order of their eigenvalues, going from the top rows to lower ones and moving from left to right inside each row. The complexity of the features clearly increases moving from lower to higher components. The last component showing some structures is the 13th component (last row, second panel from left), afterwards the noise does not allow to distinguish any feature.
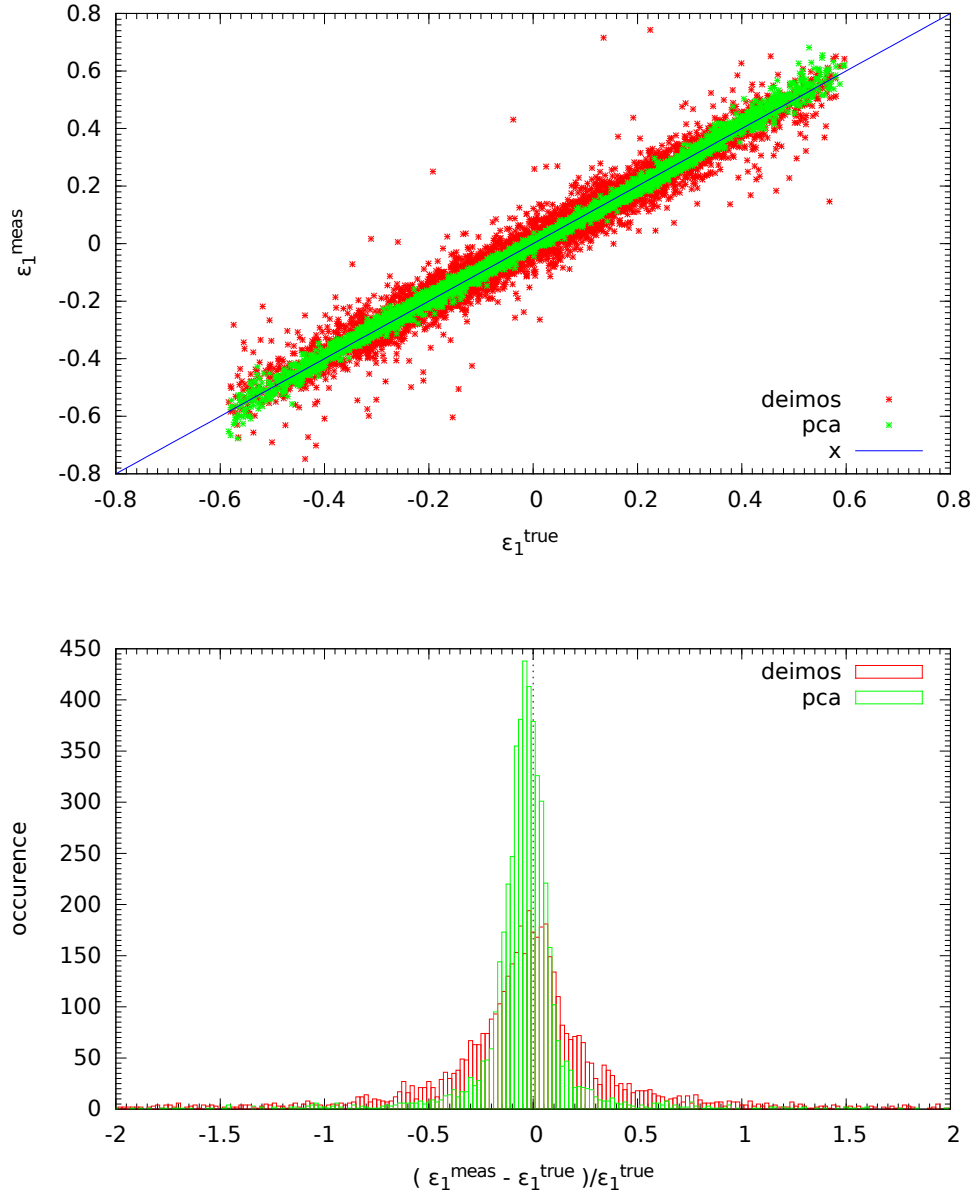
Figure 6.6: Ellipticity measurements with *PCALens*, compared to DEIMOS measurements. The mock data sample consists of a population of 5000 noisy images of Sérsic galaxies with $n_s = 1$, $R_e = 3$ pixels and intrinsic ellipticities sampled from a Rayleigh distribution with $\sigma_\epsilon = 0.3$. Gaussian pixel noise with standard deviation $\sigma_n = 10^{-3} \cdot$ flux (i.e. SNR ~ 50) was used to degrade the images. *Upper panel:* First component of the ellipticity as measured with the two methods vs first component of the true ellipticity (as estimated from the noise free image). *Lower panel:* Distribution of the relative residuals. For both panels, the situation is analogous for the second component of the ellipticity.

of the source, i.e. in presence of flexion.

One more time we will make use, in order to test our pipeline, of different samples of mock images of lensed galaxies, simulated using the pipeline described in section 4.2.

In contrast to the ellipticity measurements discussed in section 6.3, when estimating flexion we are interested in measuring the deviations from the symmetric elliptical shape. Because of this reason, we decided to align all the galaxies along their major axis before computing the principal components. In fact, if the galaxies are randomly oriented, too many components need to be used to reproduce ellipses with many different orientations and less relevance is given to the description of how much the shape of each object differs from an ellipse. On the other side, if we align all the galaxies along their major axis, the main difference among the various objects will be represented by the amount of curvature characteristic of each galaxy, meaning that very few principal components are needed to describe the ellipticity (since all the objects are elongated along the same direction), and the remaining components can focus on the description of the higher order distortions.

Based on these considerations, in the samples of mock images that we are going to use for the next tests, the galaxies have always been oriented with their major axis along the postage stamp bisector $y = -x$. This means that, in real observations, a rotation of all the galaxy images will have to be performed before computing the principal components of the sample, with the disadvantages of introducing noise in the measurements due to an inevitably imperfect alignment, as well as introducing a correlation in the pixel noise. Although this is something that will have to be considered when working with real data, for the moment, we are going to neglect these complications.

6.4.1 Tests with noise-free images

In order to investigate the ability of the *PCALens* pipeline to measure flexion-induced distortions, we initially performed tests on noise-free images of flexed galaxies. The idea is to use these tests to understand which, and how many, principal components are needed to reproduce the shape of galaxies with the necessary details to measure precisely the estimators δ and ζ and, at the same time, possibly identify particular characteristics of galaxies which favor this kind of measurements.

The tests were performed on 20 different sets of galaxies, each set corresponding to a population of 10000 Sérsic galaxies with certain effective radius, R_e, and Sérsic index, n_s. The sets differ for the particular combination of the R_e and n_s parameters, which assume values in the ranges: $R_e = 2, 4, 8, 16$ pixels and $n_s = 0.5, 1, 2, 3, 4$. For each galaxy from a certain population the amount

of the intrinsic ellipticity was drawn randomly from a Rayleigh distribution with $\sigma_\epsilon = 0.3$, while the orientation was imposed to follow the $-45°$ bisector of the postage stamp[3]. Before convolving the galaxies with a circular Moffat PSF with $\beta = 3.5$ and FWHM$= 2.85$ pixels, each object has been lensed with values of the reduced lensing fields g, F and G, randomly drawn from uniform distributions in the following ranges: $g_2 \in [-0.05, 0]$, $F_{1,2} \in [-0.006, 0.006]$, $G_{1,2} \in [0.015, 0.015]$, where, to preserve the orientation of the galaxies at $-45°$, only the second component of the shear was assumed different from zero and having negative values. Note that, in this case, every object undergoes a different lensing transformation and the particular combinations of the strengths of the lensing fields are not meant to describe a realistic lensing situation, since we are now interested in studying the capacity of the PCA algorithm to recover a variety of galaxy shapes showing spin-1 and spin-3 distortions, independently of the reasons which caused these deformations.

For each of the samples of 10000 noise-free images of galaxies we constructed the principal components and then studied how the errors on the measurements of δ and ζ vary with the number of components used in the modeling[4]. We present, in figure 6.7, the variation of the mean error on δ_1 obtained for the population characterized by $R_e = 4$ pixels, $n_s = 1$, when modeling the galaxies with 4 different numbers of principal components, specifically: 4, 5, 15 and 30 components. To produce this plot, the galaxies of the sample have been binned according to their true δ_1 value and, inside each bin, the mean absolute error, $\sum_{i=1}^{n_{bin}} \left(\delta_{1,i}^{\mathrm{pca}} - \delta_{1,i}^{\mathrm{true}} \right)$, and the mean relative error, $\sum_{i=1}^{n_{bin}} \left((\delta_{1,i}^{\mathrm{pca}} - \delta_{1,i}^{\mathrm{true}})/\delta_{1,i}^{\mathrm{true}} \right)$, have been evaluated and plotted in figure 6.7, top and bottom panel, respectively. The error bars attached to the data points in the top panel correspond to one rms of the measured δ_1 distribution inside each bin. In the bottom panel the relative mean bias is shown. The rms of the measured δ_1 distributions inside the various bins is, instead, plotted in figure 6.8. To allow a comparison between the different bins, in the bottom panel, we normalized it to the mean δ_1 value measured inside each bin.

What we can observe in these plots is that a significant improvement in the accuracy of the δ_1 measurements is obtained when the 5th component is included in the modeling. If we have a look at the principal components of this sample, shown in figure 6.9, we realize that the 4th and 5th components are those having spin-3 symmetry. It then appears clear that in order to measure

---

[3]The axis for the alignment was fixed at $-45°$ for convenience, since, compared to the x axis, it allows to have larger galaxies, once a size for the (square) postage stamps is given.

[4]Note that, in all the tests that we are going to present, we never performed the PSF deconvolution. The comparison between measured and true values of the different estimators refers then to the comparison between (measured and true) convolved quantities.

Figure 6.7: Measurement of the spin-3 δ estimator with *PCALens*, for a sample of 10000 noise-free images of Sérsic galaxies with $R_e = 4$ pixels, $n_s = 1$, characterized by different intrinsic ellipticity and lensing deformations. *Upper panel:* Mean error on δ_1, as a function of the true δ_1 value, obtained when modeling the galaxies with four different number of principal components (as indicated in the legend). Errobars correspond to one standard deviation of the measured δ_1 distribution inside each bin. *Lower panel:* Mean relative error on δ_1, as a function of the true δ_1 value.
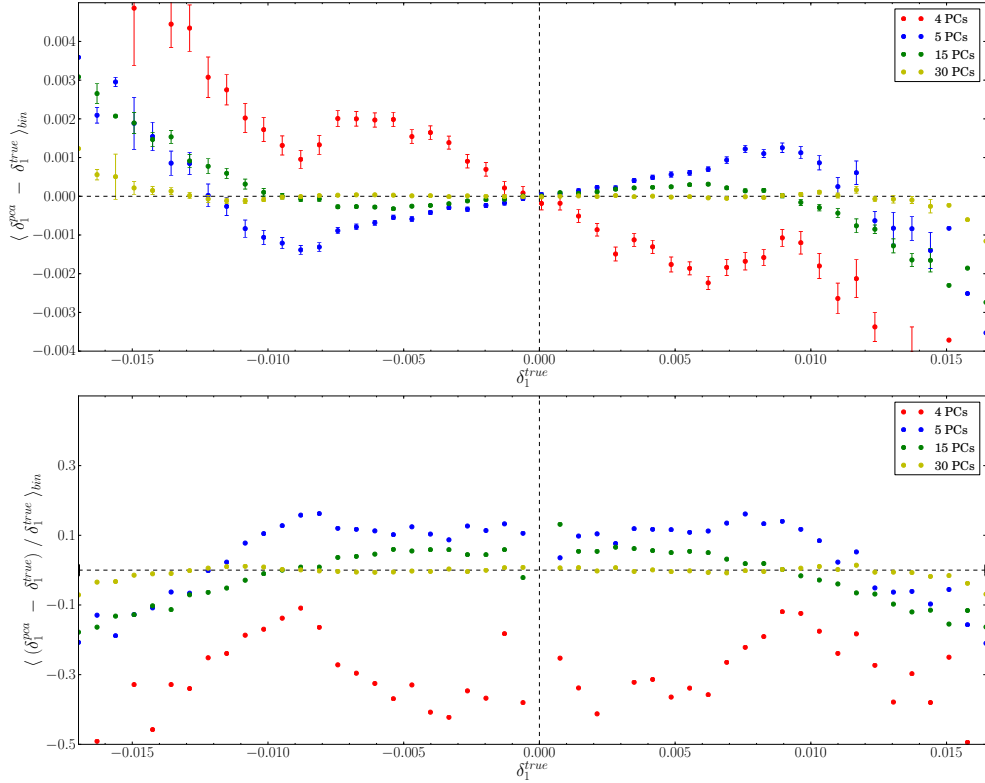
Figure 6.8: Measurement of the spin-3 δ estimator with *PCALens*, for a sample of 10000 noise-free images of Sérsic galaxies with $R_e = 4$ pixels, $n_s = 1$, characterized by different intrinsic ellipticity and lensing deformations. The different colors refer to tests made by modeling the galaxies with four different number of principal components (as indicated in the legend). *Upper panel:* Root mean square of the measured δ_1 distribution inside each δ_1^{true} bin. *Lower panel:* Root mean square of the bin normalized to the mean δ value measured in that bin.

Figure 6.9: First 8 principal components for a sample of 10000 noise-free images of Sérsic galaxies with $R_e = 4$ pixels, $n_s = 1$, characterized by different intrinsic ellipticity and lensing deformations.

the spin-3 distortion estimator, both these two basis vectors are essential. Including these components the mean errors in each bin drop below 20%, with errors around 20% only for those bins corresponding to high $|\delta|$ values. Also the dispersion of the measurements around a certain δ_1^{true} value significantly decreases when we include both the two spin-3 principal components. If we increase further the number of basis vectors used for the modeling, the mean errors gradually decrease. We can see, however, that, to reach an unbiased measurement on a large range of δ values, a high number of components is needed. In fact, even when using 30 components, the measurements relative to galaxies with the highest $|\delta|$ values are still slightly underestimated. It should be mentioned, however, that, in analogy to what is done in current weak lensing techniques, one can cope with the residual bias by calibrating the results against numerical simulations.

In figure 6.10, we present the same plots, this time for the spin-1 ζ estimator. We can observe that, in this case, including the 5th component does not change the accuracy of the ζ measurements, which, as expected, are not influenced by spin-3 features. In the case of ζ, fewer components are needed to reach similar precision as for δ, and the measurements performed on the 4-components models already present errors smaller than 20%. However we have to consider that, compared to δ, we expect this estimator to be more sensitive to the noise, since it is strongly dependent on the correct estimation of the object centroid.

As mentioned before, in our investigation, we have also compared the performance of *PCALens* on the δ and ζ measurements when applied to populations of galaxies characterized by different size or different steepness of the profile, keeping, instead, constant, between the different populations, the number of components used for the modeling. With these tests, we did not find a strong dependence of the measurement precision on the properties of the galaxies. The only relevant trend we observed is that the galaxies with smallest size ($R_e = 2$ pixels) and less steep profile ($n_s = 0.5$), generally, entail smaller relative errors. We ascribed this behavior to the fact that, as we mentioned in section 3.2, the deformations induced by flexion depend on the shape and size of the galaxies to which the lensing transformation is applied, in particular, at equal flexion fields, larger distortions are induced in the shape of larger, more concentrated or more elliptical galaxies; hence, in the population corresponding to the smallest and flattest galaxies, the lensed objects will exhibit a smaller variety of shapes, compared to the populations of larger or steeper galaxies. This higher similarity among the objects of the sample allows a simpler reconstruction of their shapes at a fixed number of components. Based on this consideration, we conclude that the accuracy in the measurement of galaxy shapes by means of PCA algorithms could benefit from constructing the principal components for

sub-samples of the galaxy images, obtained by grouping the galaxy according to similar properties.
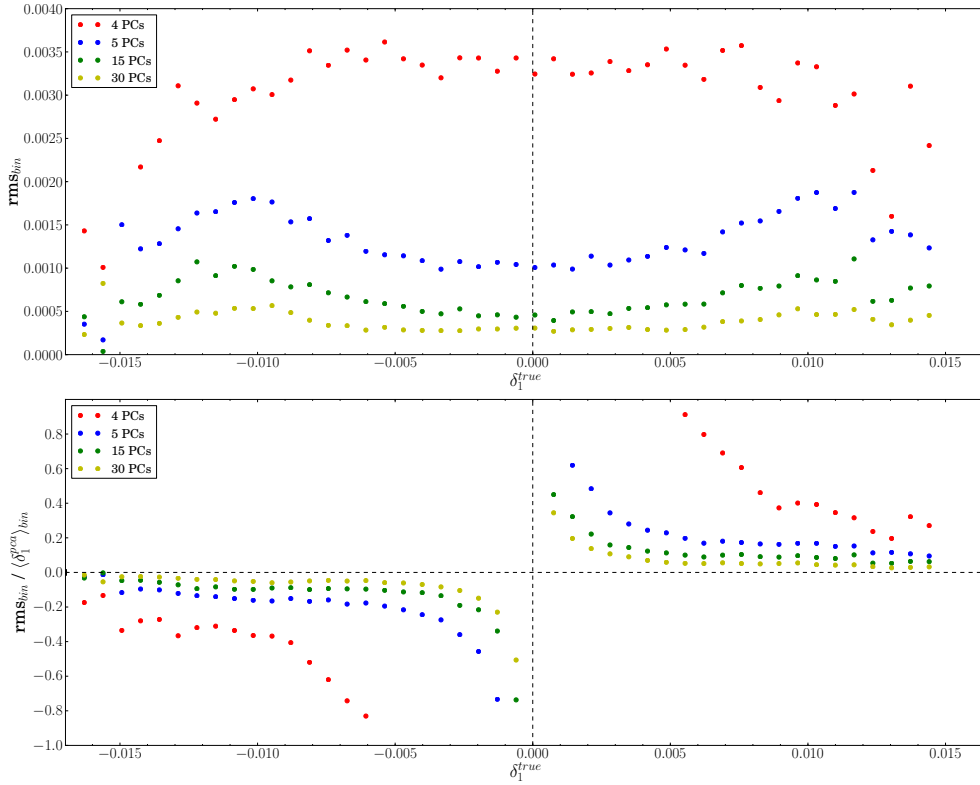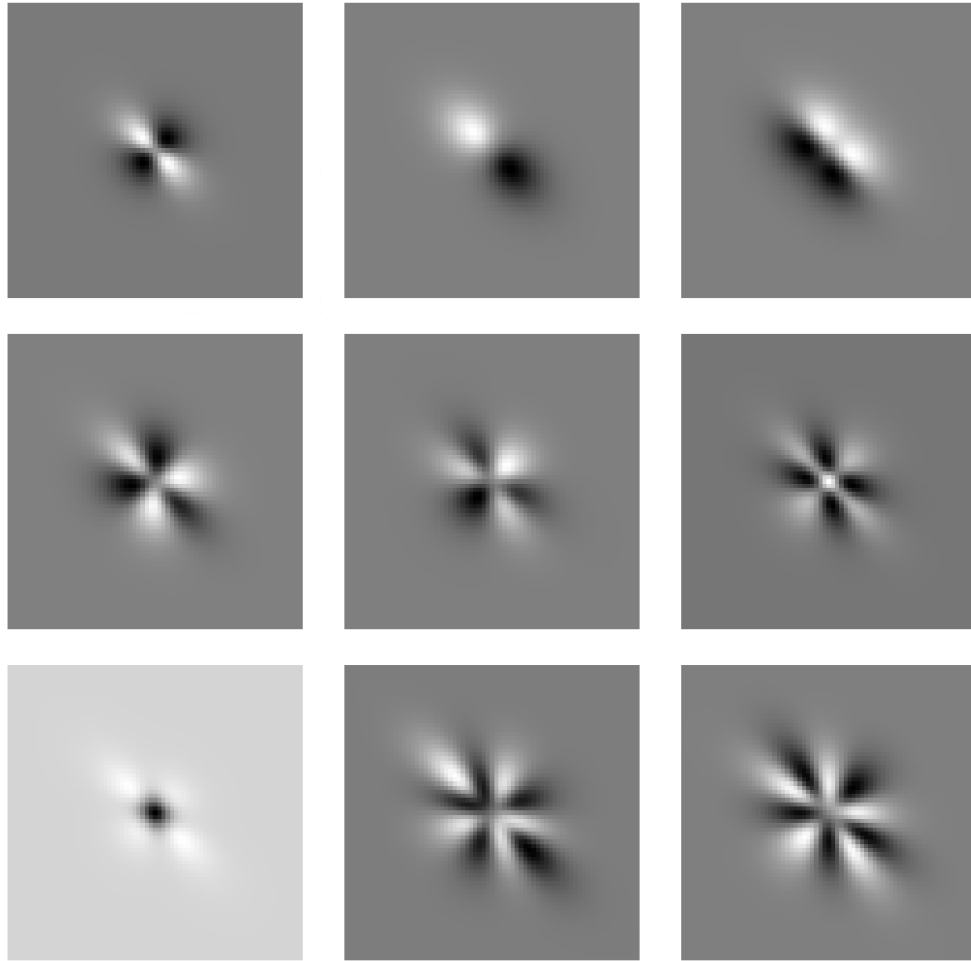

Figure 6.10: Measurement of the spin-1 ζ estimator with *PCALens*, for a sample of 10000 noise-free images of Sérsic galaxies with $R_e = 4$ pixels, $n_s = 1$, characterized by different intrinsic ellipticity and lensing deformations. *Upper panel:* Mean error on ζ_1, as a function of the true ζ_1 value, obtained when modeling the galaxies with four different number of principal components (as indicated in the legend). Errobars correspond to one standard deviation of the measured ζ_1 distribution inside each bin. *Lower panel:* Mean relative error on ζ_1, as a function of the true ζ_1 value.

6.4.2 Tests with noisy images

We can now move to investigate the performance of *PCALens* in the measurement of galaxy shapes when dealing with noisy images. For this purpose, we degraded the sets of images used in the previous section with different noise

levels, obtaining various samples of noisy images, for which we built the principal components, with *PCAlens*, following the pipeline described in section 6.2. Once the principal components have been determined, by visually inspecting the basis of each sample, we imposed the number of components to be used for the modeling equal to the order of the highest component showing features in that specific sample, and we de-noised each object. In figures 6.11 and 6.12, we show the mean residuals on δ_1 and the standard deviation of the measured distributions as a function of the true spin-3 estimator, δ_1^{true}, for 4 different samples corresponding to signal-to-noise ratios (SNR) of ~ 50, ~ 270, ~ 520 and ~ 1500, as measured by SExtractor; note that, with these SNRs, we could extract from the noise 4, 7, 10 and 17 principal components, respectively. It appears clear, from these plots, that both the mean residual as well as the dispersion of the measured δ_1 values largely increase in presence of, even low, noise. Even for the sample of images characterized by SNR~ 270, for which we could recover 7 principal components, the measured δ values are on average underestimated of $\sim 30 - 40\%$. To obtain errors under 20%, we need extremely good observing conditions (SNR > 500). Unfortunately, these SNR values do not correspond to typical values encountered in WL surveys, in fact, even the lower value, SNR ~ 50, that we used denotes definitely good, though still realistic, observing conditions in WL studies.

The flexion-induced deformations seem to be hidden very deeply in the noise, and even this new PCA approach does not completely succeed in making them emerge. Because of this reason, *PCALens* implements a different approach, which exploits a likelihood maximization algorithm, to obtain a better estimate of the principal components, as will be explained in the following section.

Expectation-maximization algorithm for PCA

The expectation-maximization algorithm for PCA, or simply EMPCA, is one of the many modifications which have been proposed over the years to overcome some of the shortcomings of the standard PCA technique. In particular, the EMPCA algorithm has the advantage of not requiring the evaluation of the data covariance matrix, and its consecutive diagonalization, to construct the principal components of a given data set, reducing in this way the computational costs, that in the case of high dimensional data sets, typical of PCA applications, are very high for the standard method. The EMPCA algorithm, exploiting a maximum likelihood approach, is able to evaluate the desired number of principal components, saving a large amount of computational time. Shortly, the idea behind is the following: given a set of n data vectors $\boldsymbol{x}^{(i)}$ of dimension m the 0th component of the sample is obtained by searching that
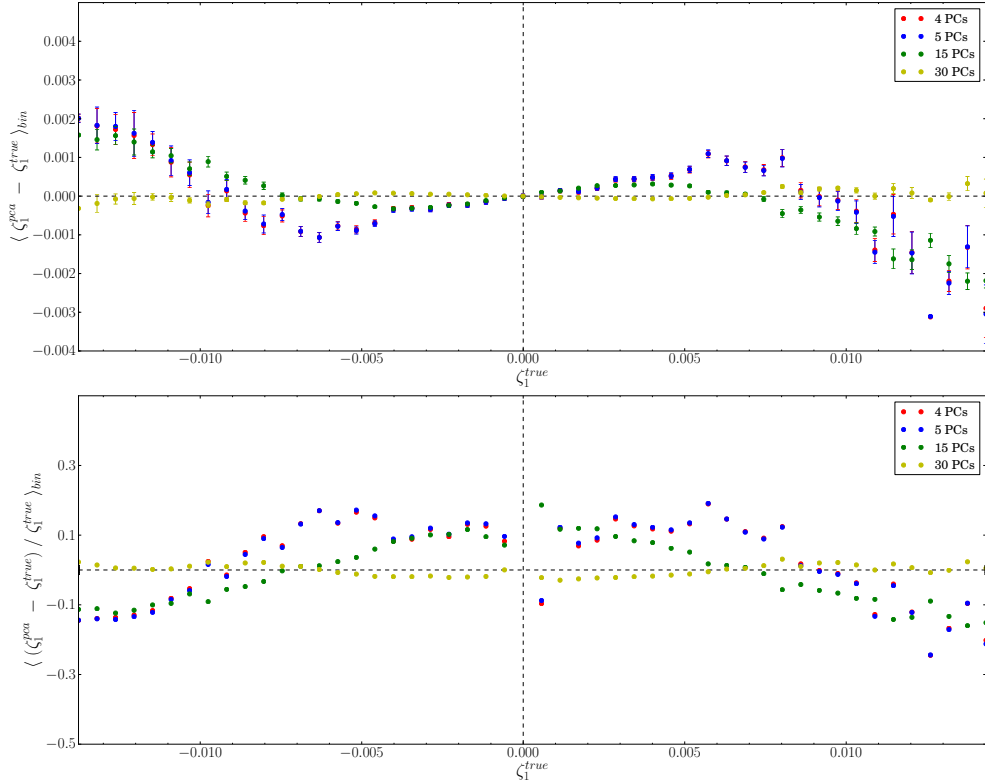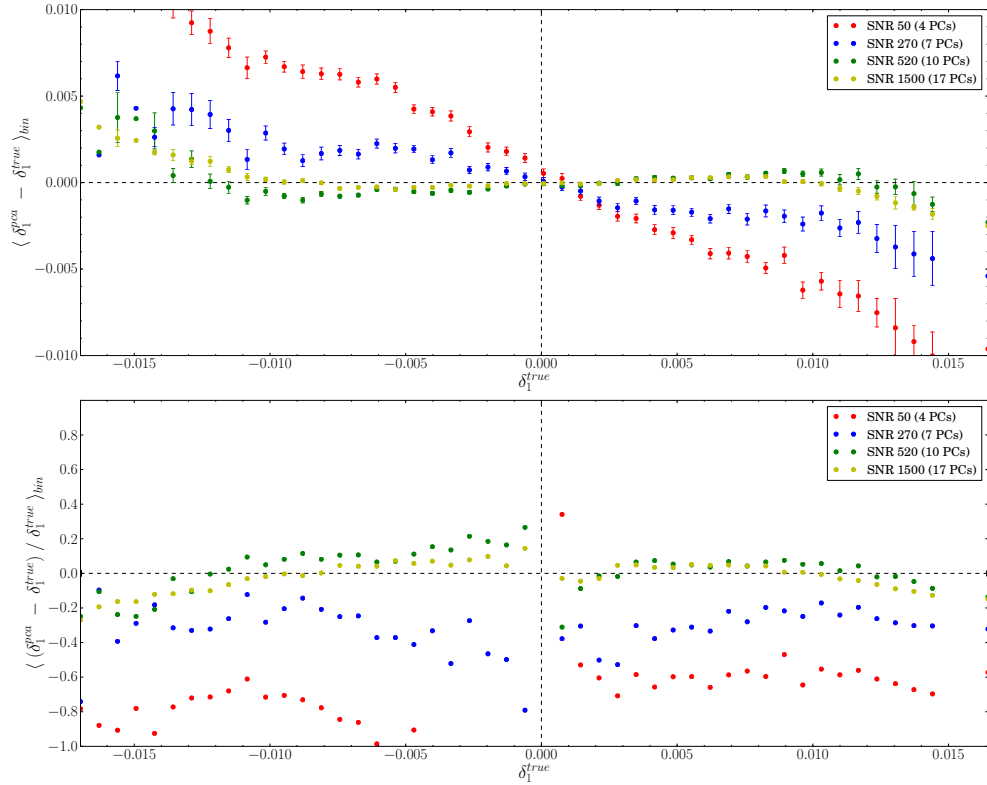
Figure 6.11: Measurement of the spin-3 δ estimator with PCALens, for a sample of 10000 noisy images of Sérsic galaxies with $R_e = 4$ pixels, $n_s = 1$, characterized by different intrinsic ellipticity and lensing deformations. Different colors refer to samples characterized by different SNR (as indicated in the legend). *Upper panel:* Mean error on δ_1, as a function of the true δ_1 value. Errobars correspond to one standard deviation of the measured δ_1 distribution inside each bin. *Lower panel:* Mean relative error on δ_1, as a function of the true δ_1 value.
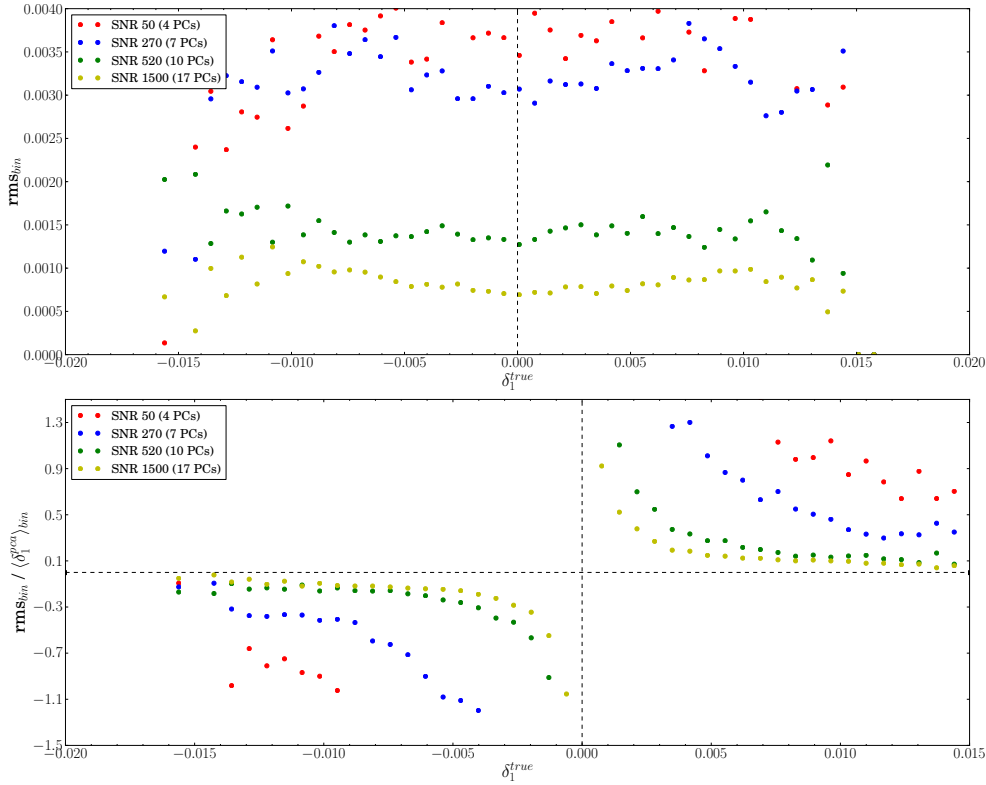
Figure 6.12: Measurement of the spin-3 δ estimator with PCALens, for a sample of 10000 noisy images of Sérsic galaxies with $R_e = 4$ pixels, $n_s = 1$, characterized by different intrinsic ellipticity and lensing deformations. Different colors refer to samples characterized by different SNR (as indicated in the legend). *Upper panel:* Root mean square of the measured δ_1 distribution inside each δ_1^{true} bin. *Lower panel:* Root mean square of the bin normalized to the mean δ value measured in that bin.

vector $\boldsymbol{e}^0$ and those coefficients $a_0^{(i)}$ which minimize the following quantity:

$$\chi^2 \equiv \sum_{i=1}^{n} \sum_{j=1}^{m} \left(x_j^{(i)} - a_0^{(i)} e_j^0 \right)^2 \; , \qquad (6.3)$$

Once this minimization has been performed, the component $\boldsymbol{e}^0$ is smoothed with a Savitzky-Golay filter[5], afterwards the data vectors are redefined by subtracting from each of them the best model that is available at this time, i.e. the model given by the only component evaluated thus far:

$$\boldsymbol{x'}^{(i)} = \boldsymbol{x}^{(i)} - a_0^{(i)} \boldsymbol{e}^0 \; . \qquad (6.4)$$

These redefined vectors $\boldsymbol{x'}$ are, then, used to identify the second component. Through an analogous minimization procedure, in the next step, the vector $\boldsymbol{e}^1$ and the coefficients $a_1^{(i)}$, which minimize the quantity:

$$\chi^2 = \sum_{i=1}^{N} \sum_{j=1}^{m} \left(x'^{(i)}_j - a_1^{(i)} e_j^1 \right)^2 \; , \qquad (6.5)$$

are identified. The process can be repeated till the number of desired principal components is obtained.

We have used this new approach to find the principal components of our data samples and present the results in figures 6.13 and 6.14. These results refer to exactly the same sets of images used in the previous test, where the standard *PCALens* pipeline was applied.

The first important fact to be noted is that, with the EMPCA version, the number of principal components which emerges from the noise, at a given SNR, is higher than in tests performed with the standard pipeline. In particular, with the EMPCA method we recover: 6, 10, 14 and 21 principal components, for the samples with SNR~50, 270, 520 and 1500, respectively, while with the standard pipeline we were obtaining: 4, 7, 10 and 17 basis vectors. A visual representation of first 5 principal components obtained for the noisiest of these samples (SNR $\sim$ 50) is given in figure 6.15, where, on the left column, we show the components obtained with the standard method and, on the right column, those obtained with the EMPCA procedure. Thanks to the smoothing procedure, the EMPCA is able to go deeper into the noise and, as can be seen in the figure, the 4th and 5th components show, in this case, much more clear features, compared to the corresponding components evaluated with the

---

[5]This smoothing procedure, based on a low degree polynomial interpolation, is introduced in order to improve the ability of the principal components to reproduce the galaxy images, based on the matter of fact that galaxies are characterized by smooth profiles.

standard method.   As we can observe in figures 6.13 and 6.14, this higher
number of components translates into smaller mean biases on the measurements
of δ_1, however the standard deviations of the measured distributions increase,
due to the inclusion of extra components and, hence, of the noise that they
carry along.

Figure 6.13: Same plot of figure 6.11, but here the principal components used
for the modeling have been estimated with the EMPCA algorithm. We refer
to figure 6.11 for a detailed description of the plot.

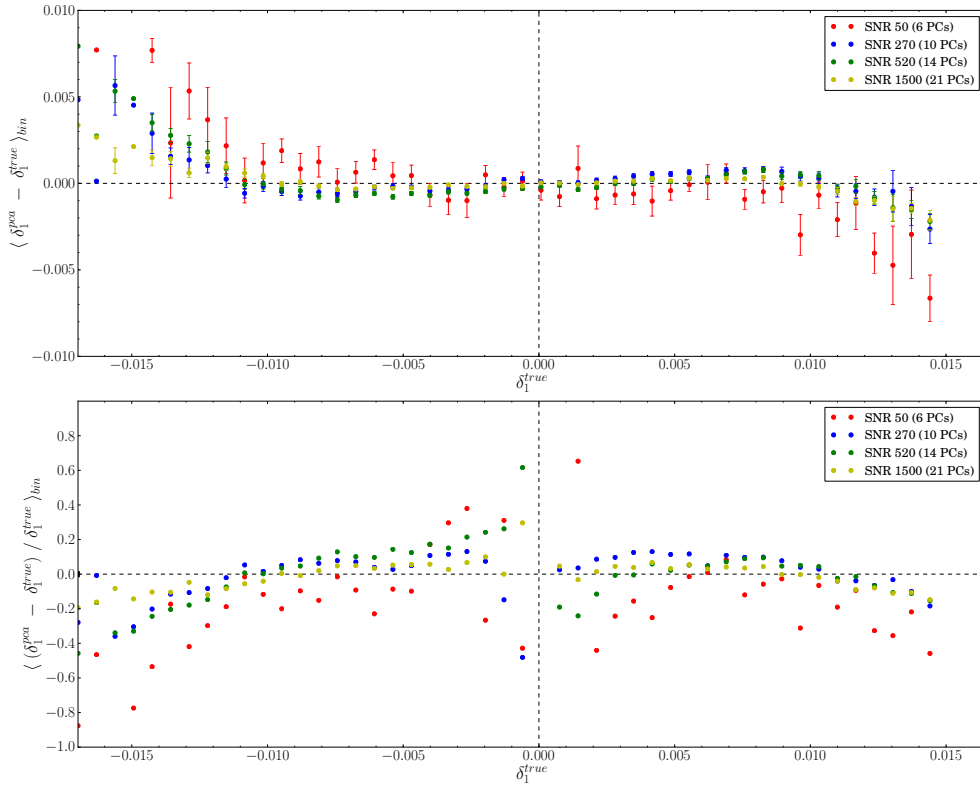Figure 6.14: Same plot of figure 6.12, but here the principal components used for the modeling have been estimated with the EMPCA algorithm. e refer to figure 6.12 for a detailed description of the plot.

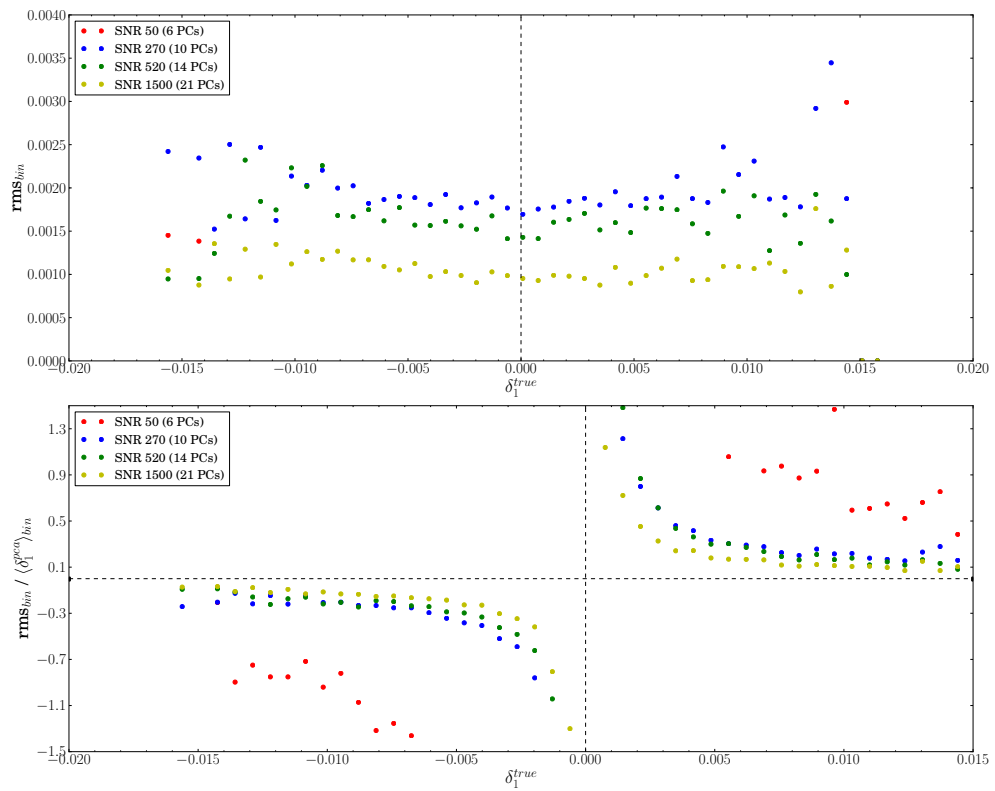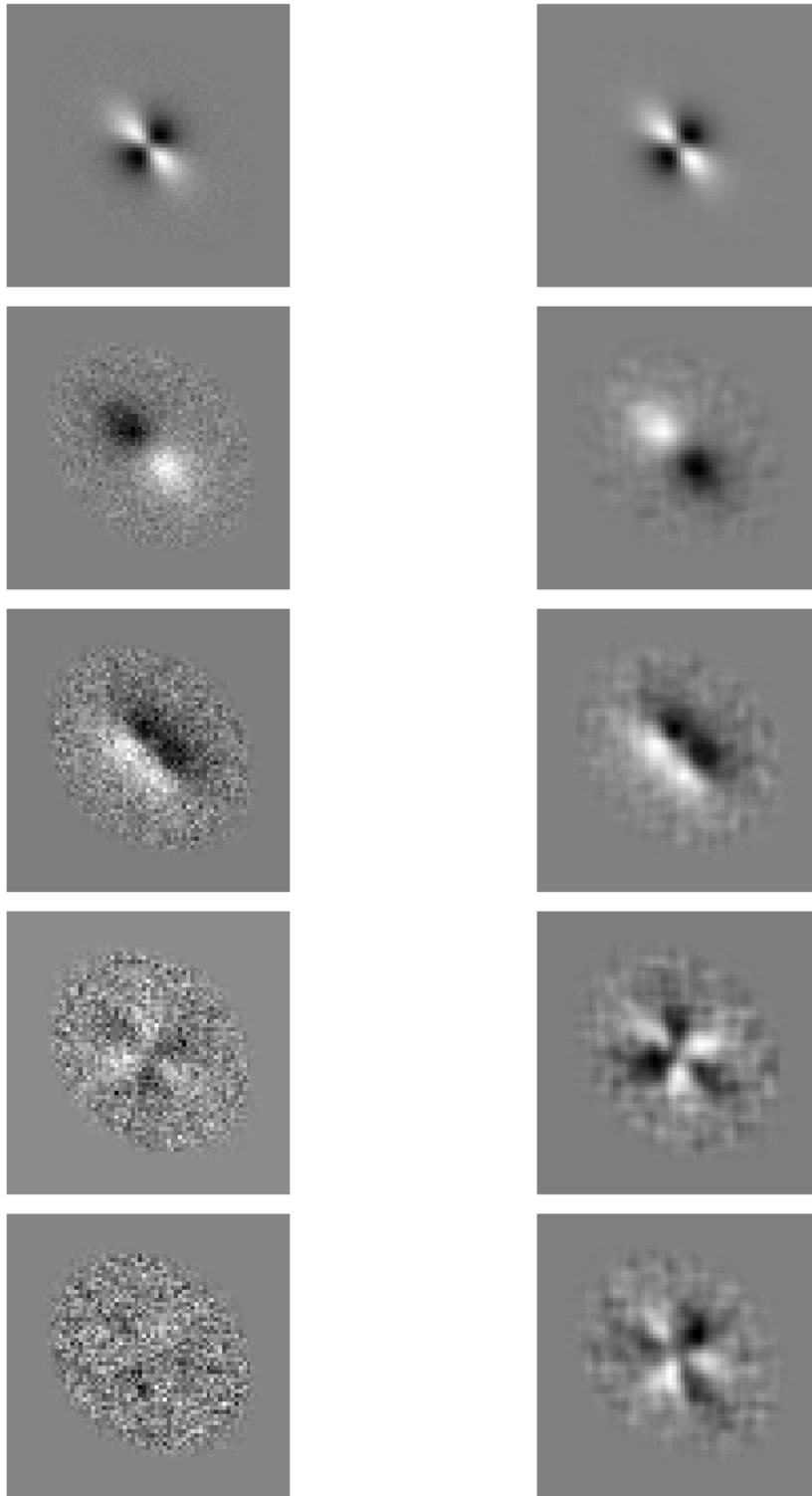Figure 6.15: First 5 PCs of a sample of 10000 galaxy images with SNR $\sim$ 50. *Left column:* PCs obtained with the standard PCA pipeline, described in section 6.2. *Right column:* PCs obtained with the EMPCA method.

6.5   Conclusions

In this chapter we have seen how the PCA technique can be used as a de-noising technique in WL applications, providing a completely non-parametric approach to galaxy modeling. In particular, using the pipeline *PCALens*, developed by Maturi (2015, in prep.), we have shown how, given a set of noisy galaxy images, it is possible to obtain for each object a noise-free model that can be used to measure the SB moments of the source and thus construct the needed lensing estimators. We showed that the method, even in its simplest version, is very competitive in measuring galaxy ellipticities. On the other side, with this method, we are still not able to measure, with high accuracy, higher order distortions in the shape of galaxies if we imagine to observe these objects in the typical observing conditions of WL surveys. At these low SNR, the components needed to recover the spin-3 features are hidden too deeply in the noise. However, with a first simple modification to the algorithm, we could already improve the number of components extracted in given noise conditions, compared to the outcome of the standard method, and for example we were able to obtain estimates of δ biased less than 20% for images having SNR $\sim$ 270, showing that margin of improvement exists. We refer to the next conclusive chapter for a summary of all the results presented in this thesis and of the conclusions we can draw from them.

Summary and conclusions

Weak gravitational lensing, i.e. the small but coherent deflection of light from distant objects due to the gravitational field of intervening matter, has developed in the past two decades into a powerful and versatile tool to constrain cosmological models, detect and study dark matter, as well as investigate the growth of structures in the universe. The power of this technique resides mostly in its ability of providing a direct measurement of the mass distribution without any need of invoking particular assumptions about the nature or dynamical state of the matter which caused the deflection.

At the first order, weak lensing is responsible for a few 10% of elliptical distortions in the shape of background sources. Standard weak lensing studies use this effect, known as gravitational shear, to explore the projected mass distribution of cosmic structures, seeking for coherent quadrupole distortions in the galaxy shapes.

Nonetheless, the last ten years have witnessed a considerable theoretical effort aimed to extend weak lensing analyses in order to include higher order distortion effects, known today as gravitational flexion. In fact, since these higher order distortions are related to the third-order derivatives of the projected gravitational potential, valuable information can be extracted from their measurement, as first shown by Goldberg and Natarajan (2002). Despite being a weaker effect compared to shear, it is believed that flexion may, nevertheless, be measured, based on the fact that galaxies typically display less intrinsic flexion-type distortions than intrinsic ellipticity, entailing that the level of noise from intrinsic shape should be lower than for the shear.

Continuing on the way opened by Goldberg and Natarajan (2002), several other studies have investigated the potential of flexion (Bacon et al., 2006; Okura et al., 2007; Leonard and King, 2010; Hawken and Bridle, 2009; Er et al., 2012). These works have shown how estimating flexion could, in principle, improve the resolution of dark matter maps, allowing to detect substructures inaccessible to shear measurements, enhance the constraints on the profiles of dark matter halos, improve the estimates of their mass and their concentration,

as well as provide tighter constraints on the halo ellipticity, finally, flexion could contribute, complementarily to shear, to investigate the evolution of structures in the universe.

Motivated by this exciting theoretical reasons, in the same years, several attempts to measure flexion in real data have been made (Goldberg and Bacon, 2005; Leonard et al., 2007; Goldberg and Leonard, 2007; Okura et al., 2008; Leonard et al., 2011; Velander et al., 2011; Cain et al., 2011). However, an unambiguous measurement of flexion has yet to be demonstrated.

The work presented in this thesis deals precisely with the problem of measuring flexion-induced distortions in realistic observational conditions. In our investigation we have applied three different methods to synthetic data in order to test their ability to infer the spin-1 and spin-3 distortions which characterize the shape of the sources in presence of flexion. The amount of such distortions is quantified, throughout the thesis, by means of the two complex estimators ζ and δ, which are defined as specific combinations of the third- and fourth-order moments of surface brightness.

The mock images used to perform our tests were created through a pipeline described in section 4.2. They consist of various sets of galaxy images, produced by taking into account all the processes that in real applications contribute to changing and degrading the shape of the observed sources, like blurring and anisotropies introduced by the PSF, pixelisation, noise degradation due to finite number of photons from source, CCD electronics or sky brightness.

The first method that we have tested is based on the DEIMOS approach developed by Melchior et al. (2011). DEIMOS is a moment-based method for weak lensing measurements which applies an exact deconvolution algorithm to correct for the PSF effect. The measurement of the SB moments on the noisy images is performed by applying a weight function whose shape is matched to the shape of the source. The change induced on the moments by this necessary weighting procedure is corrected by expressing the de-weighted moments as linear combinations of higher order weighted moments, as obtained by Taylor-expanding the inverse of the weight function to a fixed order, which represents a parameter of the method. In the standard version of DEIMOS the weight function is an elliptical Gaussian, whose centroid, size and amount of ellipticity are matched to the source through an iterative process which seeks for the WF shape which maximizes the signal-to-noise ratio. As shown in Chapter 4, if we apply the original DEIMOS algorithm to noisy images of galaxies, which are both sheared and flexed, we cannot recover the values of the ζ and δ estimators, even when working in observing conditions relatively good for weak lensing surveys (SNR $\sim$ 50, as measured with SExtractor). We ascribed this negative result to the inappropriate choice of an elliptical weight function to

measure deformations with spin-1 and spin-3.

Based on these results, we modified DEIMOS, allowing a flexed shape for the weight function and, using some simple toy models, we tested the modified pipeline. These tests, even if performed in extremely simplified situations, showed that, in order to successfully infer the estimator δ, an accurate match of the weight function shape to the source shape is fundamental. However, performing this matching turns out to be unfeasible in realistic applications, due to the higher impact of noise on the 3rd and 4th order moments compared to the second order moments used in shear measurements.

Motivated by this evidence, in Chapter 5 we developed and tested a different approach, which mostly follows the DEIMOS method, but differs from it in the de-weighting procedure. In this case, in fact, the noisy images are weighted using a circular weight function, at this point, the bias introduced on the SB moments by the weighting procedure is estimated and, before applying the deconvolution algorithm, the moments are corrected for such a bias. Two different ways to quantify the bias and correct for it have been explored.

In section 5.2, we tested a version of the pipeline in which the bias is estimated on the mean object of the galaxy population studied. We investigated both the case in which the mean object is obtained from the noise-free images of the galaxies, as well as the case in which it is obtained from the noisy counterparts, which are the only images actually accessible in real applications. In the first case, we obtained values of δ for which the residual distribution is narrower compared to the DEIMOS runs with flexed weight function. In particular, the relative errors on δ never exceed 45%. However the measured values are overall biased by 10-15%. We explained this surviving bias by considering that the corrections for the moments estimated on the mean object cannot compensate exactly for the effect of the weight function on the shape of galaxies which in general will exhibit more features and a more complex morphology compared to the mean object. When we performed the same test, using, though, for the bias estimation, the mean object obtained from the noisy images, the residual bias in the measured δ distribution significantly increased, suggesting that the noise, which survives the average process, does not allow a sufficiently precise reconstruction of the mean object shape. This has been confirmed by verifying that the residual bias decreases if we repeat the test with a higher number of galaxies, allowing a less noisy reconstruction of the mean object shape.

Thereupon, we implemented and tested a different technique, in which the bias is estimated for each single galaxy on a reconstructed noise-free model of the galaxy itself, as described in section 5.3. In particular, the noise-free models are obtained for the various objects, by modeling the galaxies with the correct profile, but assigning to them ellipticity, centroid and flexion obtained in output

from a preliminary run performed with the standard DEIMOS pipeline with circular weight function. In this case, the bias correction method performed definitely better in the measurement of δ compared to the results obtained with the DEIMOS de-weighting procedure. Indeed, we obtained, for the large majority of the objects, relative errors on δ below 30%, though a slightly biased final distribution persisted. Note, however that, as we stressed at the end of section 5.3, while performing this last test, considerable prior knowledge on the shape of the galaxies and of the PSF has been assumed, whilst this cannot be done so easily in reality. On top of that, the noise conditions considered were relatively favorable for weak lensing applications (SNR ~ 50). Loosening these assumptions would clearly reflect in a less accurate reconstruction of the objects and, thus, inevitably corrupt the final outcome.

Initially just aiming for a method able to provide a good first approximation for the shape of noisy objects to be used in the bias correction method, we undertook a different approach, which afterwards was adopted in toto. This method, developed within our group by Maturi (2015, in prep.), called *PCALens*, exploits principal component analysis to de-noise sets of images of astronomical sources. Once this has been done, the shape of each object is estimated by evaluating the SB moments on this noise-free model and, lastly, deconvolving the moments according to the same algorithm used in DEIMOS. Here no weight function is applied and the statistic of the basis used to de-noise the images reflects the statistical properties of the galaxies in the sample to be processed. In Chapter 6, we showed how this de-noising procedure is done in practice. Besides, we showed that the method is very competitive in the measurements of galaxy ellipticities. Regarding flexion, we observed that, in order to obtain values of the spin-3 distortion estimator, δ, biased in average less than 20%, the first two principal components showing features with this kind of symmetry have to be included, otherwise, even in absence of noise, the reconstructed objects will not display the details necessary to account for these higher order distortions. We tested the pipeline on sets of images characterized by different intrinsic properties of the galaxies, as well as by different levels of noise degradation. We did not observe strong evidence of systematic trends in the outcome as a function of the intrinsic properties of the galaxies. Instead, the results strongly depend on the SNR, in particular, we showed that, in order to obtain estimates of δ exhibiting mean biases below than 20%, images with SNR $\gtrsim 270$ (as measured with SExtractor) are needed. These high-SNR values, unfortunately, do not correspond to the typical values expected in standard weak lensing surveys, apart, perhaps, from a small fraction of objects in the total sample. That said, the *PCALens* approach has proved to be very versatile and easily applicable to new sets of data, since it does not require any

prior knowledge on the properties of the objects whose shape is going to be measured. Finally, it is important to note that the *PCALens* pipeline is still in its infancy, and a large margin of improvement exists, both on the side of modifying the algorithm for the principal components evaluation, as well as on the side of identifying the optimal setup for the few parameters used in the code, as well as an optimal subdivision of the data sample in order to build principal components tailored to reconstruct specific characteristics of the objects.

In conclusion, we have shown in this thesis, through a detailed investigation, that, contrary to many claims made in the last decade, a reliable estimate of the flexion-induced distortions in the images of faint background galaxies is still not achievable in the typical observational conditions of standard weak lensing surveys. A deeper understanding of the role played by pixel noise in the measurements of the flexion estimators is indispensable before the current techniques for shape measurements can be used to estimate flexion in real data. Only then, the potential of flexion will be extensively exploitable.

Bibliography

R. A. Alpher and R. C. Herman. On the Relative Abundance of the Elements. *Physical Review*, 74:1737–1742, Dec. 1948. doi: 10.1103/PhysRev.74.1737.

R. Andrae, P. Melchior, and K. Jahnke. Quantifying galaxy shapes: sérsiclets and beyond. *Monthly Notices of the RAS*, 417:2465–2477, Nov. 2011. doi: 10.1111/j.1365-2966.2011.19348.x.

D. J. Bacon, A. R. Refregier, and R. S. Ellis. Detection of weak gravitational lensing by large-scale structure. *Monthly Notices of the RAS*, 318:625–640, Oct. 2000a. doi: 10.1046/j.1365-8711.2000.03851.x.

D. J. Bacon, A. R. Refregier, and R. S. Ellis. Detection of weak gravitational lensing by large-scale structure. *Monthly Notices of the RAS*, 318:625–640, Oct. 2000b. doi: 10.1046/j.1365-8711.2000.03851.x.

D. J. Bacon, D. M. Goldberg, B. T. P. Rowe, and A. N. Taylor. Weak gravitational flexion. *Monthly Notices of the RAS*, 365:414–428, Jan. 2006. doi: 10.1111/j.1365-2966.2005.09624.x.

D. J. Bacon, A. Amara, and J. I. Read. Measuring dark matter substructure with galaxy-galaxy flexion statistics. *Monthly Notices of the RAS*, 409:389–395, Nov. 2010. doi: 10.1111/j.1365-2966.2010.17316.x.

M. Bartelmann. Cluster mass estimates from weak lensing. *Astronomy and Astrophysics*, 303:643, Nov. 1995.

M. Bartelmann. TOPICAL REVIEW Gravitational lensing. *Classical and Quantum Gravity*, 27(23):233001, Dec. 2010. doi: 10.1088/0264-9381/27/23/233001.

M. Bartelmann and R. Narayan. The Lens Parallax Method: Determining Redshifts of Faint Blue Galaxies through Gravitational Lensing. *Astrophysical Journal*, 451:60, Sept. 1995. doi: 10.1086/176200.

M. Bartelmann and P. Schneider. Weak gravitational lensing. *Physics Reports*, 340:291–472, Jan. 2001. doi: 10.1016/S0370-1573(00)00082-X.

M. Bartelmann, R. Narayan, S. Seitz, and P. Schneider. Maximum-likelihood Cluster Reconstruction. *Astrophysical Journal, Letters*, 464:L115, June 1996. doi: 10.1086/310114.

G. M. Bernstein and R. Armstrong. Bayesian lensing shear measurement. *Monthly Notices of the RAS*, 438:1880–1893, Feb. 2014. doi: 10.1093/mnras/stt2326.

G. M. Bernstein and M. Jarvis. Shapes and Shears, Stars and Smears: Optimal Measurements for Weak Lensing. *Astronomical Journal*, 123:583–618, Feb. 2002. doi: 10.1086/338085.

E. Bertin and S. Arnouts. SExtractor: Software for source extraction. *Astronomy and Astrophysics, Supplement*, 117:393–404, June 1996. doi: 10.1051/aas:1996164.

T. G. Brainerd, R. D. Blandford, and I. Smail. Weak Gravitational Lensing by Galaxies. *Astrophysical Journal*, 466:623, Aug. 1996. doi: 10.1086/177537.

S. Bridle, J. Shawe-Taylor, A. Amara, D. Applegate, J. S. T. Balan, Berge, G. Bernstein, H. Dahle, T. Erben, M. Gill, A. Heavens, C. Heymans, F. W. High, H. Hoekstra, M. Jarvis, D. Kirk, T. Kitching, J.-P. Kneib, K. Kuijken, D. Lagatutta, R. Mandelbaum, R. Massey, Y. Mellier, B. Moghaddam, Y. Moudden, R. Nakajima, S. Paulin-Henriksson, S. Pires, A. Rassat, A. Refregier, J. Rhodes, T. Schrabback, E. Semboloni, M. Shmakova, L. van Waerbeke, D. Witherick, L. Voigt, and D. Wittman. Handbook for the GREAT08 Challenge: An image analysis competition for cosmological lensing. *Annals of Applied Statistics*, 3:6–37, 2009. doi: 10.1214/08-AOAS222.

S. Bridle, S. T. Balan, M. Bethge, M. Gentile, S. Harmeling, C. Heymans, M. Hirsch, R. Hosseini, M. Jarvis, D. Kirk, T. Kitching, K. Kuijken, A. Lewis, S. Paulin-Henriksson, B. Schölkopf, M. Velander, L. Voigt, D. Witherick, A. Amara, G. Bernstein, F. Courbin, M. Gill, A. Heavens, R. Mandelbaum, R. Massey, B. Moghaddam, A. Rassat, A. Réfrégier, J. Rhodes, T. Schrabback, J. Shawe-Taylor, M. Shmakova, L. van Waerbeke, and D. Wittman. Results of the GREAT08 Challenge: an image analysis competition for cosmological lensing. *Monthly Notices of the RAS*, 405:2044–2061, July 2010. doi: 10.1111/j.1365-2966.2010.16598.x.

S. L. Bridle, J.-P. Kneib, S. Bardeau, and S. F. Gull. Bayesian Galaxy Shape Estimation. In P. Natarajan, editor, *The Shapes of Galaxies and their Dark Halos*, pages 38–46, Mar. 2002.

T. J. Broadhurst, A. N. Taylor, and J. A. Peacock. Mapping cluster mass distributions via gravitational lensing of background galaxies. *Astrophysical Journal*, 438:49–61, Jan. 1995. doi: 10.1086/175053.

S. Burles, K. M. Nollett, J. W. Truran, and M. S. Turner. Sharpening the Predictions of Big-Bang Nucleosynthesis. *Physical Review Letters*, 82:4176–4179, May 1999a. doi: 10.1103/PhysRevLett.82.4176.

S. Burles, K. M. Nollett, and M. S. Turner. Big-Bang Nucleosynthesis: Linking Inner Space and Outer Space. *ArXiv Astrophysics e-prints*, Mar. 1999b.

B. Cain, P. L. Schechter, and M. W. Bautz. Measuring Gravitational Lensing Flexion in A1689 Using an Analytic Image Model. *Astrophysical Journal*, 736:43, July 2011. doi: 10.1088/0004-637X/736/1/43.

M. Capaccioli. Photometry of early-type galaxies and the R exp 1/4 law. In H. G. Corwin, Jr. and L. Bottinelli, editors, *World of Galaxies (Le Monde des Galaxies)*, pages 208–227, 1989.

C. Chang, M. Jarvis, B. Jain, S. M. Kahn, D. Kirkby, A. Connolly, S. Krughoff, E.-H. Peng, and J. R. Peterson. The effective number density of galaxies for weak lensing measurements in the LSST project. *Monthly Notices of the RAS*, 434:2121–2135, Sept. 2013. doi: 10.1093/mnras/stt1156.

P. Coles and F. Lucchin. *Cosmology: The Origin and Evolution of Cosmic Structure, Second Edition*. July 2002.

M. Colless, G. Dalton, S. Maddox, W. Sutherland, P. Norberg, S. Cole, J. Bland-Hawthorn, T. Bridges, R. Cannon, C. Collins, W. Couch, N. Cross, K. Deeley, R. De Propris, S. P. Driver, G. Efstathiou, R. S. Ellis, C. S. Frenk, K. Glazebrook, C. Jackson, O. Lahav, I. Lewis, S. Lumsden, D. Madgwick, J. A. Peacock, B. A. Peterson, I. Price, M. Seaborne, and K. Taylor. The 2dF Galaxy Redshift Survey: spectra and redshifts. *Monthly Notices of the RAS*, 328:1039–1063, Dec. 2001. doi: 10.1046/j.1365-8711.2001.04902.x.

S. Dodelson. *Modern cosmology*. 2003.

A. Einstein. Die Grundlage der allgemeinen Relativitätstheorie. *Annalen der Physik*, 354:769–822, 1916. doi: 10.1002/andp.19163540702.

X. Er and M. Bartelmann. Estimation of halo ellipticity using spin-3 flexion. *Monthly Notices of the RAS*, 428:103–108, Jan. 2013. doi: 10.1093/mnras/sts003.

X. Er, I. Tereno, and S. Mao. Measurement of halo properties with weak lensing shear and flexion. *Monthly Notices of the RAS*, 421:1443–1449, Apr. 2012. doi: 10.1111/j.1365-2966.2012.20408.x.

T. Erben, L. Van Waerbeke, E. Bertin, Y. Mellier, and P. Schneider. How accurately can we measure weak gravitational shear? *Astronomy and Astrophysics*, 366:717–735, Feb. 2001. doi: 10.1051/0004-6361:20010013.

E. E. Falco, M. V. Gorenstein, and I. I. Shapiro. On model-dependent bounds on H(0) from gravitational images Application of Q0957 + 561A,B. *Astrophysical Journal, Letters*, 289:L1–L4, Feb. 1985. doi: 10.1086/184422.

J. Flusser and T. Suk. Degraded image analysis: An invariant approach. *IEEE Transactions on Pattern Analysis and Machine Intelligence*, 20(6):590–603, 1998. ISSN 0162-8828. doi: http://doi.ieeecomputersociety.org/10.1109/34.683773.

B. Fort, J. L. Prieur, G. Mathez, Y. Mellier, and G. Soucail. Faint distorted structures in the core of A 370 - Are they gravitationally lensed galaxies at Z about 1? *Astronomy and Astrophysics*, 200:L17–L20, July 1988.

D. M. Goldberg and D. J. Bacon. Galaxy-Galaxy Flexion: Weak Lensing to Second Order. *Astrophysical Journal*, 619:741–748, Feb. 2005. doi: 10.1086/426782.

D. M. Goldberg and A. Leonard. Measuring Flexion. *Astrophysical Journal*, 660:1003–1015, May 2007. doi: 10.1086/513137.

D. M. Goldberg and P. Natarajan. The Galaxy Octopole Moment as a Probe of Weak-Lensing Shear Fields. *Astrophysical Journal*, 564:65–72, Jan. 2002. doi: 10.1086/324202.

A. J. Hawken and S. L. Bridle. Gravitational flexion by elliptical dark matter haloes. *Monthly Notices of the RAS*, 400:1132–1138, Dec. 2009. doi: 10.1111/j.1365-2966.2009.15539.x.

C. Heymans, M. L. Brown, M. Barden, J. A. R. Caldwell, K. Jahnke, C. Y. Peng, H.-W. Rix, A. Taylor, S. V. W. Beckwith, E. F. Bell, A. Borch, B. Häußler, S. Jogee, D. H. McIntosh, K. Meisenheimer, S. F. Sánchez, R. Somerville, L. Wisotzki, and C. Wolf. Cosmological weak lensing with

the HST GEMS survey. *Monthly Notices of the RAS*, 361:160–176, July 2005. doi: 10.1111/j.1365-2966.2005.09152.x.

C. Heymans, L. Van Waerbeke, D. Bacon, J. Berge, G. Bernstein, E. Bertin, S. Bridle, M. L. Brown, D. Clowe, H. Dahle, T. Erben, M. Gray, M. Hetterscheidt, H. Hoekstra, P. Hudelot, M. Jarvis, K. Kuijken, V. Margoniner, R. Massey, Y. Mellier, R. Nakajima, A. Refregier, J. Rhodes, T. Schrabback, and D. Wittman. The Shear Testing Programme - I. Weak lensing analysis of simulated ground-based observations. *Monthly Notices of the RAS*, 368: 1323–1339, May 2006. doi: 10.1111/j.1365-2966.2006.10198.x.

H. Hoekstra, M. Franx, K. Kuijken, and G. Squires. Weak Lensing Analysis of CL 1358+62 Using Hubble Space Telescope Observations. *Astrophysical Journal*, 504:636–660, Sept. 1998. doi: 10.1086/306102.

E. Hubble. A Relation between Distance and Radial Velocity among Extra-Galactic Nebulae. *Proceedings of the National Academy of Science*, 15:168–173, Mar. 1929. doi: 10.1073/pnas.15.3.168.

N. Kaiser. Weak gravitational lensing of distant galaxies. *Astrophysical Journal*, 388:272–286, Apr. 1992. doi: 10.1086/171151.

N. Kaiser and G. Squires. Mapping the dark matter with weak gravitational lensing. *Astrophysical Journal*, 404:441–450, Feb. 1993. doi: 10.1086/172297.

N. Kaiser, G. Squires, and T. Broadhurst. A Method for Weak Lensing Observations. *Astrophysical Journal*, 449:460, Aug. 1995a. doi: 10.1086/176071.

N. Kaiser, G. Squires, G. Fahlman, D. Woods, and T. Broadhurst. Recent Developments in Weak Lensing. In S. J. Maddox and A. Aragon-Salamanca, editors, *Wide Field Spectroscopy and the Distant Universe*, page 246, 1995b.

N. Kaiser, G. Wilson, and G. A. Luppino. Large-Scale Cosmic Shear Measurements. *ArXiv Astrophysics e-prints*, Mar. 2000.

M. Kilbinger. Cosmology with cosmic shear observations: a review. *Reports on Progress in Physics*, 78(8):086901, July 2015. doi: 10.1088/0034-4885/78/8/086901.

T. D. Kitching, L. Miller, C. E. Heymans, L. van Waerbeke, and A. F. Heavens. Bayesian galaxy shape measurement for weak lensing surveys - II. Application to simulations, Oct. 2008.

A. Klypin, A. V. Kravtsov, O. Valenzuela, and F. Prada. Where Are the Missing Galactic Satellites? *Astrophysical Journal*, 522:82–92, Sept. 1999. doi: 10.1086/307643.

K. Kuijken. Weak weak lensing: correcting weak shear measurements accurately for PSF anisotropy. *Astronomy and Astrophysics*, 352:355–362, Dec. 1999.

K. Kuijken. Shears from shapelets. *Astronomy and Astrophysics*, 456:827–838, Sept. 2006. doi: 10.1051/0004-6361:20054794.

A. Leonard and L. J. King. A new tool to determine masses and mass profiles using gravitational flexion. *Monthly Notices of the RAS*, 405:1854–1866, July 2010. doi: 10.1111/j.1365-2966.2010.16573.x.

A. Leonard, D. M. Goldberg, J. L. Haaga, and R. Massey. Gravitational Shear, Flexion, and Strong Lensing in Abell 1689. *Astrophysical Journal*, 666:51–63, Sept. 2007. doi: 10.1086/520109.

A. Leonard, L. J. King, and S. M. Wilkins. Detecting mass substructure in galaxy clusters: an aperture mass statistic for gravitational flexion. *Monthly Notices of the RAS*, 395:1438–1448, May 2009. doi: 10.1111/j.1365-2966.2009.14546.x.

A. Leonard, L. J. King, and D. M. Goldberg. New constraints on the complex mass substructure in Abell 1689 from gravitational flexion. *Monthly Notices of the RAS*, 413:789–804, May 2011. doi: 10.1111/j.1365-2966.2010.18171.x.

D. N. Limber. The Analysis of Counts of the Extragalactic Nebulae in Terms of a Fluctuating Density Field. *Astrophysical Journal*, 117:134, Jan. 1953. doi: 10.1086/145672.

M. Lombardi and G. Bertin. Improving the accuracy of mass reconstructions from weak lensing: from the shear map to the mass distribution. *Astronomy and Astrophysics*, 335:1–11, July 1998.

M. Lombardi and G. Bertin. A fast direct method of mass reconstruction for gravitational lenses. *Astronomy and Astrophysics*, 348:38–42, Aug. 1999.

G. A. Luppino and N. Kaiser. Detection of Weak Lensing by a Cluster of Galaxies at z = 0.83. *Astrophysical Journal*, 475:20–28, Jan. 1997.

R. Lynds and V. Petrosian. Giant Luminous Arcs in Galaxy Clusters. *Bulletin of the American Astronomical Society*, 18:1014, 1986.

R. Mandelbaum, B. Rowe, R. Armstrong, D. Bard, E. Bertin, J. Bosch, D. Boutigny, F. Courbin, W. A. Dawson, A. Donnarumma, I. Fenech Conti, R. Gavazzi, M. Gentile, M. S. S. Gill, D. W. Hogg, E. M. Huff, M. J. Jee, T. Kacprzak, M. Kilbinger, T. Kuntzer, D. Lang, W. Luo, M. C. March, P. J. Marshall, J. E. Meyers, L. Miller, H. Miyatake, R. Nakajima, F. M. Ngolé Mboula, G. Nurbaeva, Y. Okura, S. Paulin-Henriksson, J. Rhodes, M. D. Schneider, H. Shan, E. S. Sheldon, M. Simet, J.-L. Starck, F. Sureau, M. Tewes, K. Zarb Adami, J. Zhang, and J. Zuntz. GREAT3 results - I. Systematic errors in shear estimation and the impact of real galaxy morphology. *Monthly Notices of the RAS*, 450:2963–3007, July 2015. doi: 10.1093/mnras/stv781.

R. Massey, C. Heymans, J. Bergé, G. Bernstein, S. Bridle, D. Clowe, H. Dahle, R. Ellis, T. Erben, M. Hetterscheidt, F. W. High, C. Hirata, H. Hoekstra, P. Hudelot, M. Jarvis, D. Johnston, K. Kuijken, V. Margoniner, R. Mandelbaum, Y. Mellier, R. Nakajima, S. Paulin-Henriksson, M. Peeples, C. Roat, A. Refregier, J. Rhodes, T. Schrabback, M. Schirmer, U. Seljak, E. Semboloni, and L. van Waerbeke. The Shear Testing Programme 2: Factors affecting high-precision weak-lensing analyses. *Monthly Notices of the RAS*, 376:13–38, Mar. 2007a. doi: 10.1111/j.1365-2966.2006.11315.x.

R. Massey, B. Rowe, A. Refregier, D. J. Bacon, and J. Bergé. Weak gravitational shear and flexion with polar shapelets. *Monthly Notices of the RAS*, 380:229–245, Sept. 2007b. doi: 10.1111/j.1365-2966.2007.12072.x.

M. Maturi. Modelling the image of galaxies with PCALens. 2015, in prep.

P. Melchior, M. Viola, B. M. Schäfer, and M. Bartelmann. Weak gravitational lensing with DEIMOS. *Monthly Notices of the RAS*, 412:1552–1558, Apr. 2011. doi: 10.1111/j.1365-2966.2010.17875.x.

L. Miller, T. D. Kitching, C. Heymans, A. F. Heavens, and L. van Waerbeke. Bayesian galaxy shape measurement for weak lensing surveys - I. Methodology and a fast-fitting algorithm. *Monthly Notices of the RAS*, 382:315–324, Nov. 2007. doi: 10.1111/j.1365-2966.2007.12363.x.

A. F. J. Moffat. A Theoretical Investigation of Focal Stellar Images in the Photographic Emulsion and Application to Photographic Photometry. *Astronomy and Astrophysics*, 3:455, Dec. 1969.

B. Moore, S. Ghigna, F. Governato, G. Lake, T. Quinn, J. Stadel, and P. Tozzi. Dark Matter Substructure within Galactic Halos. *Astrophysical Journal, Letters*, 524:L19–L22, Oct. 1999. doi: 10.1086/312287.

R. Nakajima and G. Bernstein. Shear Recovery Accuracy in Weak-Lensing Analysis with the Elliptical Gauss-Laguerre Method. *Astronomical Journal*, 133:1763–1779, Apr. 2007. doi: 10.1086/511957.

R. Narayan and M. Bartelmann. Lectures on Gravitational Lensing. *ArXiv Astrophysics e-prints*, June 1996.

W. Ngan, L. van Waerbeke, A. Mahdavi, C. Heymans, and H. Hoekstra. Sérsiclets - a matched filter extension of Shapelets for weak lensing studies. *Monthly Notices of the RAS*, 396:1211–1216, June 2009. doi: 10.1111/j.1365-2966.2009.14787.x.

Y. Okura, K. Umetsu, and T. Futamase. A New Measure for Weak-Lensing Flexion. *Astrophysical Journal*, 660:995–1002, May 2007. doi: 10.1086/513135.

Y. Okura, K. Umetsu, and T. Futamase. A Method for Weak-Lensing Flexion Analysis by the HOLICs Moment Approach. *Astrophysical Journal*, 680: 1–16, June 2008. doi: 10.1086/587676.

B. Paczyński. Giant luminous arcs discovered in two clusters of galaxies. *Nature*, 325:572–573, Feb. 1987. doi: 10.1038/325572a0.

T. Padmanabhan. Books-Received - Structure Formation in the Universe. *Journal of the British Astronomical Association*, 103:193, Aug. 1993.

J. A. Peacock. *Cosmological Physics*. Jan. 1999.

A. A. Penzias and R. W. Wilson. A Measurement of Excess Antenna Temperature at 4080 Mc/s. *Astrophysical Journal*, 142:419–421, July 1965. doi: 10.1086/148307.

S. Perlmutter and B. P. Schmidt. Measuring Cosmology with Supernovae. In K. Weiler, editor, *Supernovae and Gamma-Ray Bursters*, volume 598 of *Lecture Notes in Physics, Berlin Springer Verlag*, pages 195–217, 2003.

S. Perlmutter, G. Aldering, G. Goldhaber, R. A. Knop, P. Nugent, P. G. Castro, S. Deustua, S. Fabbro, A. Goobar, D. E. Groom, I. M. Hook, A. G. Kim, M. Y. Kim, J. C. Lee, N. J. Nunes, R. Pain, C. R. Pennypacker, R. Quimby, C. Lidman, R. S. Ellis, M. Irwin, R. G. McMahon, P. Ruiz-Lapuente, N. Walton, B. Schaefer, B. J. Boyle, A. V. Filippenko, T. Matheson, A. S. Fruchter, N. Panagia, H. J. M. Newberg, W. J. Couch, and T. S. C. Project. Measurements of Ω and Λ from 42 High-Redshift Supernovae. *Astrophysical Journal*, 517:565–586, June 1999. doi: 10.1086/307221.

Planck Collaboration, P. A. R. Ade, N. Aghanim, M. Arnaud, M. Ashdown, J. Aumont, C. Baccigalupi, A. J. Banday, R. B. Barreiro, J. G. Bartlett, and et al. Planck 2015 results. XIII. Cosmological parameters. *ArXiv e-prints*, Feb. 2015.

P. Prugniel and F. Simien. The fundamental plane of early-type galaxies: non-homology of the spatial structure. *Astronomy and Astrophysics*, 321:111–122, May 1997.

A. Refregier. Shapelets - I. A method for image analysis. *Monthly Notices of the RAS*, 338:35–47, Jan. 2003a. doi: 10.1046/j.1365-8711.2003.05901.x.

A. Refregier. Weak Gravitational Lensing by Large-Scale Structure. *Annual Review of Astronomy & Astrophysics*, 41:645–668, 2003b. doi: 10.1146/annurev.astro.41.111302.102207.

A. Refregier and D. Bacon. Shapelets - II. A method for weak lensing measurements. *Monthly Notices of the RAS*, 338:48–56, Jan. 2003. doi: 10.1046/j.1365-8711.2003.05902.x.

A. G. Riess, A. V. Filippenko, P. Challis, A. Clocchiatti, A. Diercks, P. M. Garnavich, R. L. Gilliland, C. J. Hogan, S. Jha, R. P. Kirshner, B. Leibundgut, M. M. Phillips, D. Reiss, B. P. Schmidt, R. A. Schommer, R. C. Smith, J. Spyromilio, C. Stubbs, N. B. Suntzeff, and J. Tonry. Observational Evidence from Supernovae for an Accelerating Universe and a Cosmological Constant. *Astronomical Journal*, 116:1009–1038, Sept. 1998. doi: 10.1086/300499.

B. Rowe, D. Bacon, R. Massey, C. Heymans, B. Häußler, A. Taylor, J. Rhodes, and Y. Mellier. Flexion measurement in simulations of Hubble Space Telescope data. *Monthly Notices of the RAS*, 435:822–844, Oct. 2013. doi: 10.1093/mnras/stt1353.

P. Schneider. Cluster lens reconstruction using only observed local data. *Astronomy and Astrophysics*, 302:639, Oct. 1995.

P. Schneider. Weak Gravitational Lensing. *ArXiv Astrophysics e-prints*, Sept. 2005.

P. Schneider. *Extragalactic Astronomy and Cosmology: An Introduction.* 2015. doi: 10.1007/978-3-642-54083-7.

P. Schneider and C. Seitz. Steps towards nonlinear cluster inversion through gravitational distortions. 1: Basic considerations and circular clusters. *Astronomy and Astrophysics*, 294:411–431, Feb. 1995.

T. Schrabback, T. Erben, P. Simon, J.-M. Miralles, P. Schneider, C. Heymans, T. Eifler, R. A. E. Fosbury, W. Freudling, M. Hetterscheidt, H. Hildebrandt, and N. Pirzkal. Cosmic shear analysis of archival HST/ACS data. I. Comparison of early ACS pure parallel data to the HST/GEMS survey. *Astronomy and Astrophysics*, 468:823–847, June 2007. doi: 10.1051/0004-6361:20065898.

C. Seitz and P. Schneider. Steps towards nonlinear cluster inversion through gravitational distortions. III. Including a redshift distribution of the sources. *Astronomy and Astrophysics*, 318:687–699, Feb. 1997.

S. Seitz and P. Schneider. Cluster lens reconstruction using only observed local data: an improved finite-field inversion technique. *Astronomy and Astrophysics*, 305:383, Jan. 1996.

J. L. Sérsic. Influence of the atmospheric and instrumental dispersion on the brightness distribution in a galaxy. *Boletin de la Asociacion Argentina de Astronomia La Plata Argentina*, 6:41, 1963.

J. L. Sérsic. *Atlas de galaxias australes*. 1968.

V. M. Slipher. Radial velocity observations of spiral nebulae. *The Observatory*, 40:304–306, Aug. 1917.

G. Soucail, B. Fort, Y. Mellier, and J. P. Picat. A blue ring-like structure, in the center of the A 370 cluster of galaxies. *Astronomy and Astrophysics*, 172: L14–L16, Jan. 1987.

V. Springel, S. D. M. White, A. Jenkins, C. S. Frenk, N. Yoshida, L. Gao, J. Navarro, R. Thacker, D. Croton, J. Helly, J. A. Peacock, S. Cole, P. Thomas, H. Couchman, A. Evrard, J. Colberg, and F. Pearce. Simulations of the formation, evolution and clustering of galaxies and quasars. *Nature*, 435:629–636, June 2005. doi: 10.1038/nature03597.

G. Squires and N. Kaiser. Unbiased Cluster Lens Reconstruction. *Astrophysical Journal*, 473:65, Dec. 1996. doi: 10.1086/178127.

K. Subramanian and S. A. Cowling. On local conditions for multiple imaging by bounded, smooth gravitational lenses. *Monthly Notices of the RAS*, 219: 333–346, Mar. 1986.

I. Trujillo, J. A. L. Aguerri, J. Cepa, and C. M. Gutiérrez. The effects of seeing on Sérsic profiles - II. The Moffat PSF. *Monthly Notices of the RAS*, 328: 977–985, Dec. 2001. doi: 10.1046/j.1365-8711.2001.04937.x.

J. A. Tyson and P. Seitzer. A deep CCD survey of 12 high-latitude fields. *Astrophysical Journal*, 335:552–583, Dec. 1988. doi: 10.1086/166949.

J. A. Tyson, F. Valdes, J. F. Jarvis, and A. P. Mills, Jr. Galaxy mass distribution from gravitational light deflection. *Astrophysical Journal, Letters*, 281: L59–L62, June 1984. doi: 10.1086/184285.

J. A. Tyson, R. A. Wenk, and F. Valdes. Detection of systematic gravitational lens galaxy image alignments - Mapping dark matter in galaxy clusters. *Astrophysical Journal, Letters*, 349:L1–L4, Jan. 1990. doi: 10.1086/185636.

L. Van Waerbeke, Y. Mellier, T. Erben, J. C. Cuillandre, F. Bernardeau, R. Maoli, E. Bertin, H. J. McCracken, O. Le Fèvre, B. Fort, M. Dantel-Fort, B. Jain, and P. Schneider. Detection of correlated galaxy ellipticities from CFHT data: first evidence for gravitational lensing by large-scale structures. *Astronomy and Astrophysics*, 358:30–44, June 2000.

M. Velander, K. Kuijken, and T. Schrabback. Probing galaxy dark matter haloes in COSMOS with weak lensing flexion. *Monthly Notices of the RAS*, 412:2665–2677, Apr. 2011. doi: 10.1111/j.1365-2966.2010.18085.x.

M. Viola, P. Melchior, and M. Bartelmann. Shear-flexion cross-talk in weak-lensing measurements. *Monthly Notices of the RAS*, 419:2215–2225, Jan. 2012. doi: 10.1111/j.1365-2966.2011.19872.x.

L. M. Voigt and S. L. Bridle. Limitations of model-fitting methods for lensing shear estimation. *Monthly Notices of the RAS*, 404:458–467, May 2010. doi: 10.1111/j.1365-2966.2010.16300.x.

D. Walsh, R. F. Carswell, and R. J. Weymann. 0957 + 561 A, B - Twin quasistellar objects or gravitational lens. *Nature*, 279:381–384, May 1979. doi: 10.1038/279381a0.

D. M. Wittman, J. A. Tyson, D. Kirkman, I. Dell'Antonio, and G. Bernstein. Detection of weak gravitational lensing distortions of distant galaxies by cosmic dark matter at large scales. *Nature*, 405:143–148, May 2000.

J. Zhang, W. Luo, and S. Foucaud. Accurate shear measurement with faint sources. *Journal of Cosmology and Astroparticle Physics*, 1:024, Jan. 2015. doi: 10.1088/1475-7516/2015/01/024.

Acknowledgements

It has been a long journey, but here I am, about to cross the finishing line. If I made to the end, it is certainly thanks to many people that have accompanied me, guided me, and sometimes even pushed me through these four years of PhD in Heidelberg. It is to them that I would now like to express my gratitude.

First and foremost, I would like to thank you, Matthias, for your continuous encouragement and support, especially through the hardest times I have encountered during my PhD. I will always admire your enthusiasm, your passion for this job, your kindness. I am glad to have experienced this time under your guidance.

I would like to thank Prof. Joachim Wambsganßfor kindly accepting to be the second referee of my thesis. I would also like to thank the other members of the examining committee, Prof. Eva Grebel and Prof. Volker Springel.

A special big "grazie" goes to Matteo Maturi. Your guidance in the last year really made a difference, Matteo. I am not sure if I would have come to the end without your help. I admire your work, your passion, your pragmatism. Thanks for having been a "carabiniere" when I asked you to do it, but at the same time, for always having been able to cheer me up in my down days, and make me see the bright side.

The project I have conducted has its roots in the work of two former students of our group, Peter Melchior and Massimo Viola. Even if our presence at ITA did not overlap, you never denied me your help. Whenever I contacted you with a doubt or a question, or 1000 questions, your answer promptly arrived. The first steps would have been impossible without your aid and advice.

Big thanks go to Adi Zitrin. We shared a short but intense time as collaborators, a longer one as friends. Adi, I love how you can influence everybody around you with your dynamism and cheerfulness. You certainly did it with me, and I am grateful for that!

I would like to thank the IMPRS program, in particular Christian Fendt for his work and effort in making it successful. I am very grateful for being part of the 7th IMPRS generation. We had very good times together. I, especially, would like to warmly thank our representatives, Anahí and Jan, you did a great job!

I am grateful to all the colleagues at ITA that in some way contributed to

147

this work and made pleasant my everyday life at the institute. In particular, I want to thank Sven, little Matthias, Alex, Christian, Korbinian, Elena, and Luigi.

Ele, thanks for sharing with me this trip from its very beginning to the very last steps. I also thank you for understanding so well my feelings, my doubts, my worries, and for offering me your help whenever I needed it, even before we actually met. Thanks for all the coffees and chats we shared.

Fede and Ale, I missed you here at ITA. Knocking at your office always represented a way of finding a distraction, consolation, and help to face many different problems. You made me laugh and you made me think. Well, I am really glad for those times together.

Mauricio, without the "latinitá" you brought to ITA, my PhD would have not been the same. Thanks for all the work-time and party-time we shared. For all the chats and discussions, for involuntarily teaching me Spanish. Thanks for your vitality and energy, and for all the furniture that you moved for me! But, especially, thank you very much for the big help you provided me in so many occasions. Well, thanks for this special friendship.

Going from one to many of them, thanks to the Chilean or "quasi-Chilean" community for the all the evenings of drinking, partying, and dancing.

And now I come to the Family, the Heidelberg one. Anahi, Esteban, Iva and Marta, I cannot imagine there was a time I did not know you! We have shared so many things together that is impossible to make a list. So many are the reasons for which I really feel to thank you! I will try to summarize all of them in one sentence: you made Heidelberg my home, a wonderful home. Thank you so much!

Mat-teo, you were the only person I (kind of) knew when I arrived here. I am so (h)appy I had the opportunity to get to know you much better. Everything good that happened in Heidelberg started with, and thanks to you. We miss you!

Camilla, thanks for so often offering me a different point of view to look at the world, thanks for making me feeling comfortable to talk about everything with you, and thanks for the Italian dinners, so much needed sometimes!

Eduardo, I met you even before starting the PhD. Back then I did not know we would have become so close, your sweetness and your reliability are very special. Thanks for your advice, thanks for listening, and a big "grazie" for your detailed corrections.

Fabrizio, we both are people of not so many words (if you can say so in English...), but not always big words are necessary to create a bond. Your always being in for any new adventure, small or big, is a gift that I appreciate very much. I am very glad to have shared some of them with you.

Manu, when I saw you on that plane going from Rome to Leiden, I spotted you immediately; something was telling me that we were in some way similar. You contributed with something special to these years. Your sarcasm, your way of being, your wisdom, your loud laughter are so unique. Dai che questa aridità la combattiamo insieme, torna presto che mi manchi!

Thomas, thanks for bringing a bit of Germany in our group, I am so glad for that. And thanks for welcoming me in your family, my first real "German experience", a really worthy one!

Lucy, thanks for all the help and support you gave me in these last months, for never getting tired of our questions about English, for the nice words you always have. Lastly, thanks for contributing to double the European presence in the nights out!

A huge thank you goes to Arianna. When you arrived in Heidelberg, you brought here with you a bit of Trieste, and all the good things Trieste represented. I am very glad for that. More than a friend, you have been like a sister for me. I felt always at ease with you, in that way as can only happen at home. I miss so much our dinners together!

Last but not least, I would like to thank some friends that have not been physically here, but despite the distance, have managed to be close to me as I could have never hoped. Cristina, Maria, and Marco, you showed me how a friendship can survive large distances, long periods of few contact, substantial life changes. Every time I meet you it is like we never moved apart. Thank you for that!

Infine, voglio ringraziare la mia famiglia. Miriam e Marta, le mie sirocchie, quei vecchietti di mamma e papà, la bellissima piccola Febe ed Ema, un cognato speciale (anche se chiamarti così suona decisamente troppo distante, Ema!). Sono lontana da tanto tempo e probabilmente lo sarò per altro ancora. Ma il vostro affetto non è mai mancato. Pian piano negli anni ho portato a casa "pezzi" della mia vita altrove, per farveli conoscere, ma sopratutto perché loro potessero conoscere voi e capire così tante cose di me. Grazie per avermi dato in questi anni tutta la libertà che cercavo, tenendomi allo stesso tempo sempre vicina. Prometto che questa volta vi spiego per bene quello che faccio!

The time is running out, and still a long to-do list is awaiting me. I know that you would tell me: "Ma faster!" and, I have to admit, you would be right. However, this time I wanted to take it slowly, and give it the time and thought that you deserve. Thanks to all of you for having made this journey really worth!